Superconducting wind turbine generators

Mijatovic, Nenad; Jensen, Bogi Bech; Træholt, Chresten; Abrahamsen, Asger Bech

Publication date:
2014

Document Version
Publisher's PDF, also known as Version of record

Citation (APA):
Mijatovic, N., Jensen, B. B., Træholt, C., & Abrahamsen, A. B. (2014). Superconducting wind turbine generators. Technical University of Denmark, Department of Electrical Engineering.

Superconducting Wind Turbine Generators

Nenad Mijatovic
Center for Electric Technology
Technical University of Denmark

A thesis submitted for the degree of
PhilosophiæDoctor (PhD)
January 2012

1. Reviewer:
Henk Polinder, Ph.D

2. Reviewer:
Philippe J. Masson, Ph.D

3. Reviewer:
Arne Hejde Nielsen, MSc

Day of the defense: January 2012
Signature from head of PhD committee:

Primary Supervision:
Bogi B. Jensen, Ph.D.

Co – Supervision:
Chresten Træhold, Ph.D.

Co – Supervision:
Asger B. Abrahamsen, Ph.D.

Abstract

A HTS machine could be a way to address some of the technical barriers offshore wind energy is about to face. Due to the superior power density of HTS machines, this technology could become a milestone on which many, including the wind industry, will rely on in the future. The work presented in this thesis is a part of a larger endeavor, the Superwind project that focused on identifying the potentials that HTS machines could offer to the wind industry and addressing some of the challenges in the process. In order to identify these challenges, I have designed and constructed an HTS machine experimental setup which is made to serve as precursor, leading towards an optimized HTS machine concept proposed for wind turbines.

In part, the work presented in this thesis will focus on the description of the experimental setup and reasoning behind the choices made during the design. The setup comprises an HTS synchronous machine where a revolving armature winding spins around an open bath liquid nitrogen cryostat, which contains the HTS coils cooled down to 77 K. A significant part of the thesis is allocated to the description of the setup, particularly the torque transfer element and the compact cryostat design, where a concept with $\sim$20 W of heat transfer is achieved.

Following the setup description, the focus turns to the electromagnetic design of the HTS machine. Particularly, an approach to increase the performance of HTS coils and the influence of the armature reaction to the HTS field winding will be discussed.

Two design strategies are proposed, novel in a machine design, in order to reduce the amount of HTS required in a machine whereby the merits of both have been experimentally verified. The first employs a multiple HTS types in the machine design, since each type of the HTS tape has a specific

magnetic characteristic with respect to the critical current. I have showed that the potential for the reduction of HTS conductor can be significant, if the coils are placed strategically, whereby the coils wound with BSCCO performed 40% better depending on the placement in the field winding. The 2G coils were less sensitive to the placement which made them particularly useful for high magnetic field regions in the field winding. The second design approach proposed and tested was to use multiple current supplies which allowed each coil to operate close to its critical current. I have demonstrated that by introducing one additional power supply, an order of 12% higher MMF was generated (or equivalent HTS savings achieved). Increasing in the number of additional power supplies did not show the same potential for HTS reduction.

The implications of an armature reaction impact on the HTS field winding performance were examined and verified throughout a series of Locked Armature experiments. The interaction have been defined in the terms of two (direct and quadrature) axis machine theory (Park transformation), where significant reduction of $\sim 20\%$ was observed for the rated armature reaction in the q axis. Building on this observation, a control strategy for the excitation current to improve a partial load efficiency of a HTS machine is proposed.

Thus, this work has shown that a significant savings of a the costly HTS tape could be realized indicating that the HTS machine design can still be optimized towards more competitive alternative to conventional machines. Additionally, by constructing the HTS machine setup we went through most of the issues related to the HTS machine design which we managed to address in rather simple manner using everyday materials and therefore proving that HTS machines are close to commercialization.

Resumé

Høj temperatur superledende (HTS) maskiner kan komme til at adressere nogle af de tekniske barrierer som havvindmølle sektoren står over for på grund af deres overlegne effekt tæthed. Arbejdet præsenteret i denne afhandling er del af en større indsats i Superwind projektet, som er fokuseret på at identificere mulighederne HTS maskinerne kan bidrage til vindmølleindustrien og diskutere udfordringerne forbundet med dette. For at identificere udfordringerne, har jeg designet og konstrueret en HTS eksperimentel maskine opstilling, som skal danne grundlaget for optimeringen af et HTS maskine koncept til vind møller.

Arbejdet præsenteret i denne afhandling vil fokusere på en beskrivelse af den eksperimentelle opstilling og på tankerne bag de valg som blev truffet i design fasen. Opstillingen består af en HTS synkron maskine, hvor ankeret roteres omkring en åben bad flydende kvælstof kryostat, som indeholder HTS spolerne nedkølet til T = 77 K. En stor del af afhandlingen er dedikeret til beskrivelsen af opstillingen, specielt kraft moment overførsels elementet og det kompakte kryostat design, hvor et koncept med 20 W varme overførsel til den kolde rotor blev opnået.

Efter beskrivelsen af den eksperimentelle opstilling bliver fokus rettet mod de elektromagnetiske design overvejelser af HTS maskinen. Specielt bliver en måde at øge ydeevnen af HTS spoler og indflydelsen af anker vekselvirkningen på HTS felt viklingen diskuteret. To nye design strategier bliver foreslået med formålet at reducere mængden af HTS leder som er nødvendigt i en maskine og fordelen ved disse bliver eftervist eksperimentelt. Den første strategi omfatter brugen af forskellige typer af HTS tapes i en maskine, fordi de har forskellige karakteristika med hensyn til den kritiske strøm de kan bære. Jeg har vist, at potentialet for at reduceret HTS tape

forbruget er betydeligt, hvis forskellige spoler placeres strategisk og i tilfældet af spoler viklet med BSCCO tape kan ydeevnen forøges med 40 %. Spolerne baseret på 2G tape var mindre følsomme over for magnet felt og gjorde dem specielt anvendelige i regioner af felt viklingerne med høje magnet felter. Den anden design strategi er at benytte flere strømforsyninger, som tillader at hver spole kan forsynes med en strøm tæt på den kritiske strøm af spolen. Jeg har demonstreret, at man kan øge MMF af rotor viklingen med omkring 12 % ved at introducere en ekstra strømforsyning (hvilket svarer til en mulig 12 % reduktion af forbrug af tape). Der blev ikke observeret yderligere forbedringer ved at introducere flere forsyninger.

Indvirkningen af anker vekselvirkningen på HTS felt viklingen er blevet undersøgt og eftervist i en række låste anker eksperimenter. Vekselvirkningen er blevet defineret i termer af to-akse maskine teori (Park transformationen) og en signifikant reduktion på 20 % blev observeret med nominal anker vekselvirkning i q-aksen. Disse observationer er blevet benyttet til at foreslå en kontrol strategi for magnetiserings strømmen for at forbedre effektiviteten af en HTS maskine ved dellastning.

Dette arbejde har vist at en signifikant besparelse på den dyre HTS tape kan opnås og dermed indikerer, at designet af HTS maskiner kan optimeres mod et konkurrence dygtigt alternativ til konventionelle maskiner. Desuden har konstruktionen af test opstillingen bragt Superwind teamet igennem de fleste design overvejelser for en HTS maskine, og da det er lykkedes at løse disse med brug af simple materialer er det bevist at HTS maskiner er tæt på en kommercialisering.

To Andrijana

Preface

This thesis was written at Center for Electric Technology (CET) which is a part of Department of Electrical Engineering at Technical University of Denmark (DTU) in partial fulfilment of the requirements for acquiring the Ph.D. degree. The Ph.D. project is supported by the DTU globalization funds in the framework of the Superwind project. The main focus of the study is a design and performance evaluation of a HTS machine with reference to the wind turbine application.

At the beginning of my project, the aim was to design a 50 kW demonstration HTS machine as a prototype for the future wind turbine generator. Since a HTS machine research is a costly venture, ambitions had to be revised. Instead, creating a versatile experimental HTS machine setup in order to build a solid base knowledge that will ultimately lead towards an optimized machine prototype was considered a better choice.

In the first year of my work, I have spent significant time learning about superconductivity and its applications since my background was in design, analysis and control of conventional electrical machine. At the same time, the effort was made to strengthen the competence in the machine design at CET by employing a senior specialist in the field. The situation changed when Dr. Bogi B. Jensen started in 2010 as Associate Professor teaching electrical machines and stepped in as my primary supervisor since my previous supervisor Professor Niels F. Pedersen retired. Parallel to the learning process, I have worked on the HTS machine design starting out with the main design issues and considerations. The design and construction process spanned over two and a half years where most of the parts were designed and built from scratch.

My most sincere gratitude, I would like to extend to people at CET and Risø who gave me the opportunity to carry out this research and welcomed me to Superwind team. From the very beginning I have felt as part of the team and a valued member and for that I am very grateful to everyone in Superwind. I would like to express special thanks to Bogi B. Jensen , Chresten Træhold (co- supervisor), Asger B. Abrahamsen (co-supervisor) and Niels F. Pedersen for all support and guidance without which my research would be impossible. Big thanks to NKT cables for providing assess to measuring hardware which made data acquisition and experiments to run smoothly. Many thanks to Freddie Fahnøe and the staff in the workshop for help provided with all practical issues. Furthermore, I would like to express my thanks to CET management, Jacob Østergaard and Morten Sadolin, where in the time of challenging conditions during the reconstruction of laboratories, I could rely on your support and understanding. Last but not least, without the support and encouragement from my Andrijana, family and friends to whom I owe so much, none of my dreams could be realized; thank you!

Declaration

I herewith declare that I have produced this paper without the prohibited assistance of third parties and without making use of aids other than those specified; notions taken over directly or indirectly from other sources have been identified as such. This paper has not previously been presented in identical or similar form to any other Danish or foreign examination board.

The thesis work was conducted from 1. May 2008 to 31. December 2011 under the supervision of Prof. em. Niels Falsig Pedersen in period from 1. May 2008 until 30. May 2010 and Dr. Bogi Bech Jensen from 1. Jun 2010 until 31. December 2011 at Department of Electric Engineering, Technical University of Denmark .

Lyngby, December 2011

Nenad Mijatovic

Contents

List of Figures

List of Tables

Glossary

LN_2	Liquid Nitrogen
MgB_2	Magnesium Diborate, a superconducting compound with moderate transition temperature of 39 K
1G	First generation of High Temperature Superconductor tape or BSCOO or Bi–2223
2G	Second generation of High Temperature Superconductor tape or YBCO or Coated Conductor
AMS344	YBCO 344 coated conductor from American Superconductor
AMSC	American Superconductor Inc.
Arr1	Configuration of the HTS field winding with four HTS coils
Arr2	Configuration of the HTS field winding with six HTS coils
Bi–2223	$Bi_2Sr_2Ca_2Cu_3O_{10}$ High Temperature Superconductor
BSCOO	$Bi_2Sr_2Ca_2Cu_3O_{10}$ High Temperature Superconductor
CC	Coated Conductors
DD	Direct Drive wind turbine
DDPMSM	Direct Drive Permanent Magnet Synchronous Machine
EC	European Commission
EU	European Union
EU–27	European Union member states
EWEA	European Wind Energy Association
GM	Gifford–McMahon refrigerator or cryocooler
HP	Hewlett–Packard
HTS	High Temperature Superconductors
IBAD	Ion Beam Assisted Deposition
ICPP	Intergovernmental Panel on Climate Change

GLOSSARY

IV curve	Relation between current and voltage of superconductor.
LTS	Low Temperature Superconductor
MMF	Magneto motive force
MOCVD	Metal Organic Chemical Vapor Deposition
MOD	Metal Organic Deposition
MTOE	Million Tons of Oil Equivalent
p	number of pair of poles
p.u.	per unit
PIT	Powder In Tube wire manufacturing technology
PM	Permanent Magnet
PMSM	Permanent Magnet Synchronous Machine
PT	Pulse Tube refrigerator or cryocooler
RABITS	Rolling Assisted Bi-axial Textured Substrate
RE	Rare Earth element
SC	Superconductor
SM	Synchronous Machine
SS	Stainless steel
TTE	Torque Transfer Element
USD	US dollar
USD/kAm	US dollar per meter for 1000 A conductor
YBCO	$YBa_2Cu_3O_6$ High Temperature Superconductor

Chapter 1

Introduction

"Happy is he who gets to know the reasons for things." **by Virgil**.

1.1 Motivation and challenges - An HTS direct drive wind turbine

The offshore wind energy sector is expected to expand in the next decade. However, the speed of the development of the offshore wind is impeded by the market cost as at the moment it is twice as costly as onshore wind energy. As a way to decrease a cost of wind energy, the trend towards large wind turbines can be observed where the size of 10 MW is expected. A broader discussion about the trends, state of the renewable energy and the incentives for the offshore wind development is presented in Appendix.**??**. The increase in the size of the turbines is followed by the number of challenges where the size and the weight of a direct drive generator are significant contributors.

On the other hand, one of the prominent characteristics of superconducting machines is superior power density compared to a conventional machine, which is expected to be $1.5 - 3$ times higher(3, 4, 5). Therefore, if the superconducting machine is employed as a wind turbine generator, scaling of gearless drive train becomes technically easier and potentially commercially superior (which depends on the cost and maturity the HTS technology). In addition, the HTS technology is several times less susceptible to the cost fluctuations of the Rare Earth elements. This stems from the fact that an HTS machine would use three orders of magnitude less of the Rare Earth elements than a permanent magnet alternative (which is highly attractive for wind application). Comparison between 10 MW High Temperature Superconductor and Permanent Magnet direct drive generator with respect to the usage of Rare Earth elements is included in the **??**, where an estimated requirement for RE if the future turbines are PM machines, would be higher than the world's annual production of RE.

To investigate the potential of High Temperature Superconductor machines in the wind energy, it is vital to examine the superconducting machine as a whole, where all aspects are considered, such as: cooling efficiency, complexity and reliability; HTS tape performance, cost and availability; auxiliary systems like protection system and power electronic control units; a machine performance and maintenance etc.

Since an HTS technology is still in the phase of development, the design and construction of the specific prototype would involve too many unknowns. As an alternative approach, the experimental setup where a number of superconducting materials could be employed and machine concepts could be examined had an obvious advantage and it was deemed to be more valuable at this stage. The design of the experimental setup has involved the same (or similar) challenges a specific HTS machine would have and thereby prove to be a highly educational endeavor. Therefore, this work (as a part of Superwind) presents a valuable contribution to the global knowledge pool regarding HTS machines and it represents the initial step towards an optimized design machine design intended for large wind turbines.

1.2 Layout of the thesis

Chapter-2 – The thesis will start by introducing the superconductivity which is intended for readers new to the field, underling the physical differences between types of High Temperature Superconductors and their physical properties. Manufacturing and cost projection based on the raw material content is carried out, and prospect of HTS candidates for large scale application are indentified.

Chapter-3 – In Ch.3, the concept of HTS machines are explained and the overview of demonstration projects to date is given. The concepts of an HTS machine with a high torque density are identified as the candidates for the future wind turbines. Specific aspects of an HTS machine design such as cooling systems and torque transfer from a low temperature to a room temperature are identified as crucial in the design and general recommendations with respect to the design of these are presented. Furthermore, I will briefly reflect on the nature of HTS machine parameters and the implications of these for a wind turbine application. This is done with the help of an analytic model of an HTS machine where in addition a magnetic interaction between an HTS winding and armature winding is identified as one of the important aspects for the performance of the HTS. The interaction is afterwards examined experimentally. Finally, the chapter will conclude by proposing two design strategies for improving the performance of an HTS field winding.

Chapter-4 – The design details and choices made in the Sperwind project during the design and construction of the HTS machine setup are presented in Ch.4. The flexibility of the design and value of such a concept are emphasized.

Chapter-5 – Experimental results are presented and discussed in Ch.5. The HTS coils are characterized at the beginning of the chapter. The hypothesis presented in Ch.3 are verified where versatility of the experimental setup will prove to be highly useful.

The impact of the armature reaction on the performance of the HTS winding is examined throughout a series of experiments, after which this interaction is quantified and defined in terms of two (quadrature) axis machine theory (Park model). Consequently, the control strategy for an HTS machine excitation current is proposed aimed to improve the performance of an HTS machine at partial load. In addition, the design approach concepts proposed in Ch.3 to improve the performance of an HTS field winding are put to the test where obtained results are presented and their implication discussed. Finally, the Superwind HTS machine is characterized by the No Load and Short Circuit experiments where combination of these have been used to derive the machines parameters which are compared to the machine parameters derived from the FE model.

Chapter-6 – The chapter provides a summary of the thesis and outlines its main contributions, achievements, but also its boundaries and limitations. Furthermore, possible future work is discussed since this thesis represents only a part of what is intended to be a longer strategic research related to HTS machine design.

Chapter 2

Superconductivity

"The experiment left no doubt that, as far as accuracy of measurement went, the resistance disappeared. At the same time, however, something unexpected occurred. The disappearance did not take place gradually but abruptly. From 1/500 the resistance at 4.2 K, it could be established that the resistance had become less than a thousand-millionth part of that at normal temperature. Thus the mercury at 4.2K has entered a new state, which, owing to its particular electrical properties, can be called the state of superconductivity." **by Heike Kamerlingh Onnes**.

Superconductivity has played an essential role in the development of both science and technology. This chapter will give a short retrospective of the history of superconductivity. The difference between normal conductivity and two types of superconductivity is reviewed and physical properties of High Temperature Superconductors (HTS) used in the Superwind project are presented. Production process will be described together with the electromagnetic performance of each of the conductor. Chapter2 will conclude with a review of published work on production scale up and cost forecasting of HTS intended for large scale applications.

2.1 Brief history of Superconductivity

Superconductivity as a phenomena was discovered a century ago, by Heike Kamerlingh Onnes in 1911 in Leiden during his experiments with mercury at liquid helium temperatures (6). In those experiments he observed an abrupt transition and absence of electrical resistance of Hg at $4.2K$. In following decades, superconductivity was observed in several other materials, mostly metals and metal alloys. The chronology of discovery of superconductivity in various materials is presented in the Fig.2.1.

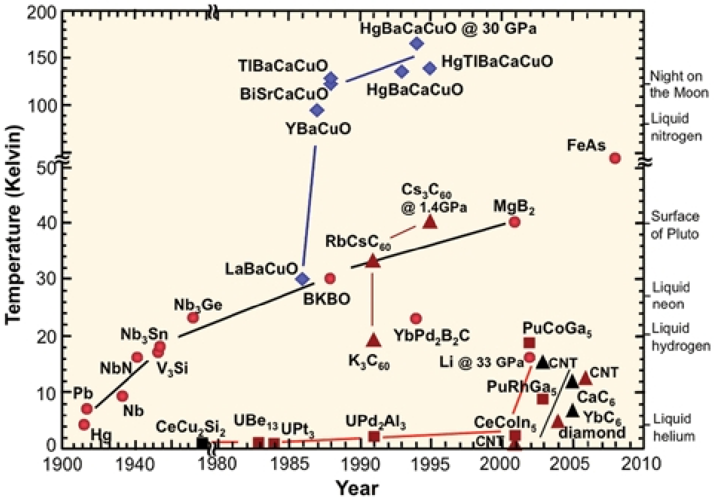

Figure 2.1: Discovery of superconductivity in various materials during a century of research - The metals and metal alloys are presented with red markers, while HTS ceramics are blue. Source: Reprinted from(7)

The breakthrough in the field came in 1986, when Bednorz and Mueller discovered superconductivity in a lanthanum-based material (8) (for which they were awarded the Nobel prize(9)). The $La_2 - BaCuO_4$ had a transition temperature of 35K which was believed to be impossible at that time(10). This discovery was followed by the discovery of $YBa_2Cu_3O_{6+x}$ (11) in 1987 with a transition temperature of 93 K. The quest for materials with even higher values of T_c was on the way, where room temperature superconductivity was predicted as an ultimate and yet unfulfilled goal (12). The most recent developments in material science have led to the discoveries of superconductivity in MgB_2 (13) and $FeAs$ (14) which caused a debate about their unique physical properties.

Thus with a discovery of new superconductors, the understanding of physical mechanisms behind superconductivity increased over the years. A brief explanation on basic differences between normal conduction and superconducting phenomena is presented in the following section.

2.2 Physics of superconductivity

Superconductivity is a complex phenomena occurring in some materials under certain conditions. Electric current in normal material (metals) constitutes the motion of electrons. As moving electrons collide with the lattice, part of the kinetic energy is converted into heat which constitutes a partial loss of the electrons energy (15). Macroscopically speaking, this energy dissipation gives rise to the notion of resistance. With the discovery of superconductivity, the apparent resistance vanished, thus allowing lossless flow of electric current (6).

On the other hand, superconductivity is caused by pairing of conduction electrons in metals into an electron pair, a so called Cooper pair. The flow of Cooper pairs constitutes a 'super-current', ie. a current in a material flowing without any resistance (electron pair lattice, collision free interaction) (16). Coupling of electrons into Cooper pairs is caused by the interaction of electrons and crystal lattice vibration of a material. One of the moving electrons will attract the positive ions of the crystal lattice, which will contract after the electron has moved on (17). The contracted region of the lattice will appear slightly more positive and thereby attract another electron. Thus, an attractive interaction is established via the lattice vibration. The electron - phonon mediated superconductivity was described theoretically by Bardeen, Cooper and Schrieffer in the famous BCS theory (18, 19).

The prediction of 30 K (28 K calculated for Nb_3Sn)(10) as the highest theoretical temperature above which superconductivity could not exist, derived from BSC theory, was based on the general material parameters of metals and alloys. However, the report of $T_c = 35$ K in 1986 in the ceramic compound La_2BaCuO_4 and later $T_c = 93$ K in $YBa_2Cu_3O_6$ (10) was in contradiction with what was at that time the understanding of electron pairing mechanisms. This was a birth of a new class of materials, called High Temperature Superconductors (HTS) due to a widely accepted belief that T_c could not surpass 30 K.

2.2.1 Classification of superconductors

Superconductors can be classified into type 1 and type 2 superconductors (10). Type 1 are usually pure metals characterized by the Meissner state where superconductivity vanishes when an applied magnetic field becomes higher than the critical magnetic field (20). Type 2 superconductors are bi-metals and ceramic materials characterized by the Meissner state for magnetic fields lower than the first critical magnetic field, H_{c1}. However, for magnetic fields above the lower critical value superconductivity does not disappear. Instead, the material enters into a mixed state where the magnetic field gradually penetrates into the superconductor in non-superconducting tube shaped regions called flux lines. If the applied magnetic field becomes larger than the upper critical magnetic field, H_{c2}, the superconductivity will vanish and the superconductor will enter into a "normal state"(20). All practical applications of superconductivity are based on type 2 superconductors.

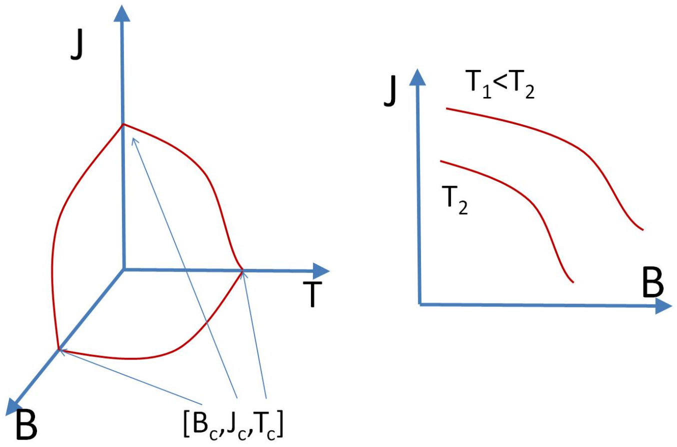

Figure 2.2: $J - B - T$ critical surface - Illustration of critical surface defined by the critical current (or critical current density), magnetic flux density (or magnetic field) and temperature, i.e. $J - B - T$.

2.2.2 Critical parameters of superconductor

A superconducting state of material is described by three parameters, the critical magnetic field (or flux density), the critical current density and the critical temperature. If presented in a 3D Cartesian coordinate system, these parameters will define a so called critical surface. A typical critical surface of a superconductor is illustrated in Fig.2.2 and presents a boundary between superconducting and normal conducting state.

The definition of critical current of superconducting (HTS) material is related to the measure of pinning sites (crystal defects and incorporated nano–particles), which will prevent the flux lines from moving due to the force acting on them caused by a current flowing in the material. Yet, macroscopically, the current - voltage relation of superconductors, where voltage increases due to the motion of flux vortexes, can be described with a power law, as expressed in 2.1

$$E = E_0 \left(\frac{I}{I_c(B,T)} \right)^{n(B,T)} \tag{2.1}$$

where I_c is the critical current of the superconductor and the n value is an exponent which defines how abruptly the transition between superconducting and normal state occurs. These are parameters of material and are dependent on the magnetic field and temperature. The criteria used to define critical electric field (electric field in a superconductor when the critical current is running) is E_0=1 μV/cm=10^{-4} V/m.

The expression 2.1 can be used as one of the ways to experimentally determine I_c of a superconductor. The so called 'Short sample' experiment (21) is experiment where a short piece of superconductor is cooled to the desired temperature after which a transport current is passed through the sample and the voltage drop across the superconductor is measured. By increasing the transport current, the critical current is reached when the voltage drop becomes equal to the critical electric field E_0 =1 μV/cm=10^{-4}V/m. Repeating this, for several temperatures and values of external magnetic field, a family of so called 'IV' curves is collected. Further post processing of IV data with the help of 2.1 will result in a critical surface (illustrated in the Fig.2.2) for that particular HTS conductor.

2.3 HTS conductors

HTS produced as commercial conductors which are used in superconducting applications, are $Bi_2Sr_2Ca_2Cu_3O_{10}$ (Bi–2223) and $YBa_2Cu_3O_6$(YBCO). In recent years MgB_2 has gained high attention and looks very promising for number of applications. Since this project is limited to T= 77 K, MgB_2 was not considered as an option due to its low T_c. The Bi–2223 was first to be commercially produced as HTS tapes from the early 1990's (22). Thus, the name 'first generation of HTS' or 1G is often used and will be used in this thesis too. The YBCO came some years later and therefore is known as a 'second generation of HTS or 2G conductor.

Both HTS materials are ceramic oxides where superconductivity takes place in CuO_2 planes of the material lattice (20). The prevailing belief is that with an increase of CuO_2 planes in the unit cell of the lattice, the critical temperatures of superconductors will increase. Yet, this trend is absent for more than 3 layers (23) since compounds with higher number of planes are not chemically stable. Thus, alignment of the CuO_2 planes of the grains of the material is of crucial importance. Achieving a high level of superconductor grain aliment is one of the inhibiting factors in an HTS wire manufacturing, downgrading the performance of HTS wires. To understand the limitation and potentials of these HTS conductors first it is necessary to understand how difficult it is to produce an HTS wire (tapes).

2.3.1 Manufacturing of Bi–2223

The 1G HTS tapes are made by the Powder In a Tube (PIT) wire technology. The PIT production process, illustrated in Fig.2.3, starts by loading a pressed powder pellet into a silver tube, which is further subsequentlty drawn into thinner diameter wires. Thin wires of Bi–2223 immersed in a silver matrix are packed into a silver tube and drawn again. This is continued until the target wire diameter is obtained (24). The final step of extrusion is rolling the multi–filament wire into the tape with rectangular cross section, where ∼4 mm wide and ∼0.3 mm thick tape is most common. Multi–filament wires are reacted in an atmosphere of oxygen, which can diffuse through silver at high temperatures. As mentioned before, good alignment of the Bi–2223 grains is a crucial element which determines critical current density of the final conductor. As a final conductor, a BSCCO conductor comprise 70%-30% share of silver to HTS ratio which can vary but the ration of BSCCO rarely gets above 30% .

One of the leading companies of 1G HTS today is Sumitomo Electric Industries (25). American Superconductor Inc. started its HTS program with 1G but have recently declared development of only 2G HTS (1). Several manufactures, somewhat smaller, such as Bruker Energy(26), Zenergy Power(27) and others also have 1G in its product portfolio.

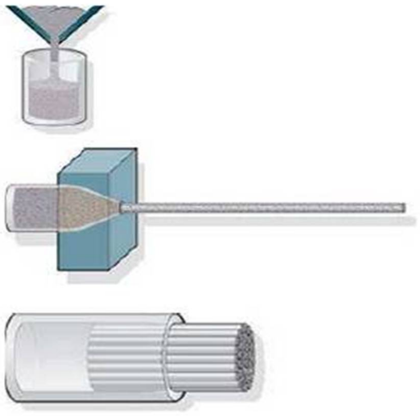

Figure 2.3: Powder In a Tube production steps - PIT wire technology is based on basic production steps illustrated in this figure. The loading of a pressed powder pellet into a metal tube is the first step which is followed by an extrusion. Last step illustrates packing and extrusion of several wires into a multi–filament wire. The last step is repeated until desired size of the filament is achieved.

2.3.2 J–B–T characteristics of 1G HTS

One of the tapes used in the Superwind project is 1G HTS. Thus, the nature of BSCCO characteristic critical current - magnetic field interaction will be discussed on the example of critical current of the DI-BSCCO from Sumitomo(25). The critical current will be a function of an external magnetic field applied either parallel or perpendicular to the wide side of the tape. Presented in the Fig.2.4, the $I_c(B)$ dependence is shown for several temperatures. For $T=$ 77 K and magnetic flux density B $\leq$0.5 T applied perpendicular to the wide side of the HTS tape, the critical current reduction is large. For the parallel direction of magnetic flux that is not the case. Magnetic anisotropy of 1G HTS is strongest at high temperature ($\geq$70 K) where at lower temperatures ($\leq$30 K), 1G tape will exhibit both lower sensitivity to magnetic field and lesser difference between parallel and perpendicular directions of external magnetic field.

At low temperatures (20 K – 30 K) an increase in I_c of 1G tape can be tenfold where a lower magnetic sensitivity and anisotropy of the conductor are observed. Thus, it may be concluded that the Bi–2223 superconductor is suitable for low magnetic field applications at high temperatures where the performance of a tape is substantially improved at lower temperature.

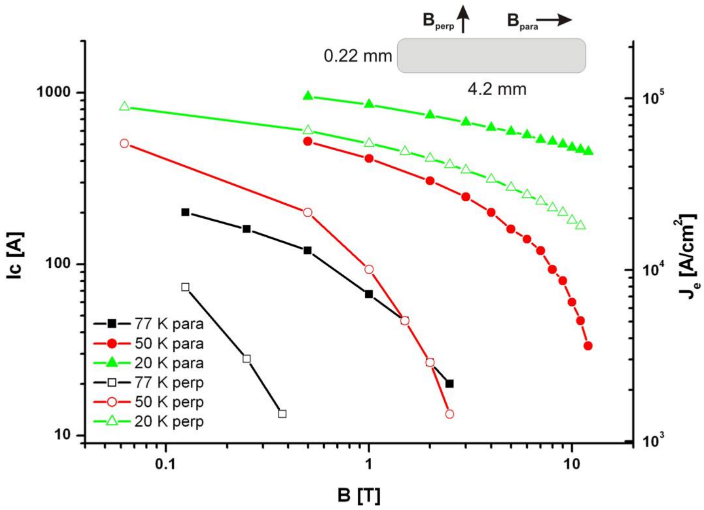

Figure 2.4: Critical current of DI-BSCCO - The figure illustrates the critical current I_c and engineering critical current density J_e (defined as the critical current divided by the wire area of a 4.2 mm wide and 0.22 mm thick Bi–2223 wire from Sumitomo) at different temperatures and as a function of applied field either parallel (B_{para}) or perpendicular (B_{perp}) to the HTS tape. Reproduced from:(28).

2.3.3 Manufacturing of YBCO

Several attempts were reported of YBCO wire production with PIT wire technology, but the obtained critical current densities reported were orders of magnitude lower compared to Bi–2223 (28, 29, 30). Insufficient alignment and connectivity of the grains are the main causes for the low values of critical current. Therefore, even though the YBCO wires produced with PIT technology have superconducting properties, the values are too low to make this production practical. One of the ways to obtain a bi-axial alignment of the CuO_2 planes of the YBCO grains in a conductor is to grow the YBCO as a thin film on the top of a bi-axially textured substrate(31). Such wires are called coated conductors (CC) and are based on either bi-axial textured metal substrates or bi-axial deposition of buffer layers on non-textured metal substrate(31).

Several ceramic buffer layers may be deposited on the metal in order to achieve a better match between the material lattice of the buffer and the lattice of the YBCO. The illustration of the general architecture of coated conductors produced commercially today is presented in Fig.2.5. American Superconductor as a primary manufacturer of CC is using the Rolling Assisted Bi-axial Textured Substrates (RABITS) (32, 33),

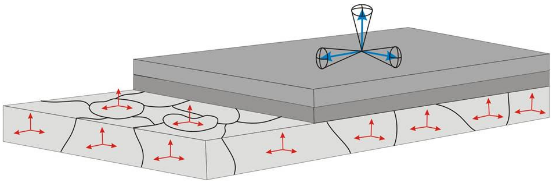

Figure 2.5: YBCO Coated Conductor (CC) - Architecture of coated conductor consisting of a metal substrate (light gray), one or more ceramic buffer layers (darker gray) and on top a $(RE)Ba_2Cu_3O_6$ layer (dark gray). Orientation of $(RE)Ba_2Cu_3O_6$ grains is induced by the texture of substrate and buffer layers. Reproduced from:(28).

sputtering of buffer layers and Metal Organic Deposition (MOD) of the YBCO layer (1), which is subsequently sealed by a metal layer on top. SuperPower is using non–textured metal substrates and obtain a bi-axial textured buffer layer by Ion Beam Assisted Deposition (IBAD) (34) followed by Metal Organic Chemical Vapor Deposition (MOCVD) of the YBCO layer (2).

2.3.4 J–B–T characteristics of 2G HTS

Critical current of a CC from American Superconductor is shown in Fig.2.6 for 75 K and 64 K. It is obvious that the J_e anisotropy is smaller for CC compared to the 1G tape at magnetic fields larger than 1 Tesla and at temperatures above 64 K.

It should be noted that the active superconductor layer (YBCO) of the CC is only ∼1 μm thick compared to the total tape thickness of 0.2 mm. Thus the critical current density of the superconductor by itself is $J_c = 2{\cdot}10^6$A/cm^2 at T= 77 K and in self field. Given that YBCO CC are a relatively new technology and $R\&D$ is ongoing, substantial improvement of J_e of CC could be achieved either by improving the HTS properties of the thin layer of YBCO (improved pinning, alignment...), increasing the layer thickness where J_c is maintained, or by reducing the substrate thickness (35, 36, 37). Some of the listed methods may sound simple enough but a number of challenges must be addressed first.

One of the major challenges in further development of the coated conductors is to increase the superconducting fraction of the tape cross section area by growing thicker layers while maintaining J_c. The present technology is limited to a YBCO layer thickness of ≤2 μm, since further increase in thickness is not improving J_e (33, 38).

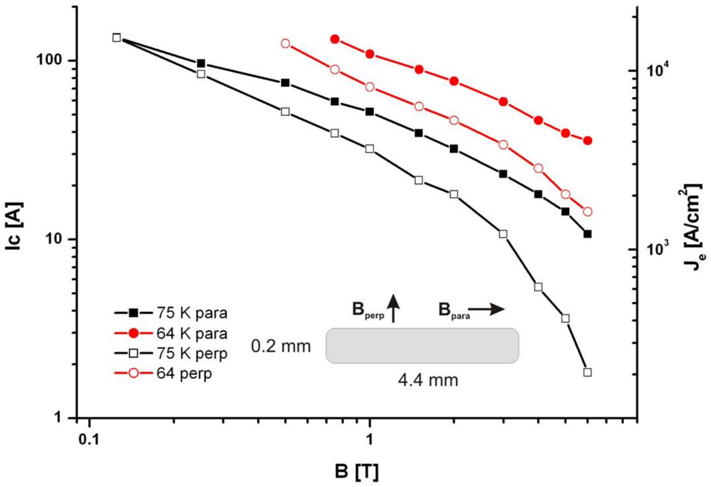

Figure 2.6: Critical current of YBCO, AMS344 - Critical current, I_c, and engineering critical current density, J_e, of 344 coated conductor from American Superconductor as function of the field parallel or along the tape for two temperatures. The cross section area of the tape is shown by the insert and the critical current in self field and at T= 77 K is I_c= 140 A (1).Reproduced from:(28).

It should be said that progress with respect to YBCO layer thickness is reported (39) without loss of J_c which is highly encouraging.

2.4 Production of HTS: scale consideration

Production capacity of HTS (both 1G and 2G) worldwide is estimated to be 1000 km annually in 2009 (40) which is only a fraction of the production capacity required to maintain large-scale application such as HTS machines or HTS cables ($\sim$3% (41)). The maximum length of HTS conductors in continues pieces needs to be increased. For 1G conductor, lengths above 1000 m for a single tape have become a standard (42), while 2G tape is still produced in only a few hundred meters lengths (43, 44), even though a slow increase in lengths is noticeable (45). Issues with increasing the length of single tape in part stems from variations of critical parameters over the length of the tape, where a section with low I_c downgrades the whole batch.

An important aspect to consider before choosing which HTS technology to use in large scale application is growth potential. As a good point of reference with respect to the cost - performance evaluation, a low temperature superconductor (LTS) could be used. A cost - performance factor is compared among superconductors through the cost of conductor in USD (US Dollars) versus current capacity per length in kAm. $NbTi$ and $NbSn_3$ conductors have a cost of 1 USD/kAm and 8 USD/kAm at 4.2 K, respectively. Breakdown of material content for both 1G and 2G tapes can provide better insight in scaling implications with respect to the cost - performance evaluation.

A BSCCO HTS tape is comprised of 70%–30% share of silver to superconductor ratio (46). The cost of 1G HTS will never become lower than cost of raw material used. Due to high content of silver, even if the cost of HTS is neglected, the cost of 1G tape will be 70% of the value of silver, i.e $0.7C_{Ag}$, where C_{Ag} is the cost of silver. If the 0.3 USD/gram (47) is adopted for a price of silver, the resulting cost for 1G tape taking only that into the account would be ~20 USD/kAm. The price in 2011 for 1G HTS tape was ~200 USD/kAm, which implies that the cost reduction is possible, assuming production and cost of BSCCO are lower than silver. However, the lowest cost 1G HTS could ever reach would be closely correlated to the price of silver.

On the other hand, 2G HTS is comprised of a 1–2 micron thick superconducting layer deposited on a substrate (such as stainless steel) resulting in HTS tape which is 0.2 mm–0.3 mm thick (1, 2). The HTS content (YBCO) in 2G conductor is 0.5% – 1.5% of conductor thickness. Thus, the cost of YBCO will be added to other costs. Other cost contributors such as cost of substrate, buffer layers and laminates will be minor contributors to a total cost. It should be noted that capital investment and production cost can be significant (44). Nevertheless, these initial costs will be subjected to a learning curve and as the production optimization level increases, so will the reduction of cost, all driven by the increase in volume of production.

Yttrium is one of the rare earth (RE) elements in the periodic table with the cost of 56 USD/kg for yttrium oxide in 2010 (48). Since the required amount of yttrium is very small, $\sim$ 30 mg per meter for 4 mm wide tape with 1.2 micron thick YBCO layer, the cost of active raw material in 2G HTS tape would be $\leq$1 USD/kAm. Cost of substrate and thin coating of silver were included as well while the deposition efficiency of YBCO layer was not included. The cost of 2G HTS in 2010 was 200–400 USD/kAm.

This simple analysis shows that the cost of 2G HTS stems from its complex production process and thus holds the potential for great reduction with production optimization. It is also important to stress that 2G technology harbors higher potential of increasing J_e, a parameter not explicitly quantified by USD/kAm criteria. Several approaches have been proposed and promising results were reported such as improved pining(49) and increased HTS layer thickness as reported in (39).

Chapter 3

HTS machines

"The rotating armatures of every generator and motor in this age of electricity are steadily proclaiming the truth of the relativity theory to all who have ears to hear." **by Leigh Page**.

The motivation for superconducting machines was known from as early as 1960 when the first demonstrations of superconducting machines took place (50). Hence, the idea to improve the conventional design of electric machines has been tried before with low temperature superconductors (niobium titanium and niobium tin) in several demonstration projects(50). Most of the initiated demonstrations were successful and proved merits and technical feasibility of superconducting machines. However, in the first ambitious effort to demonstrate a fully superconducting synchronous machine, where both stator and rotor winding were superconducting(51), that was not the case. A 50 kW machine failed during testing, yet it was the very first evidence of the importance that ac losses have in application of superconductivity and complexity involved in the design of superconducting machines.

After initial successful demonstrations, an aim of further LTS machine development focused on utility generators where the number of designs and demonstrations ranging from 20 MW up to 1200 MW was carried out. All of these have confirmed over and over that the concept of a superconducting machine is promising, but have also identified various issues where the difficulty of the refrigeration to 4 K was by far the largest(50).

With the discovery of HTS and the possibility of higher operation temperatures, superconducting machines have become again interesting to researchers. A main difference between LTS and HTS application is not only that the temperature range is substantially higher, but the temperature operational window of HTS material is much wider. Hence, a refrigeration system and thermal insulation can be simpler and more efficient compared to LTS systems. A number of designs have been suggested over the course of two decades to enhance electric machines with usage of HTS. Among the proposed machines which could benefit by employing HTS were synchronous, induction, switched reluctance, trapped field and dc homopolar machines. Improvements and design challenges of the most promising HTS machine concepts will be reviewed in coming sections where the concept most suitable for lightweight machines is identified.

It is interesting to notice that even from early on in the history of application of superconductivity, very few novel concepts of superconducting machines have been proposed (a Meissner motor, Trapped field motor). Instead, superconductivity was used to enhance conventional designs by increasing either the magnetic field or electric loading in a machine.

3.1 Superconducting machine - motivation

Regardless of if it is a dc or an ac machine, machine operation is based on the interaction of two magnetic fields, one from the rotor and one from the stator. It is possible to express the power and torque output of an electrical machine in terms of these fields and the machine dimensions, as 3.1

$$P = \frac{\pi^2}{\sqrt{2}} k_w B_r A_s D^2 L n_s \Longrightarrow \frac{P}{n_s} = T = (2\sqrt{2}\pi k_w) B_r A_s V \tag{3.1}$$

where B_r, A_s and V=(D/2)$^2\pi$L are flux density at an air gap produced by the rotor, electrical loading of an armature winding and the volume of a machine (air gap), respectively. k_w is the winding coefficient for the armature winding while n_s stands for rotational speed of machine.

For a conventional electrical machine, the product $B_r A_s$ is limited by material properties. Maximum values of peak air gap flux densities in all machine designs are limited to values 1 T due to saturation of the magnetic circuit. Any increase in the flux density would call for substantial magneto-motive (MMF) force to drive it, which means higher current in the copper turns of the rotor winding (or thicker permanent magnets if a PM machine is in question). Consequently, one can come to the conclusion that excessive cooling must be used to manage temperature increase in the rotor winding (caused by high current densities), and that only a small increase of the air gap flux density could be obtained due to the low magnetic permeability of saturated steel.

Electric loading of a conventional machine produced by the stator (armature winding) is bound by the maximum temperature of electric insulation (usually 120°C – 150°C) to 50 kA/m – 200 kA/m depending on cooling (52, 53). An additional, but less prominent constraint to armature loading is the maximum force (radial in faults). Thus, a closer look at the torque expression, 3.1, by taking into account that $B_r A_s$ product has its maximum, reveals that the size of a conventional electric machine is related to the torque T that the machine can develop. In order to increase the torque density of machine, according to 3.1, only an increase of $B_r A_s$ will give results.

Superconductor, with practically lossless magneto-motive force (MMF) can provide a significant increase of MMF available in a machine design. Consequently, the product $B_r A_s$ could be improved by increasing the value of the air gap flux density to $\geq$2 T or even further by increasing both the air gap flux and the electric loading, depending on where the superconductors are employed. Accordingly, superconducting machines can be made smaller than conventional machines and the degree of volume and weight reduction can be adjusted by choice of the $B_r A_s$ value.

3.2 Design concepts of an HTS machines and practical experience

The description of design concepts for HTS machines proposed and demonstrated to date is presented in the following section. The most frequent design used for an HTS application is a synchronous machine (SM), where the dc application of HTS offers the most of advantages(54). Several other HTS machines such as induction, switch reluctance, trapped field machines, dc homopolar machines and others are described as well.

3.2.1 Synchronous machines (SM)

The majority of the designs proposed and demonstrated have been radial flux SM, but the same configurations with a little modification are applicable for axial flux machine as well. Moreover, it is possible to make a distinction between two concepts: HTS SM where only the field winding is superconducting and HTS machine where both field and armature windings are superconducting, which will be referred to as a full HTS SM in order to avoid confusion.

3.2.1.1 An HTS–SM with warm rotor

An HTS machine with a conventional armature winding (slotted stator), warm rotor iron and an HTS rotor coil, illustrated in Fig.3.1, is the HTS machine design closest to a conventional machine where only a conventional field winding is replaced by an HTS field winding. The motivation for this concept was based on improved efficiency of large machines, since with HTS field winding excitation loss can be significantly reduced which would in turn make the machine more efficient. An advantage of this concept compared to the other HTS SM designs can be a simpler torque transfer since most of the developed torque acts on the warm steel and not on the HTS coils.

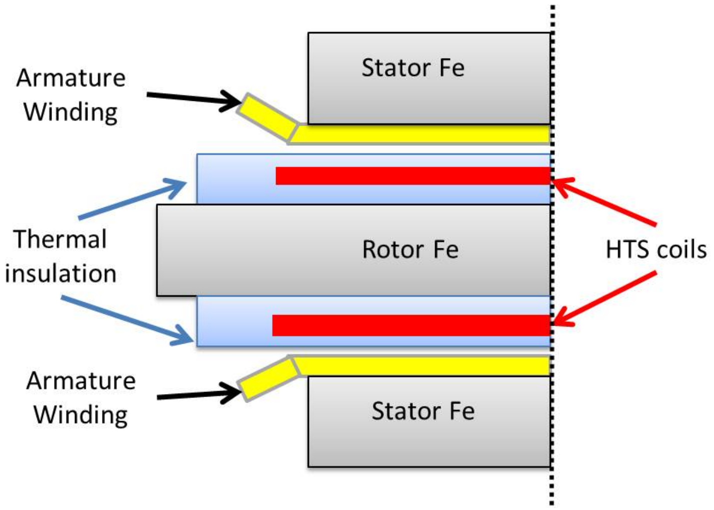

Figure 3.1: An illustration of HTS-SM design with warm rotor iron - The field winding is made of number of HTS coils (red) which are thermally insulated (blue) from the rest of the rotor. Thus, the rotor steel (gray) is at room temperature, same as are the armature winding (yellow) and stator steel (gray).

Demonstrations: An HTS SM with warm rotor In 2003, a 1.5 MVA HTS generator has been designed, built and successfully tested by General Electric as an engineering prototype for a 100 MVA turbo generator(55). The HTS coils in the 1.5 MVA demonstrators, wound with BSCCO HTS were designed to operate at 20K–40K (55, 56). A closed cycle helium refrigeration system was employed using GM cryocoolers (56, 57). The refrigeration unit and the helium transfer coupling used was a full size model needed for a 100 MVA generator (55, 57). Consequently, the design of the full 100MVA generator based on the constructed prototype is being finalized (55, 58).

In Europe, Converteam had undergone a construction of a 1.79 MW, 28 poles, 214 rpm hydroelectric generator(59, 60) which was actually a retrofit of old hydroelectric generator. The HYDROGENIE HTS generator is excited from a 1G HTS field winding cooled to about 30 K using high pressure helium gas(61) which is transferred from static cryocoolers (GM) to the rotor via a bespoke rotating coupling (62). The rotor steel in the machine is kept at room temperature while the armature winding is left unchanged, i.e. conventional slotted stator(61).

3.2.1.2 An HTS SM with cold rotor

An HTS SM machine design where the entire rotor is cooled down to operating temperatures of HTS is illustrated in Fig.3.2 and Fig.3.3. The difference between these two is the presence of ferromagnetic steel in the cold rotor. In the first design, an HTS field winding is wrapped around cold steel, while in the second an HTS field winding is mounted on a nonmagnetic support structure. In both concepts, a thermal insulation encloses the complete rotor. The latter is often called an air core HTS machine since the rotor holds no ferromagnetic material. The air core concept of HTS SM requires the highest amount of HTS (large MMF is necessary in absence of steel) but it is also the concept with highest power density (large weight reduction due to lack of rotor steel).

As a consequence of thermal insulation an HTS machine with a cold rotor will have a much large effective air gap (10 mm - 200 mm), compared to an HTS SM with warm rotor or a conventional machine. Consequently, the amount of MMF required to achieve considerable values of magnetic flux density at armature winding ($\geq$1 T) needs to be much larger than for the conventional machines. With such high values of MMF at rotor and dominant air nature of machines, electromagnetic parameters will differ considerably from what is found in the conventional machines.

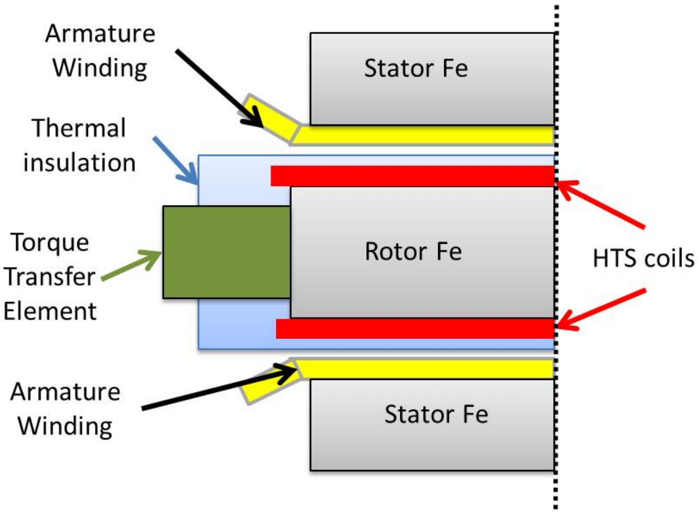

Figure 3.2: An illustrations of HTS SM design with cold (ferromagnetic) rotor - The field winding is made of a number of HTS coils (red) which are at the same temperature as the rest of the rotor. Armature winding (yellow) and stator steel (gray) are at room temperature. Additional element in the design is the Torque Transfer Element (dark green). The armature winding (yellow) can be either an air-gap winding or conventional slotted design.

In addition, for both designs where the entire rotor is cold, a few additional design specific elements have to be introduced. A Torque Transfer Element (TTE) is the structural element which is required to transfer rated torque from a cold rotor to a warm shaft. The developed electromagnetic torque needs to be transferred to a warm shaft (to either primary mover in case of a generator or mechanical load in case of a motor) this element will need to provide both mechanical strength and thermal insulation, objectives which are divergent for most structural materials. A torque transfer element design and concepts will be discussed in details later on, but it should be stated that its necessity in the design can significantly increase complexity of an HTS machine design.

An additional consideration for HTS SM with cold rotor is loss in the cold steel. Although a field winding and rotor steel are exposed to a main dc flux, in a machine operation some ac flux will be present. Any load change or spatial and time harmonics of flux linkage in a machine will cause some loss in the rotor steel (not a big loss and often neglected for conventional machines). Yet, due to a poor cooling efficiency, any

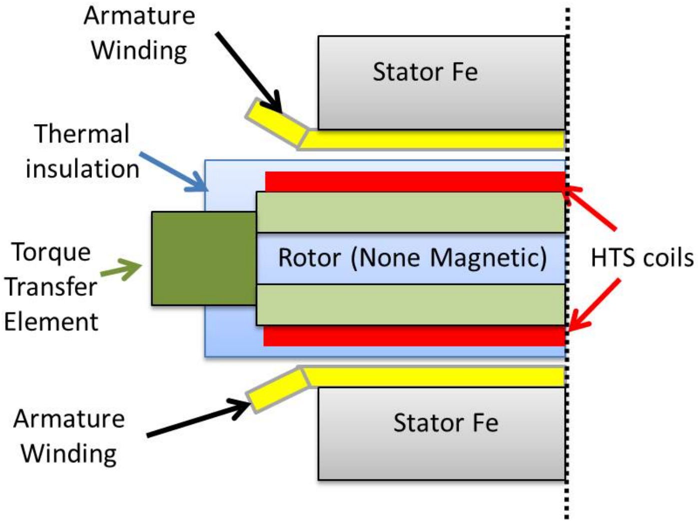

Figure 3.3: An illustrations of the "air core" HTS SM design - The field winding is made of a number of HTS coils (red) which are at the same temperature as rest of the rotor. A mechanical support for HTS coils (light green) is made from nonmagnetic material (stainless steel or composite material). An armature winding (yellow) and stator steel (gray) are at room temperature and Torque Transfer Element (dark green) is a mechanical interface between low temperature and room temperature. An armature winding (yellow) can be either an air gap winding or conventional slotted design.

(even small) loss dissipated at low temperature can become a significant load for a cooling system, and thus not negligible anymore. Several HTS machine designs(63, 64), particularly where high power density is an objective (65), have employed an air gap armature winding instead of a conventional winding placed in slots of stator steel laminates. In the following section advantages and issues tied to air gap winding are presented.

Demonstrations: An HTS SM with cold rotor Reliance Electric (Rockwell Automation) was the first company to start development of HTS motors in US(58).DOE funded projects for a 150 kW motor built and tested in 1996(66) and for a larger 750 kW motor tested in 2000(67). Both motors were 4 poles, 60 Hz machines using conventional slotted armature winding (54) (water cooled) with HTS field coils fabricated by AMSC (68) using BSCCO HTS conductor cooled by helium gas down to 20 K – 27 K.

Two HTS SM with cold rotor steel have been designed and constructed by Siemens (69). The first machine was 400 kW (64), 1500 rpm with HTS field winding made from

BSCCO coils, with an air gap armature winding. The machine was operated at 25K and cooled with GM cryocooler placed outside of machine where liquid neon served as a coolant media(65). The second machine, had a rating of 4 MW with an identical design concept also employing 1G HTS in the field winding (70, 71). Both motors were developed for ship propulsion as the primary application field and are being certified by Germanischer Lloyd (70).

Several machines were constructed in projects led by American Superconductor (AMSC). Among the first was a synchronous condenser, built to improve the power factor of power system (72). Rated at 12 MVAR, the machine had a 1G HTS field winding and an air-gap armature (73). AMSC also designed, built, and tested a 3.5 MW four pole, 1800 rpm machine (63). In this design, the whole rotor including coils wound with BSCCO HTS conductor was cooled down to 35 K using a closed cycle neon heat pipe concept (72). Under contract with the Office of Naval Research AMSC built two prototype motors (5 MW, 230 rpm motor (74) and 36.5 MW, 120 rpm motor (75)) as a power compact ship propulsion alternatives to existing ship propulsion concepts (74).The armature is liquid cooled with dielectric insulating oil. Both motors employed 1G (BSCCO) field windings cooled with GM cryocoolers and operated at 30 K.

The objective of the HTS 36.5 MW motor was the development of a full - scale, high power density, lightweight, advanced propulsion motor suitable for future naval applications. It employs many of the technologies developed for the 5 MW motor, including the HTS field winding, a high current density liquid - cooled stator, and the refrigeration, mechanical support, and excitation systems. This machine presents the highest torque HTS machine constructed up to date with an output shaft speed of 120 rpm, and over 2.9 MNm of torque and weight estimate of 75 tons which is proof of how difficult it is (but not impossible) to build compact high torque machines(54).

At University of Southampton a 2 pole, 100 kVA HTS SM with a cold rotor generator was designed and constructed in 2004 (76, 77). The HTS rotor is designed to operate in the range of 64 K – 77 K using either liquid nitrogen or air where coolant was introduced through a hollow shaft and rotating coupling (77). The field winding was assembled from a number of coils wound from BSCCO HTS conductor. The innovative approach in this design was handling a perpendicular magnetic field which would at higher operation temperatures constrain the current capacity of BSCCO coils to a high degree(78). The same generator was retrofitted into an air core configuration by omitting a ferromagnetic core(79) where also BSCCO coils were used and cooled by sub-cooled nitrogen(80).

A 1 MW, two pole HTS machine employing the BSCCO coils in air core configuration and air gap armature winding was designed and constructed at KERI (81, 82). The rotating HTS field coils were cooled below 30 K (83) by the cryogenic rotating cooling system which consisted of GM cryocooler and thermosyphon via neon circulated cooling system. Issues with ensuring desired degree of concentric alignment were reported (83).

Several plans have been put forward to design and construct a 10 MW wind turbine generator from the time the Superwind project started (2007). Converteam came first with an air core HTS SM machine using 1G HTS tape(84). AMSC has also announced intention to construct a wind turbine DD generator under the brand name SeaTitan(85). Construction of the proposed wind generator has not begun to date, as far as the author is aware.

3.2.1.3 Fully HTS-SM

There were several suggestions towards large utility fully superconducting generators using LTS (86, 87) and a very limited number of laboratory scale projects of fully superconducting machines using HTS conductors (88). The obvious advantage of fully HTS SM is higher electric loading of the HTS armature (89). In addition, if an armature and field winding operate at the same temperature, the air gap can be made much smaller and thus the whole magnetic design of the machine becomes more efficient. Nevertheless, the largest issue in this concept is the ac loss generated by the HTS armature. Since the HTS in the armature will be in the path of full flux (alternating with revolution of rotor), and will also carry ac current, the ac loss will be the dominant loss in the machine. At the moment, the amount of ac loss in high field ac application is regarded as prohibitive (54) due to a poor cooling efficiency. Several approaches are investigated in order to decrease the ac loss of HTS conductors (90, 91). A proposal for fully superconducting wind turbine generators (class of 10MW) has been put forth by Advanced Magnet Lab, Inc. (AML) using a Double-Helix technology and MgB_2 superconductor (92). Yet, no HTS full superconducting machine has been developed by industrial partners.

3.2.2 Other types of HTS machines

Several other HTS machines such as induction, switch reluctance, trapped field machines, dc homopolar machines and others suited for high power applications were demonstrated as well. Intended application for these was more focused on improvement or modification of machine operation characteristic (torque – speed, overload characteristic, etc.) than on to increase of torque density of such machines. A brief, overview of demonstrated projects of induction, switched reluctance, trapped field and dc homopolar machines are presented in the following section.

Induction machines with HTS conductors Induction machine designs published so far had only a HTS rotor squirrel cage (93, 94). In this way, a torque characteristic of an induction machine would have a different trend compared to a conventional machine, due to the ac loss in HTS bars, which is a function of slip (the higher the slip, the larger the rotor resistance) (95). Consequently, start and maximum torque of induction machine will become much higher (93) and due to very stiff characteristic (very small slip) the energy loss in the rotor can be very small (96, 97). However, the dominant ac nature of induction machines (even at slip frequencies for rotor currents) requires improved HTS conductors with respect to ac operation.

Switched reluctance machines If an HTS bulk material is introduced in a rotor, due to the flux screening effect of HTS material, flux path permence of d axis and q axis of a machine will differ, hence reluctance effect will be enhanced. Several demonstration projects were carried out where the latest one was a 400 kW motor with $NdFeB$ magnets and bulk HTS (YBCO) in four pole rotor topology which was successfully constructed and tested (98) where the rotor was cooled via liquid nitrogen at 77 K (99).

Trapped field machines HTS material can be regarded as a particular type of permanent magnet. If the magnetic field is trapped inside of HTS material, the HTS bulk would sustain the field for very long time. Maximal trapped flux density for bulk material would correspond to 1T – 2T at 77 K and 7 T – 8 T at 20 K (99). Thus, in principle this would be a very convenient way of designing an electrical machine, since these machines are very similar to conventional permanent magnet machines. However a number of issues need to be addressed such as magnetization techniques, stability of trapped field, ac loss and etc.

DC homopolar machines DC homopolar machines are based on Faradays disk machine (100, 101). It is a relatively simple machine design comprised of a dc magnetic field winding (usually simple solenoid) which creates an excitation field in axial direction. A conducting disk which presents a rotor is placed in such a way so both axial axis are aligned, thus the excitation field is perpendicular to the disk (54). Current will flow from the center of disk towards the outer radius where current collectors are placed at the edge of a disk and at the center of a disk. In this way current and magnetic flux are perpendicular; hence a torque is proportional to the product of current, flux and radius. Limiting issues in the design of dc homopolar machines (as well as for conventional dc machine) is the design of current collector, here even more so as the currents of the rotor are very large. With higher magnetic flux, rotor current becomes lower for the same torque; hence a collector has a simpler design. The first successful demonstration came with LTS in (102) a field winding wound by LTS. A 3.7 MW machine was designed and constructed as a prototype, where a preliminary design of a 36.5 MW generator is being developed for U.S Navy application by General Atomics (103).

3.3 HTS SM design considerations

A torque transfer element, an HTS winding and cooling system are the most essential aspects of an HTS machine design. Considerations with respect to the mentioned design aspects will be presented in the following sections. A state of the art low temperature refrigeration systems is reviewed where advantages and drawbacks with respect to potential wind turbine generator application for offshore wind turbines are discussed. Afterwards, a torque transfer element and its unique requirements are identified. The general guidelines are derived for geometry of this element regardless of material choice, which allows an optimized design to be applied for the design of an experimental setup. Finally, HTS coil topologies are discussed and magnetic anisotropy of an HTS coil is acknowledged.

3.3.1 Low temperature cooling system overview and thermal insulation

Refrigeration at low temperatures is an inefficient process. It is well known that the ideal Carnot efficiency can never be attained in practice. Since all practical cryocoolers work on the bases of compression and expansion of gases (usually helium), present cryocoolers are still a long way from Carnot ideal limit (104). A typical ratio for input work /output work for the temperature range 300 K to 30 K is approximately 100 to 1. This means that in order to obtain a 100 W of cooling power at 30 K, an electrical input power needs to be about 10 kW (50).

Several concepts of refrigeration can be used depending on the HTS machine concept and operating temperature. Often applied configuration is cooling in a closed cycle of helium with one or several cryocoolers where a coolant which can be either a gas or a liquid (nitrogen, oxygen, neon, hydrogen) is circulated between heat exchanger (cold head) and HTS coils. Since gas or liquid is possible to be transferred via rotating coupling between stationary cold head and rotating HTS coils, where either a thermosiphon or forced circulation of fluid is employed, this configuration has particular benefits for HTS SM machines and is by far the most readily used (58, 63, 82, 105). Instead of convection cooling, where fluid is the heat transport media, it is also possible to employ a conduction cooling where the HTS coils are in a good thermal contact with the heat exchanger (cold head) (106). Hence, a cyrocooler needs to rotate with an HTS winding. Presented concepts are considered as a standard solution where "off the shelf" cryocooler is employed. As an alternative to this concept, it is possible to use a boil-off of some of the gaseous with appropriate boiling temperature (T_{He} ~4 K, T_{H_2} ~20 K, T_{Ne} ~27 K and T_{N_2} ~77 K) where fluid absorbs the heat by phase transition (107). If the system is closed, a liquefier would be necessary in the cooling loop, otherwise an inflow of cooling fluid must be ensured (constant inflow of LN_2 for example). Gifford-McMahon (GM) refrigerator is the by far most often used cyrocooler used for low temperature cooling, while Pulse Tube refrigerators are looking very promising.

A Gifford-McMahon refrigerator Gifford-McMahon (GM) refrigerators are used in cooling thermal shields of low temperature superconductor MRI systems (cooled $\leq$ 4.2 K). Hence, it is considered to be a well established technology (65, 108). The refrigeration power of available models is limited to ~100 W at ~20 K, which suggest that for higher cooling requirements several cryocooler in parallel will be necessary. Efficiency of a cryocooler is relatively good, where for example AL325 GM from CryoMech has 100 W at 25 K for 11.2 kW input power (109) which gives a factor of ∼112 as cooling penalty. A GM cryocoolers have couple of drawbacks with respect to machine application. From the HTS machine application perspective oil-lubricated compressors and cold head moving displacers are considered weak links, both of which have high maintenance requirements (once annually). Also dependence of the orientation with respect to gravity can become an issue (65). Thus, GM cryocoolers are available and are not costly, yet they do require maintenance which is an issue for future offshore application.

A Pulse Tube refrigerator Pulse Tube refrigerators (PTR), developed as an alternative to GM, have no moving displacer in the cold head. Cost of PTR is considerably higher compared to a GM. In addition, the cooling efficiency is lower (e.g.the PT63 available cooling power at 30 K is 11.5 W for input power of 4.2KW (110)). Consequently, a cooling penalty becomes ∼356 which is substantially higher than GM. However, if an oil free linear compressor is employed (which is also a possibility in GM refrigerator systems), a cooling system with PTR could have a lower maintenance (once every 2 – 3 years) and longer lifetime (111). In addition, PT refrigerates can be highly susceptible to orientation (111) where operation with cold end down is a requirement (110). However, a development of Stirling type co-axial PT cryocoolers is encouraging since these are able to be incorporated on-board in rotating equipment (112). Substantial efforts are invested in development of PTR in order to make them more efficient and less costly (111, 113).

Thermal insulation Regardless of which refrigeration cycle is used, HTS coils have to be well insulated in order to decrease a parasitic heat inflow and minimize effects of poor cooling efficiency on the whole system efficiency. Consequently, a cryostat for HTS needs to be designed. For temperatures between 20 K – 80 K, a cryostat will probably need to have a vacuum insulation in order to minimize convection and conduction heat transfer. Depending on the HTS SM design concept, an additional requirement for cryostat and vacuum insulation is to be as thin as possible (an air gap is vital for machine design). To prevent radiation heat transfer, a Multi Layer Insulation (MLI) in the form of thin aluminum foils can be used as an efficient way to reduce radiation to an acceptable level.

The necessity of a low temperature cooling system is certainly one of the most prominent inhibiting factors for development of HTS machines and reluctance of industry to employ this technology. Thus, mastering and improving a low temperature refrigeration and thermal insulation technology is as important for HTS application as development of the HTS.

3.3.2 Torque Transfer Element (TTE)

The main candidate for achieving significant improvement of torque density is an air core HTS SM. This design needs to have an element that can transfer the full electromagnetic torque (both rated and fault conditions) from the cold rotor to the warm shaft of the primary mover. Hence, the heat transfer through the torque transfer elements needs to be minimized. A suitable name for this element could be Torque Transfer Element (TTE) which will be used through out this thesis. Torque tube is also a commonly used name in publications.

The mechanical strength and thermal conductivity are objectives, standing in contradiction for such an element. Although a TTE represents one of the essential elements in a design of a HTS SM with a cold rotor, surprisingly little has been published on this subject and the challenges it involves. It should be stated that the heat transfer through the TTE is a large contributor to the base load of the refrigeration system next to the current leads and radiation heat; hence its optimization is critical.

In LTS application for large turbo generators, two solutions have used stainless steel torque tubes, where the heat transfer is minimized with a flow of cold gas in the return path from the HTS coils towards the heat exchanger (114, 115, 116, 117). A TTE for HTS machines at Southampton, Siemens and AMSC was based on complex composite material elements. An obvious advantage of composite materials is a rather low heat conduction with strength comparable to that of steel. The fiberglass G10 TTE in the design of the 100 kW (∼320 Nm of rated torque) air core machine developed in Southampton consist of multiple parts, eight 180 mm long ”dog−bone−shaped” arms tapered by fiberglass bracing cone (105), where the total heat input (including current leads and heat transfer through the cryostat and TTE) was estimated to be 60 W (105, 118) at 77 K. A G-FRP (glass-fiber reinforced plastics) monolithic TTE was developed by CrossLink Faserverbundtechnik GmbH for Siemens for the 400 kW ship propulsion machine with ∼2500 Nm for rated torque and only 22 W of total cooling power requirements (119) at ∼30 K. An even more impressive accomplishment for the 400 kW machined design is the fact that the torque tube was able to sustain torques up to 37 kNm, which is ∼15 times higher than rated torque. This was required since the machine had very low synchronous reactance $x_d = 0.15$ p.u. which would cause large fault currents and forces. AMSC holds several patents regarding TTE, HTS rotor construction and design(120, 121), yet little information is available on details of solutions used in HTS machine demonstration projects AMSC led.

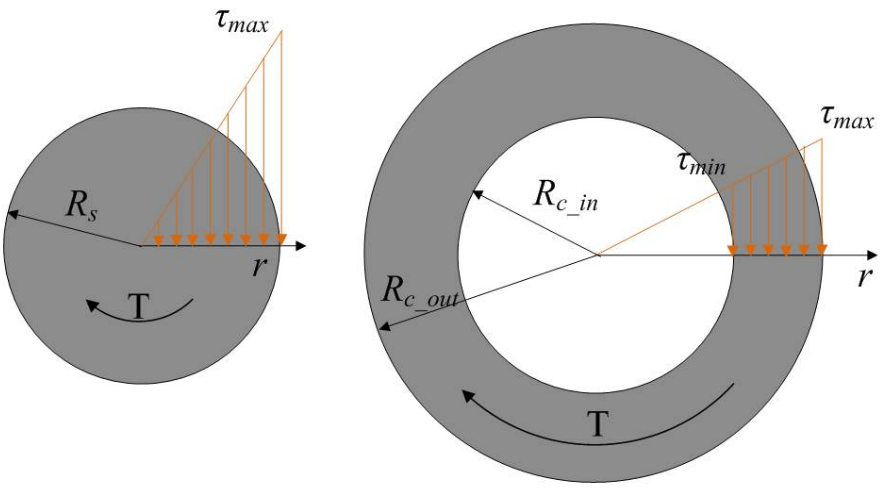

Figure 3.4: The stress distribution in the material - The stress distribution in the TTE for the case that the TTE is shaft or cylinder. The maximal stress will occur at the largest radius.

Thus, from this short overview one may get the impression that relatively little recommendation on general guidelines toward TTE design are available. With regards to material candidates for TTE, the composite materials (G10 and GFRP) showed advantages over structural stainless steel. However, the design of TTE is far from trivial and its importance in the design of high torque machines (with rated torque of 1 MNm) requires an even higher degree of optimization in order to minimize the cost of refrigeration.

3.3.2.1 Mechanical and thermal consideration for TTE

Regardless of which material is used, the guidelines for optimal TTE are necessary, such that will minimize the heat inflow while providing good torsion transfer capabilities. Let us assume that we need to design a simple TTE. As no complex shapes are of interest (only 2D analytical analysis will be used), a simple shaft and cylinder could be candidates for optimal TTE.

When exposed to the torsion torque, T, the stress distribution in the material is a linear function of distance from the axial axes around which the torsion acts. The highest sheer stress will always be at the largest radius (122). This is illustrated in Fig.3.4 for a shaft and a cylinder, two simple candidates for TTE. The relation between the torsion torque, T and maximal sheer stress in the material τ_{max} is expressed as

$$T = \int r dF = \int r\tau dA = \int r \underbrace{\frac{r}{R}\tau_{max}}_{\tau} dA = \frac{\tau_{max}}{R}\int r^2 dA \longrightarrow J\frac{\tau_{max}}{R} \tag{3.2}$$

were dF is the elementary force, dA is the elementary surface of the cross section, r is the distance from the center of the torsion and $J = \int r^2 dA$ is a polar moment of inertia for the particular shape of the TTE. R is the largest distance of material from the axis of torsion, hence $R = R_s$ in the case of shaft or $R = R_{c\_out}$ in the case of the cylinder. The relation $\tau/\tau_{max} = r/R$ was used in 3.2. To compare these two with R_s for a shaft radius and R_{c_out} and R_{c_in} for an outer and inner cylinder radius, respectively, both TTE will need to have same torsion capability. Using 3.2, the equal torque condition can be expressed as 3.3 where $J_s = 0.5\pi R_s^4$ and $J_c = 0.5\pi(R_{c\_out}^4 - R_{c\_in}^4)$.

$$T_{shaft} = T_{cylinder} \rightarrow J_s\frac{\tau_{max}}{R_s} = J_c\frac{\tau_{max}}{R_{c\_out}} \tag{3.3}$$

From 3.3, it is possible to express the shaft's radius as a function of the outer radius of the cylinder and the wall thickness, $\delta_{wall} = R_{c\_out} - R_{c\_in}$, as 3.4.

$$R_s^3 = \frac{R_{c\_out}^4 - R_{c\_in}^4}{R_{c\_out}} = \frac{R_{c\_out}^4 - (R_{c\_out} - \delta_{wall})^4}{R_{c\_out}} \tag{3.4}$$

From 3.4, by defining the ratio R_s/R_{c_out} as a function of δ_{wall}, we can identify "mechanically equivalent" candidates for TTE. If the wall thickness is normalized to the outer radius of the cylinder, equation 3.4 now expressed with 3.5 will become more general.

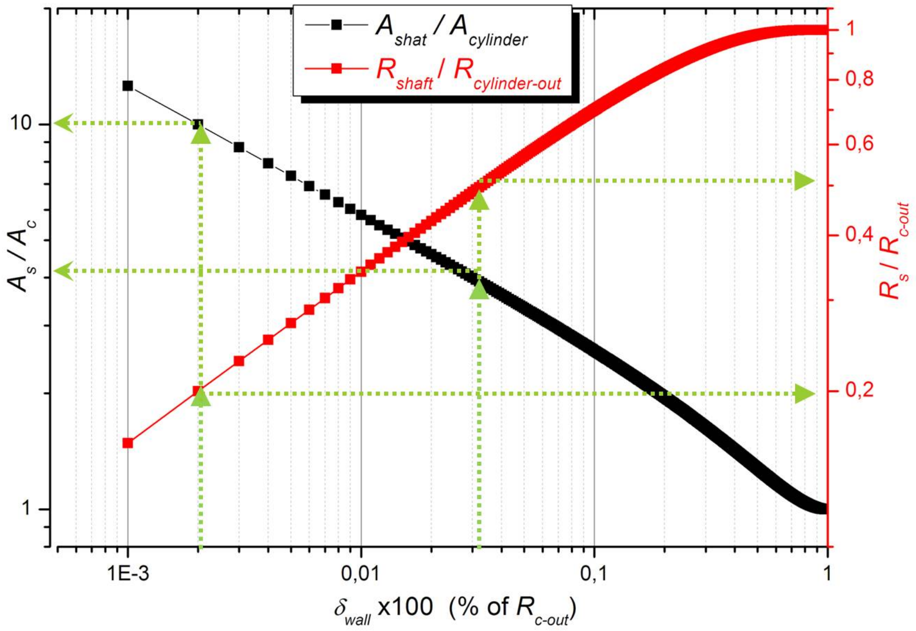

Figure 3.5: Comparison of the cross section area of a shaft and a cylinder with same torque transfer capabilities. - The derived ratio of the cross sections of a shaft and a cylinder with the same maximum sheer stress in the material when exposed to the same torque, as a function of the wall thickness of the cylinder normalized to the outer radius of the cylinder is presented with the black trace. The red trace defines the ratio of the radii of the shaft over the cylinder as a function of the wall thickness of the cylinder normalized to the outer radius when both are equally strong (same torque capability). Thus, the shaft with the same mechanical capability to transfer the torque as for example the cylinder with the radius (outer) of 1 m and wall thickness of 3 cm (which is 3% of the outer radius) would need to have radius of 0.5 m. This is indicated with the green dashed line going from 3% for the horizontal axis and reading the value for the red trace on the right axis. To compare now the heat conduction of these two, the value of the black trace for the 0.03 is found on the left axis for the black trace. The conclusion is that the shaft would have ≈4 time higher heat conduction. In the case of the TTE integrated in the Superwind cryostat design, the wall thickness is 2%.

$$\delta_{wall\%} = \frac{\delta_{wall}}{R_{c\_out}} \rightarrow \frac{R_s}{R_{c\_out}} = \sqrt[3]{1-(1-\delta_{wall\%})^4} \tag{3.5}$$

The next step is to define a ratio of cross sections, expressed by 3.6.

$$\frac{A_s}{A_c} = \frac{\pi R_s^2}{\pi(R_{c\_out}^2 - (R_{c\_out} - \delta_{wall})^2)} = \frac{\left(\frac{R_{c\_out}^4 - (R_{c\_out} - \delta_{wall})^4}{R_{c\_out}}\right)^{2/3}}{R_{c\_out}^2 - (R_{c\_out} - \delta_{wall})^2} \tag{3.6}$$

This ratio using the relation between shaft and cylinder radii defined by 3.4 can be used to estimate which of the candidates, equal in maximum torque rating, will have lower heat conduction. Similar to the previous case, with the same normalization here, the 3.6 can be reduced to

$$\frac{A_s}{A_c} = \frac{\sqrt[3]{1 - (1 - \delta_{wall\%})^4}}{1 - (1 - \delta_{wall\%})^2} \tag{3.7}$$

Fig.3.5 illustrates the ratio of the cross section surface of the TTE as a function of $\delta_{wall\%}$. Looking at Fig.3.5 it is obvious that for the same torque capability (the same maximal torque), a shaft will have larger cross section area compared to a cylinder. Fig.3.5 would imply that the largest possible radius for the cylinder as TTE would result in the lowest heat transfer regardless which material is used. In addition to heat transfer, the cylinder would make a lighter option too, since less material is used. In reality it would mean that the TTE should practically be at the same radii as the air gap.

3.3.3 An HTS field winding

The HTS field winding consists of number of HTS coils. Therefore it is important to understand the limitations of the HTS coils and see which configuration could be optimal for a HTS machine application.

3.3.3.1 HTS Coil design concepts

It is well known (from Ch.2) that both $1G$ and $2G$ HTS conductors are manufactured as a thin tape (0.1 mm – 0.4 mm thick) of different widths from 2 mm – 15 mm (where 4.2 mm is the most common) (1, 2). HTS tapes have specific mechanical constraints, which are necessary in order to preserve the superconducting properties of the brittle ceramic material. These constrains are usually specified in terms of maximal pitch angle an HTS tape can be exposed to, minimal bending radius and maximal strain (stress) after which degradation of the current capacity will occur. Due to all these mechanical limitations, the only practical coil design for winding HTS tape is a racetrack coil.

This is one of the reasons why it is, although not impossible, rather difficult to design a multi phase armature winding with racetrack coils for an all-superconducting

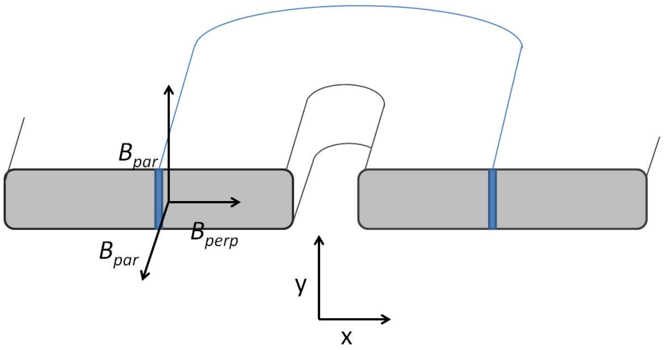

Figure 3.6: An illustration of HTS racetrack coil cross section - One turn of HTS tape is identified in the racetrack coil where prevailing perpendicular direction and parallel direction of flux are indicated with the local coordinate system

machine where the armature is superconducting as well. Insulated tape is wound into racetrack coils which are usually paired into so–called double pancake, thus creating a compact winding assembly. An HTS field winding comprises a number of racetrack coils, stacked together and connected in series.

HTS coils need to be designed and constructed in such a way as to ensure good cooling conduction for the HTS turns, and good mechanical support in both nominal and fault conditions. Finally, HTS field winding also needs to maximize the performance of the HTS tapes, and hence the field winding design should minimize the exposure of HTS turns to the magnetic field (particularly perpendicular to the turns).

3.3.3.2 Magnetic sensitivity of an HTS coil

It has been demonstrated in Ch.2, that the performance of the HTS conductor is sensitive to a magnetic field. It was also shown that 1G will exhibit a higher degree of magnetic anisotropy at higher temperatures compared to 2G HTS conductors.

If an HTS coil carries a current, magnetic field will have a certain distribution in space. Nevertheless, it is almost certain that the magnetic field will not be the same at each turn of a HTS coil. Thus, the turns will exhibit different critical currents. Depending on the particular case, some turns in the coil will be exposed to very large flux while others will be in no field. The critical current of a coil will be limited by the section of the coil with the lowest critical current, expressed as

$$I_{Coil} = MIN(I_c(L)) \tag{3.8}$$

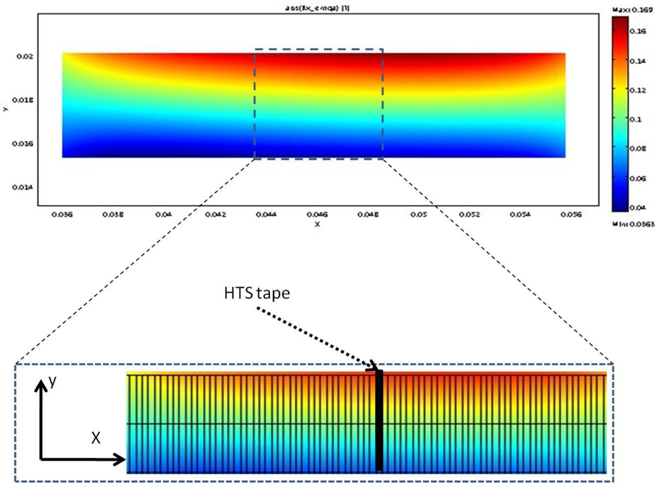

Figure 3.7: A 2D FE simulation of the flux density distribution of the HTS coil - An HTS coil carrying current will be exposed to either self generated and/or external magnetic flux (generated by other coils). The distribution of flux density will differ between turns.

where $0 \leq L \leq L_{Coil}$ and L_{Coil} is length of the HTS tape in the coil. Otherwise, some sections could carry currents above the critical value, which could put them in risk of quench. The same thinking applies for a stack of coils where the coil with minimal critical current will set the current of a coil stack. Therefore, in a good design of HTS field winding there is an effort to minimize the exposure of HTS coils to the perpendicular flux and thus increase available MMF of the field winding. Instead of 3.8, in practice the coil current is derived from the coil voltage which is composed of multiple turns. More on the effects of non uniform flux distribution will be discussed in Ch.5 where the experimental results are presented.

3.4 Electromagnetic model of HTS SM

The difference between a conventional and an HTS machine concept was clarified in the previous section. The next step is to understand the difference between electromagnetic parameters of conventional and HTS machines. The cold rotor HTS SM represents the concept of HTS machine with the highest potential for torque density increase and thus could also be a potential concept for a DD wind turbine generator.

Due to the absence of iron in an air core HTS SM or a large air gap caused by a

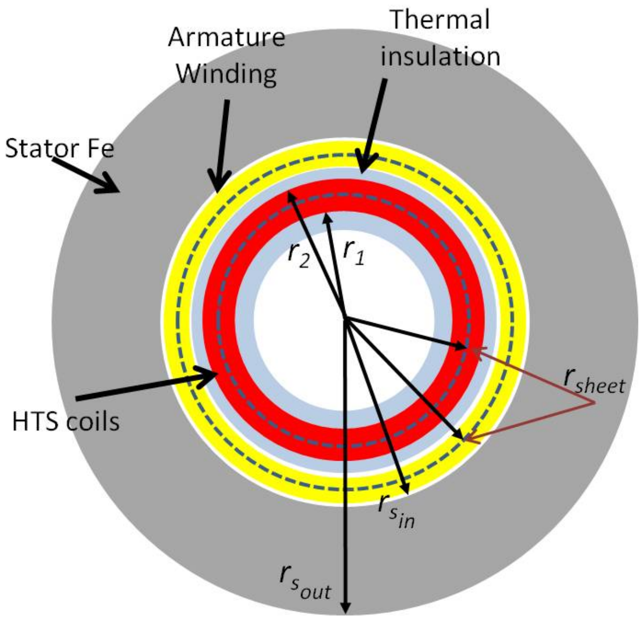

Figure 3.8: Illustration of the generic cross section of the HTS SM - The air core HTS SM machine with the armature winding (the yellow ring) and HTS field winding (the red ring) enclosed by the thermal insulation (the blue rings) is presented. The stator back steel is presented by the gray ring with radii $r_{s_{out}}$ and $r_{s_{in}}$. Each winding can be approximated by the infinitely thin current sheet at radii r_{sheet}.

thermal shield, the traditional approach of magnetic permenace of magnetic circuit of an electric machine is inapplicable (52, 53). The flux across the air gap in an air core machine is not only radial, as assumed for a conventional machine. Consequently, the distribution of magnetic flux density cannot be assumed constant in the air gap but rather a function of the radial distance. To evaluate the radial distribution of flux density, analytical formulation of magnetic flux distribution generated by the current sheet approximation of windings (both armature and field winding) is used. A derivation of the current sheet approximation for HTS field winding is presented in Appendix.**??** and discussed in more details in (4). The discussion on the nature of inductances of an air core HTS SM is presented next, followed by analysis of the impact an armature reaction has on the HTS is recognized which will be the base for the experimental verification of this effect. The flux density distribution expression assumes the geometry of an air core HTS SM illustrated in the Fig.3.8.

3.4.1 Flux density distribution

Vector potential formulation A_z of Maxwell equations is a convenient way to derive analytical expressions for spatial flux distribution in a machine. The method was presented in (52) and adopted here. In the formulation, the authors have assumed an infinitely thin current sheet at radius r_{sheet} with harmonic current distribution along the circumference $A_{(\theta)} = A_{sheet} sin(p\theta)$. The method presented in (52) is extended with the derived current sheet approximation for HTS winding representation.

The radial magnetic flux density distribution of the current sheet enclosed by the stator back iron is presented in 3.9. Saturation and "end effects" are not included in this approach even though iterative procedures were proposed by other authors where the saturation could be included (123). For $r_{sheet} < r < r_{s_{in}}$, the radial flux distribution can be expressed as

$$B^{\nu}_{(r,\theta)} = \frac{\mu_0}{2} A^{\nu}_{sheet} \cdot \underbrace{\left[\frac{r_{sheet}}{r}\right]^{(\nu p+1)} \left(1 + \eta_s \lambda_s \left[\frac{r}{r_{s_{in}}}\right]^{2p\nu}\right)}_{K^{\nu}_{(r,p)}} \cdot cos\left(\nu p \theta\right) \tag{3.9}$$

or as

$$B^{\nu}_{(r,\theta)} = \frac{\mu_0}{2} A^{\nu}_{sheet} K^{\nu}_{(r,p)} \cdot cos\left(\nu p \theta\right) \tag{3.10}$$

where μ_0 is the permeability of vacuum. The ν is the harmonic order and p is the number of pairs of poles. A_{sheet} is the electrical loading of the current sheet at radius r_{sheet}. If the radial flux density distribution of the armature winding is to be investigated, the current sheet approximation at armature radius should be used (dashed line in yellow ring in Fig.3.8). The radii $r_{s_{in}}$ and $r_{s_{out}}$ are inner and outer radius of the stator back iron. The tangential component of flux density has the same expression as 3.9, where sin is used instead of cos. The influence of the stator back iron on the flux density of an current sheet is seen throughout parameters λ_s and η_s, defined by the 3.12 and 3.11 respectively, where μ_s is the relative permeability of the stator back iron.

$$\eta_s = \left[1 - \left(\frac{r_{s_{in}}}{r_{s_{out}}}\right)^{2p\nu}\right] / \left[1 - \lambda_s^2 \left(\frac{r_{s_{in}}}{r_{s_{out}}}\right)^{2p\nu}\right] \tag{3.11}$$

$$\lambda_s = \frac{\mu_s - 1}{\mu_s + 1} \tag{3.12}$$

The distribution of the flux density for the $r < r_{sheet}$ will be the same as 3.10 with one difference in $K^{\nu}_{(r,p)}$, which is expressed as 3.13

$$K^{\nu}_{(r,p)} = \left[\frac{r_{sheet}}{r}\right]^{(1-\nu p)} \left(1 + \eta_s \lambda_s \left[\frac{r_{sheet}}{r_{s_{in}}}\right]^{2p\nu}\right) \tag{3.13}$$

3.4.2 Nature of inductance of an air core HTS SM

The air core HTS SM is considered to be the main candidate for lightweight machines, hence interesting for wind turbine generators. Due to the lack of iron and air-gap armature, the synchronous reactance of an air core HTS machine will be lower than the inductance in conventional machines. Therefore, it is interesting to make a comparison between machine concepts and the nature of the synchronous inductances. The value of synchronous inductance (in p.u.) can be expressed as a function of the magnetic field that the armature current sheet would create at the radius of the armature current sheet (52, 53). For an air core machine, if the armature winding is presented as a current sheet (same as above), the expression for synchronous inductance in p.u. would be (52)

$$L_{(air-core)} = \frac{\mu_0 k_w}{\sqrt{2}} \frac{A_{sheet}}{B_{sheet}} (1 + (\frac{r_{sheet}}{r_{s_{in}}})^2) \tag{3.14}$$

while for the conventional machine where g would stand for the air gap, the synchronous inductance can be expressed as (52)

$$L_{(conv)} = \frac{\mu_0 k_w}{\sqrt{2}} \frac{A_{sheet}}{B_{sheet}} (\frac{2r_{s_{in}}}{g}) \tag{3.15}$$

For example, the values for L_d for SM in MW class can be between 1.5 p.u. – 3 p.u. (124). In MW class conventional machines, the air gap is much smaller than the radius of armature winding. Thus, it is clear what kind of effect a small air gap has on L_d from 3.15 where for 2% air gap, $2r_{s_{in}}/g$ would be 100. In the contrast to a conventional machine, there is no air gap in the air core machine. The amplification factor $(1 + (r_{sheet}/r_{s_{in}})^2)$ would be 2 at most when the armature winding is placed closest to stator back steel, i.e. $r_{sheet} = r_{s_{in}}$. Consequently, it is obvious that air core machines will have an order of magnitude lower inductance than conventional machines. This certainly presents the largest difference between a conventional and an air cored HTS SM.

It is essential to understand that an increase in power density of a machine will go hand in hand with the decrease of the inductance. Thus, if future wind turbine generators are required to be compact machines, the expected value of inductance would be much lower than conventional machines have. However, this is only true if the air gap flux density is increased while electric loading is either kept constant or decreased. In the case of a full HTS SM, the electric loading can be significantly increased. The effect of increase of the electric loading on the inductance is opposite. Hence, if the ratio A_s/B_r is maintained constant or increased, the power density of the machine can be increased while the values of inductance can be adjusted to more acceptable values.

Note: Consequences of low synchronous inductances for machines can be seen in outstanding transient and overload capabilities and better voltage and power control due to inherently low load angle value (70, 74, 75, 77). Yet, it is important to say that low values of synchronous inductances would cause large short circuit currents. For example, if $x_d = 0.1$p.u., the protection system (breakers) would need to be rated for an order of magnitude higher than the rated value. In other words, having the increase of torque density of a machine will result in smaller a machine but at the same time will require an elaborated protection system which will need to be greatly oversized. Thus, for real world application the whole system needs to be considered and not only machine size and cost.

Additional complications in the design phase of HTS machine will arise from the large values of transient forces and heat dissipation, which will in turn call for more structural reinforcement in the design (75, 119). Therefore it is important to look at the HTS SM machines not as a substitute for conventional machines but rather as a unique component with a list of specific requirements.

3.4.3 Armature reaction effect on an HTS field winding

Due to the magnetic sensitivity of the HTS tape, the field winding critical current will be reduced. Thus, the field winding will be characterized by the magnetic conditions in the machine. However, since an interaction of two magnetic fields of the rotor and the stator is the grounds for operation of the electric machine, the effects the armature winding will have on HTS performance must be evaluated as well.

Operation of the machine (air core HTS SM) is accessible by the analytic model presented above. If two current sheets are at the HTS field radius and at the armature radius, operation of the machine depend on the amplitude of the magnetic flux density generated by the field winding current sheet, electric loading of the current sheet the armature winding has an angular displacement between these. Hence the torque developed by the interaction between the rotor and stator magnetic field can be estimated by 3.16.

$$T(\theta) \sim B_r cos(p\theta) A_s sin(p\theta + p\gamma) \rightarrow T(\gamma) \sim B_r A_s sin(p\gamma) \tag{3.16}$$

The impact an armature has on the HTS field winding will depend on the ability of the armature reaction to alter magnetic conditions the HTS field winding is in. Thus, the flux density generated by the armature current sheet at the field winding can be used to quantify this change (for flux distribution expression consult (52)).

Two aspects the armature reaction has on HTS field winding can be recognized. The first is the intensity of armature reaction, where the stronger it is the larger effect it will have on the flux distribution and thus on HTS operation. The second is angular displacement, $p\gamma$, as this will disrupt the flux distribution at the HTS field winding. The latter is the consequence of magnetic anisotropy of the HTS field winding.

Fig.3.9 illustrates the effect of the number of pair of poles on the angle between an armature reaction and perpendicular direction of flux to HTS turns. As this angle will scale as $\sim (p\pi)/2$, the impact of armature reaction is expected to be most severe for the two pole machines.

The effects of armature reaction on HTS field winding have not been discussed in published material in a systematic manner. An exception to this is the excellent work done in (77) where the authors investigate the angular dependence of armature reaction on the HTS field winding, but since the machine design took advantage of flux diverters placed between coils, the conclusions derived in this work cannot be used as a general statement true for all cold rotor HTS SM machines. In work reported by (56, 64, 70), aspects of armature reaction in fault conditions and with respect to quenching of the HTS field winding have been reported.

As an effort to address this important aspect of an HTS machine, this thesis will experimentally investigate the effect that armature reaction has on the HTS field winding in normal operation which includes both intensity of the armature reaction and the

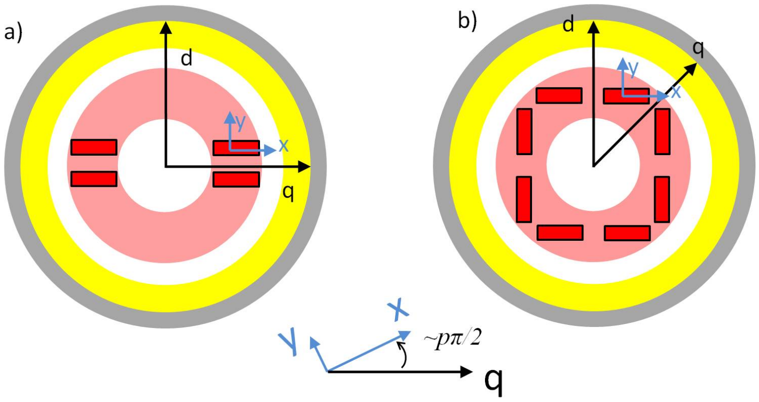

Figure 3.9: Difference between two pole and multipole machines - The air core HTS SM machine with the armature winding (the yellow ring) and HTS filed winding (the red ring) for (a) p= 1 and (b) p= 2. The HTS coils, the d and q axises and local x and y coordinate of HTS turns are presented. The figure illustrate that the angle between the x axis (perpendicular flux direction) of an HTS coil and the q axis will depend from number of poles, i.e it will scale $\sim p\frac{\pi}{2}$.

load angle γ between these. The experimental setup is designed and constructed with the specific purpose to investigate this interaction, where description of the setup and experiments is presented in Ch.4 while results are presented in Ch.5.

3.5 Suggested methods for increasing an HTS winding performance

HTS tapes are costly and any means to minimize the usage will be appreciated in an application where large amounts of HTS are required. Two design strategies have been proposed and investigated as an approach in order to better utilize the HTS tapes and ultimately to increase the MMF of the HTS field winding. The first proposed approach is to employ multiple types of HTS tapes assuming that the optimal composition of different types of HTS exists. The second approach investigates improvements due to multiple current supplies to the field winding. Both approaches will be discussed in coming sections while quantification of potential improvements of each approach will be deduced experimentally. The experimental results for the proposed concepts and degree of improvements achieved in the experimental setup will be presented in the following chapters.

3.5.1 An HTS field winding with 1G and 2G coils

Combining different superconductors as an idea comes from magnet technology where hybrid high field magnet design (125, 126) take advantage of LTS and HTS coils working together. A number of insert coils (one or two) are usually placed in the bore of a larger magnet which provides a background field on which the insert coils will build on. Since an HTS is sensitive to magnetic field, the performance of insert coils is adapted to the magnetic conditions inside the magnet bore.

The same approach can be used for electric machines where an objective could be to minimize the cost of machine which is in tight connection with amount of HTS used. Fig.3.10 illustrates a simple case of a field winding formed from a stack of HTS coils. Coils on the left are wound with only one type of HTS tape and the coils on the right are wound with multiple types of HTS conductor. Cumulative HTS machine experience and demonstration projects reported so far have employed either 1G or 2G HTS or a bulk material. As far as the author is aware, no systematic analysis of combination of HTS types used in HTS machines is performed so far. This thesis will investigate the potential benefits of combining 1G and 2G coils in the field winding. In principle, this approach next to HTS could be extended to include also MgB_2 (due to cost and availability) as a viable candidate for systems where operation temperature allows it.

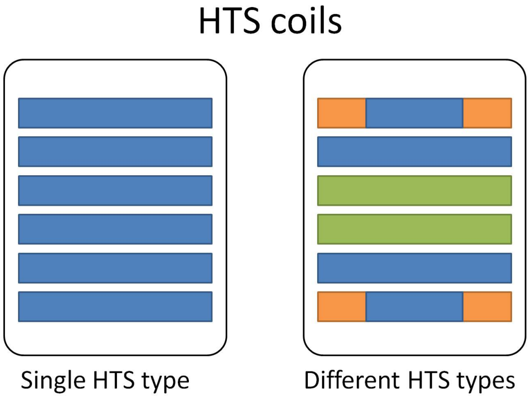

Figure 3.10: An HTS field winding comprising single and multiple types of HTS - Illustration of an HTS field winding where the possibility of using multiple HTS types are investigated. The single HTS tape (one color) winding presented at left is the conventional approach, while the concept at the right presents the hybrid concept employing multiple types of HTS tape where each color stands for types of different HTS.

Tape manufacturers are investing efforts to create HTS conductor which is less sensitive to magnetic field (improved pinning) and at the same time has higher uniformity with respect to the angle of the external magnetic field (127, 128). However, tapes highly sensitive to magnetic field (like 1G) produced at low cost used in combination with HTS tapes less susceptible to magnetic field could result in lower overall cost of the system (field winding).

The most convenient way to include multiple types of HTS in a field winding is to differentiate between different coils. Thus, inner coils would be wound with one type while the next layer can be another type of HTS. With a higher degree of complexity, benefits to MMF could be achieved if the coils could have insert coils from different tapes or if they are simply wound with two types of HTS, one continuing on the next one. Connection points of two HTS types need to be carefully engineered as superconductivity is interrupted and a resistive joint is introduced (129). By taking advantage of magnetic sensitivity and anisotropy of different types of superconductors and a degree to which they differ, an optimal composition of superconductors could lead to significant savings in HTS material. Thus, less costly 1G tapes which are highly sensitive to a magnetic field could be used in the field winding where the flux is low, while less sensitive and more expensive 2G tape could be placed in high flux conditions.

An additional parameter to consider on the path toward optimal field winding is the electric insulation of the HTS tapes. Electric insulation could have a prevailing effect on the design of HTS coils and engineering current of the coils and it can be used to adjust MMF distribution of the field winding. Compact coils can employ an insulating coating adhered to the HTS tape (only 0.05 mm – 0.1 mm thick) which would allow the highest values of engineering current density.

3.5.2 An HTS field winding with multiple power supplies

By allowing a number of power supplies to supply currents to the field winding, the critical current of each coil could be reached and thus the full capabilities of the HTS tapes can be utilized. This scheme for the excitation system of an HTS machine represents adaptation of practice found in magnet technology where for insert coils separate supplies are usually employed (126, 130). Proposed concepts are presented in Fig.3.11.

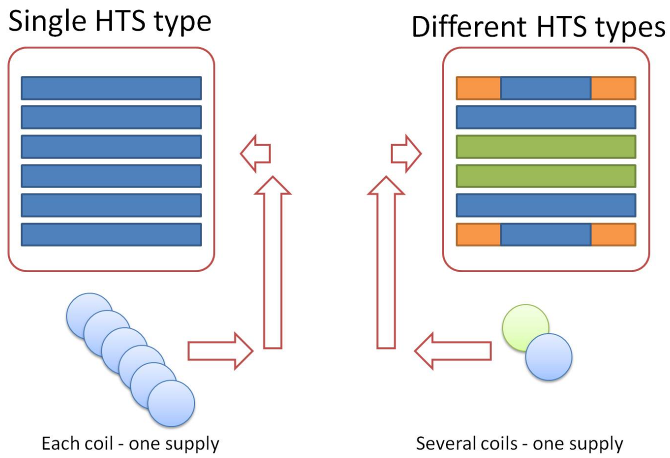

Figure 3.11: Supply schemes for an HTS field winding - Most flexibility and thus an increase in performance of HTS winding is achievable by assigning one power supply to one coil (left). By optimizing the number of power supplies improvements can be achieved as the increase of the performance will not scale linearly with the increase in number of power supplies.

This method, suggested as a means to boost the performance of magnets (131), where 30% improvements in MMF was observer, is not seen as an applied practice for a supply scheme of an HTS field winding.

Next to providing an increase in MMF of the field winding, additional power supplies will present additional cost and complexity. Although the power rating of excitation system is not increased, a one multi terminal dc source or several single output sources are required which cause the increase in the cost of auxiliary systems of HTS machine. However, reliability of the HTS excitation system will increase together with introducing additional power supplies. If a fault happens in one of the coils depending on how much power supplies are present in the excitation system the machine could still operate with partial output.

3.5.3 Proposed optimization approach

The concept of topology optimization was applied to an HTS machine (implemented and carried out in 2D FE) in order to maximize the effectiveness of the HTS current capacity. Here, instead of optimization of each coil geometry and afterwards a coil stack (shape optimization), which is the traditional way optimization is carried out in magnet technology (132) on MRI and high field magnets, the optimization algorithm controls the material distribution. An illustration of the concept is presented in Fig.3.12, comparing the traditional optimization approach and topology optimization.

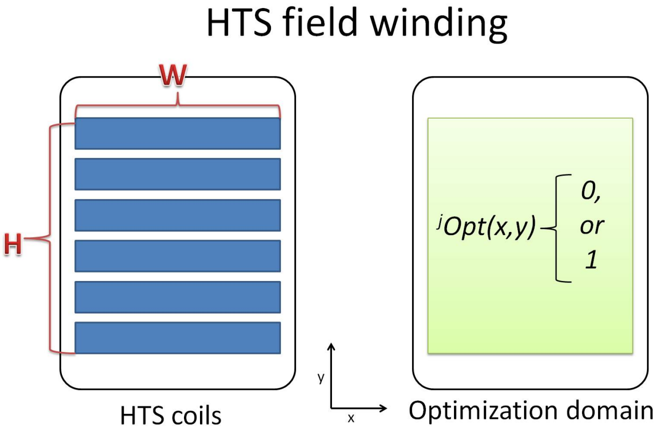

Figure 3.12: Optimization approach - The shape optimization, presented at the left, is conventionally used in various optimization problems including HTS magnets. As an alternative in the topology optimization approach, presented at the right, the algorithm is in charge of the material distribution.

Thus, if an optimization variable is defined in an optimization domain which is corresponding to the space allocated for HTS coils, the value of that variable could correspond to the material distribution. If the value of the variable is 1, the HTS conductor is present and carries current, while a 0 would correspond to an empty space (inactive material). The optimization algorithm needs to evaluate the objective function which contains all boundary conditions for the optimization problem and determine what distribution of HTS material would be the best. The amount of HTS can be included in the objective function and thus minimization will result in the lowest amount of HTS where defined constraints, which could be air gap flux density, electromagnetic torque or similar, are kept in defined bounds. Since two values for optimization variable are of interest, 0 and 1, the problem could be constrained to only binary variables.

Proposed optimization, described in (133) (included in the Appendix.**??**), was implemented in a 2D model of multipole (16 pole) HTS SM in Comsol Multiphysics (134) presented in Fig.3.13a. The paper presents formulation of topology optimization in Comsol Multiphysics for several types of HTS and multiple current supplies which will

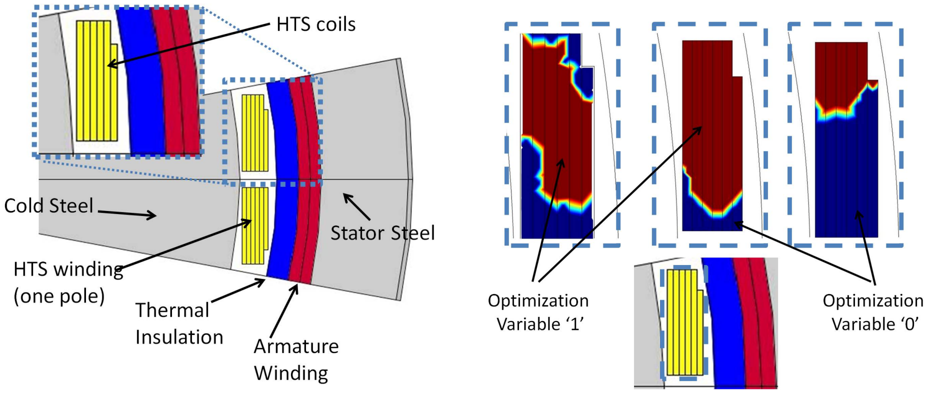

(a) The 2D model of 16 pole HTS generator

(b) Results of optimization

Figure 3.13: Implementation of topology optimization of HTS coils in Comsol MultiPhysics - **(a)** Only one pole of the 16 pole generator is modeled. **(b)** Optimization returned proposed distribution for an HTS conductor where the dark red is where the conductor is present while the dark blue the area where conductor is absent. The figure includes three different cases for three different HTS types.

not be presented here. The results for three different HTS types, presented in Fig.3.13b with different costs and $J_c(B)$ have been obtained where the tape with lowest cost produced the cheapest solution but also had largest volume of the coil.

The highest possible reduction of HTS for infinite number of power supplies (each turn has different current) for presented model 2D model was reported in (133) to be 50% for 2G and 30% for 1G HTS at 20 K. These values should be taken as indication to how much of HTS conductor is not fully utilized in field winding and hence the potential of multiple power supplies approach.

However, presented optimization approach and results are only initial step. The built–in optimization algorithm in Comsol was unable to handle binary values of optimization variables. Thus, this had to be addressed throughout the contributions to the global objective function, where a number of contributions have been defined in order to force the optimization variables to either 0 or 1. Unfortunately, this interfered with optimization process (evaluation of sensitivity based on gradient of objective function) and proved to be a limiting factor of described implementation. However, if an optimization engine capable of handling binary variables (like Branch and Bound) is employed, the presented optimization can become a valuable means for achieving an optimal layout of HTS machine.

Chapter 4

Superwind–HTS machine setup

"If at first the idea is not absurd, then there is no hope for it." **by Albert Einstein**.

4.1 Introduction

As a part of the effort to assess the state of the HTS technology and its application challenges in the wind industry, we have designed and constructed a small scale experimental HTS machine test platform. The focus during the design process was on creating the setup where various HTS tapes, coils, their performance and handling as a part of an electrical machine could be evaluated.

The coils wound from HTS tapes produced by several manufacturers, both 1G and 2G technology, have been tested as a part of an HTS field winding in the HTS machine. A modular approach during platform development was of crucial importance. It was important to design a versatile HTS machine platform where modification to the HTS field winding like interchanging the HTS coils, trying out different connections strategies of the coils, etc. is a straightforward task completed in a couple of hours.

The setup, illustrated in Fig.4.1, is comprised of a three phase armature winding rotating around a stationary HTS field winding operated at 77 K. The HTS field winding is immersed into a LN_2 chamber of the custom made cryostat which in this stage is operated as an open LN_2 bath. The setup is also equipped with the custom angular

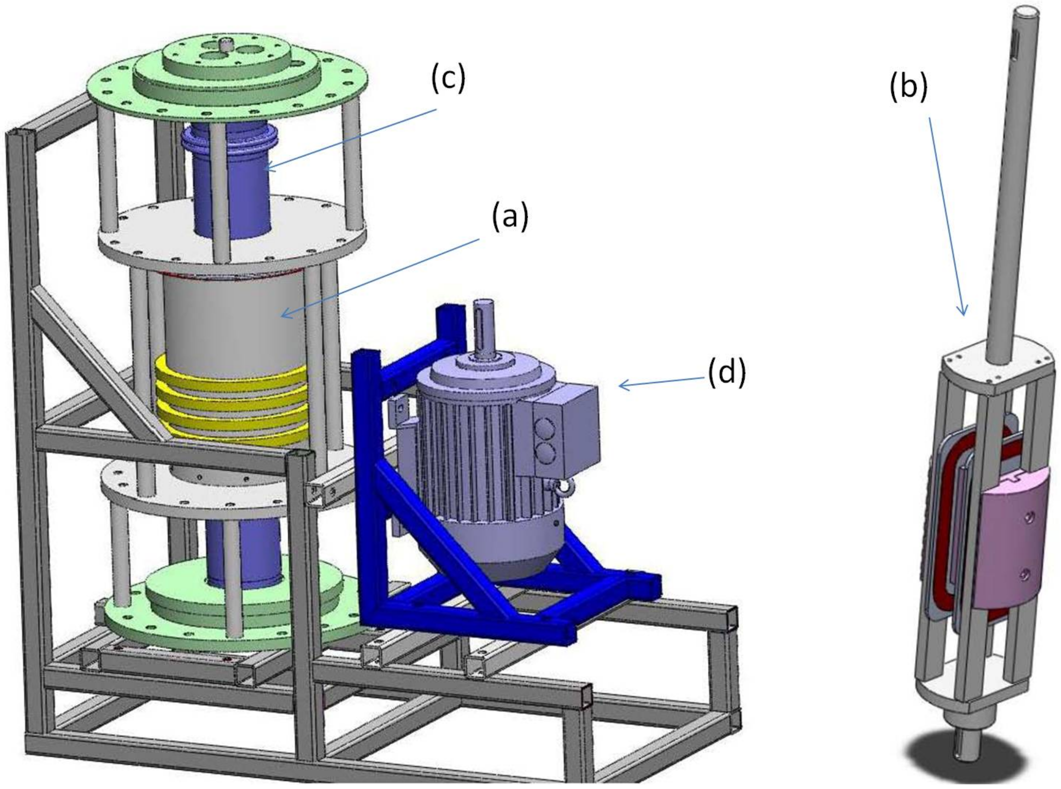

Figure 4.1: 3D CAD model of the Superwind setup and HTS field winding. - The armature winding, (a), is rotating around the HTS field winding (b) which is enclosed inside an open top LN_2 cryostat, (c). The armature is driven by the belt coupled induction motor, (d), controlled by a frequency converter. The belt connection is not shown. The assembled HTS field winding, (b), is lowered to the LN_2 chamber from the top of the cryostat.

position and speed measurement of the rotating armature as well as the stationary torque measurement. The armature position can be locked with respect to the HTS field winding and the angle relative to the armature can be adjusted in the 360° span.

The speed of the armature winding is controlled by the frequency converter driving the induction machine (it is an open loop U/f control of the induction machine). The induction machine is coupled to the armature winding by a belt. The speed reference is set manually by entering the desired value of the speed into the frequency converter control panel.

Data acquisition and control of the HTS field winding, supplied with six HP power supplies, is controlled by LabVIEW software. Schematic illustration of the data ac-

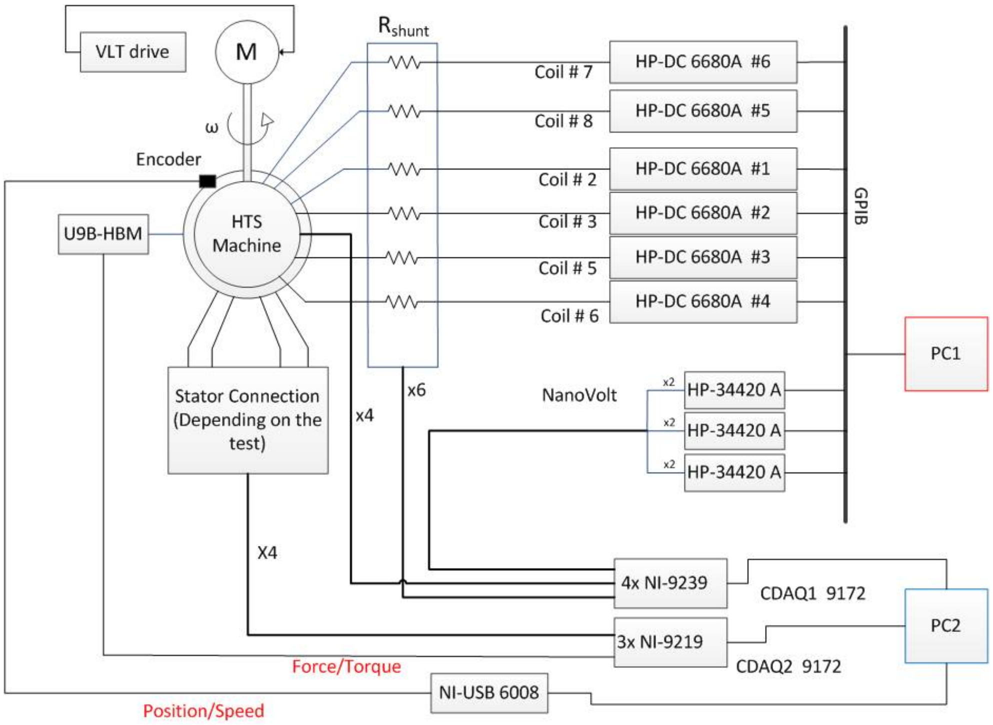

Figure 4.2: Schematic of the Superwind setup auxiliary equipment - The figure illustrates the measurement and control setup used in tests performed on the HTS machine with six dc power supplies. PC1 was used to control the dc power supplies (HP#1 – HP#6) and read the Nanovoltmeters (due to low sampling speed of Nanovoltmeters (one sample/s) the data from the Nanovoltmeters were used only in the case of static experiments). PC2 continuously reads the NI cards with high sampling rate (100 samples/s for NI9219 and 5×10^3 samples/s – 20×10^3samples/s for NI9239)

quisition is illustrated in Fig.4.2. The data acquisitions is performed with 24 bit NI measurement modules NI9239 (135) and NI9219 (136) characterized with simultaneous sampling, high voltage sensitivity and high sampling speeds.

4.2 The armature winding

Design and construction of HTS machine can be very costly due to the number of expensive elements, complex designs and uncertainty related to the low temperature operation and HTS where several iterations in designing phase might be required. Thus, we have decided to keep the focus on the HTS specific issues and to try to address challenges such as cryogenics (insulation), HTS coils design and others, so we could maximize the learning potential relative to the amount of funds invested. Hence, instead of designing and constructing an armature winding corresponding to the design of the HTS field winding (where for example air gap armature winding concept could be used), we have adopted the conventional armature winding from commercially available induction machine. At the later stage, a specific armature winding design could be incorporated in the setup without major complications.

The three phase two pole armature with distributed windings was adopted from a 22 kW, 50 Hz induction machine and custom fitted to a metal cylinder which acts as housing for the armature. Two bearings (137) are placed at the base of the armature bore. The armature winding is designed to rotate in order to avoid challenges of having the rotating parts at cryogenic temperatures. Thus, four slip rings are mounted on the bore making the phase and neutral terminals (for a star connected armature winding) accessible via four brushes. The armature winding is driven with an induction machine drive controlled by a *Danffoss* frequency converter (15 kW (138)) and coupled with a belt transmission. The speed range can be adjusted to any value between 0 – 400 rpm (limit imposed by the choice of bearings and the driving motor).

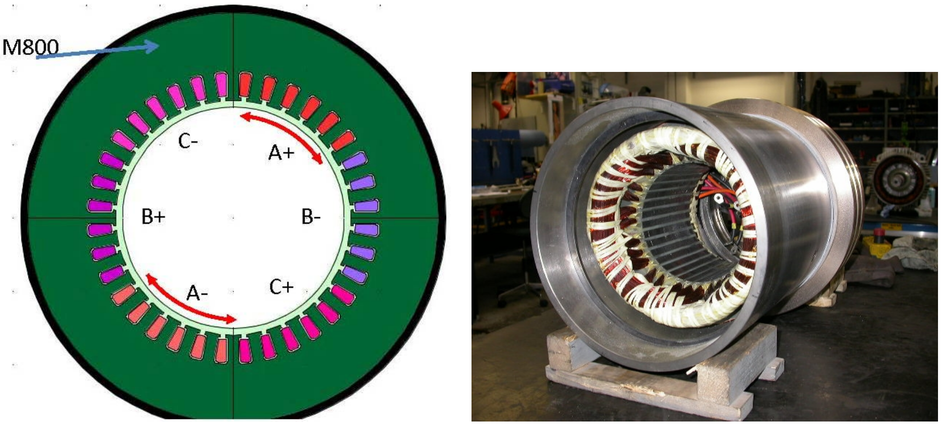

(a) Illustration of the armature winding **(b)** The armature in the metal housing

Figure 4.3: The armature winding. - **(a)** A 2D cross section of the three phase armature winding. The phase belts, occupying six slots per pole, are identified. **(b)** The armature winding during the construction phase. The metal housing, armature winding, 4 slip rings glued to the armature housing, bearing slot and 'O' ring are shown in the photo.

The geometry of the armature steel stack and windings has been inspected and it is illustrated in Fig.4.3a. The steel stack of M800-50A silicon steel (139) has axial length of 150 mm and rotor diameter of 160 mm. The phase windings are distributed over 36 stator slots in a single layer winding. The nameplate data and parameters of the induction machine from which the armature winding was adopted are presented in Appendix.**??** while technical drawings are included in Appendix.**??**.

4.2.1 The number of turns in the phase winding

The number of turns in the slot of the armature winding was not among induction machine documentation and thus it was determined experimentally. The AC power supply has been connected to phase A and B while a Rogowski current transducer *CWT015* (140) was wrapped around the turns in two slots. The placement of the Rogowski transducer is shown in Fig.4.4. The same arrangement has been repeated but now with Rogowski transducer wrapped around the 8 turns of the phase A current lead.

The phase voltage was varied with an ac power supply, which comprised a signal generator and an audio amplifier. The recorded values for output voltage for current passing throughout the Rogowski transducer hoop in both cases are presented in the Table.4.1. The number of the turns in the slot is derived as a ratio of the recorded Rogowski transducer output and it can be expressed as

$$Z = 4\frac{V_{turns}}{V_{lead}} \tag{4.1}$$

where the Z, V_{turns} and V_{lead} is the number of turns in one slot of the armature steel, the Rogovski voltage output for the case the transducer is placed around turns in two armature slots and the Rogowski voltage output for the case the transducer is wrapped around 8 turns of the current lead, respectively. The number of turns in one slot converged to 18.

4.2.2 The winding coefficients of the armature winding

It is from interest to investigate the tendency of the armature winding to attenuate harmonics present in the air gap flux. As illustrated in Fig.4.3a, one phase of the armature winding is distributed over 12 slots (making the number of slots per pole and per phase, q, equal to 6) in the winding with 108 turns in total (6×18). The distribution winding coefficient for the armature winding is defined by (141)

No.	V_{turns} [mV] (Wrap around the turns in two armature slots)	V_{lead} [mV] (Wrap around the 8 turns of the current lead)	Z
1	5.44	1.24	17.55
2	10.56	2.4	17.6
3	15.52	3.52	17.63
4	21.0	4.76	17.64
5	26.8	6.04	17.74

Table 4.1: The recorded results from the Rogowski current transducer in the experiment conducted in order to determine the slot number in the armature winding.

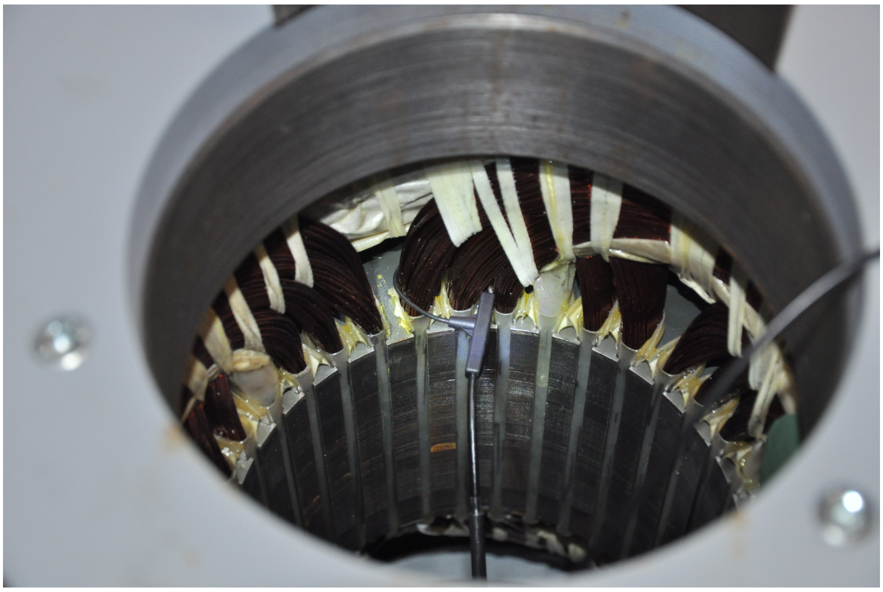

Figure 4.4: Placement of the Rogowski current transducer. - The transducer is wrapped around turns placed in two armature slots.

$$k_{d\nu} = \frac{\left(sin\left(\nu\frac{q\alpha}{2}\right)\right)}{\left(q \cdot sin\left(\nu\frac{\alpha}{2}\right)\right)} \tag{4.2}$$

where the ν is ordinal number of harmonic and α is the angular pitch between two neighboring slots. The pitch winding coefficients for the main and higher harmonics of the armature winding is expressed as

$$k_{p\nu} = sin\left(\nu\frac{\pi}{2}\beta\right) \tag{4.3}$$

where β is the span of the armature sections. The winding coefficients, $k_{w\nu} = k_{d\nu}k_{p\nu}$, for the main and higher harmonics of the armature winding are reported in Table.4.2.

ν	1	3	5	7	9	11	15	17
$k_{w\nu}$	0.9321	0.5079	0.0966	0.0279	0.0	0.0037	0.0056	0.0365

Table 4.2: Armature winding coefficients

4.3 Cryostat

The cooling system and thermal insulation are integral and very important parts of an HTS machine. Several concepts of the cooling system were considered for a cryostat design. The intention of the project was to focus on the electro-magnetic evaluation, analysis and experiments conducted on HTS field winding and HTS machine. Thus, the choice to use the LN_2 temperature range, i.e. from 64 K – 77 K, was made in part to simplify the cooling system requirements but also to challenge the HTS performance. The constructed cryostat is shown in Fig.4.5 in the frame of the HTS machine but without armature cylinder.

4.3.1 The design consideration

The orientation of the cryostat and the three phase winding is vertical (illustrated in Fig.4.1 and Fig.4.5). In addition, a stationary cryostat was chosen in order to simplify mechanical aspects of the design and to allow open bath cooling, ie. LN_2 bath. However, since the difficulty of rotating cooling is expected to be greater than the difficulty of revolving armature, this concept could have merits for wind turbine HTS generator and thus represent valuable experience.

In order to thermally insulate the low temperature chamber from room temperature, the cryostat design needs to inhibit conduction and radiation heat transfer (142, 143). Several materials could be a viable choice for the thermal insulation, like polystyrene foam, powder insulators (107, 144), vacuum, etc. where vacuum has the lowest heat

Figure 4.5: The cryostat. - The cryostat, 1.15m high, is lowered into the armature bore from the top. The bottom torque transfer element and bottom of the cryostat have corresponding pins and slots which are making sure that the cryostat is placed in the axis of rotation.

conduction coefficient (at least one order of magnitude or more depending on the vacuum quality) compared to others.

The radial distance between HTS field winding and an armature winding, i.e. magnetic air gap is an crucial parameter in HTS machine design. The larger the magnetic air gap is, the higher values of MMF are required to produce the same air gap flux density, as seen in Ch.3. Hence, an concept of a machine such as HTS SM with the cold rotor will benefit from the compact thermal insulation placed in the air gap. The vacuum insulation will result in the lowest overall radial thickness of the low temperature insulation enclosure. To investigate the difficulty of vacuum technology and integration into the machine design, we choose to construct a vacuum insulate cryostat.

4.3.2 Choice of material

Low temperature properties (mechanical, thermal, electrical) of materials are often different compared to the room temperature. Thus, the choice of the material for cryostat and outer parts at lower temperature is important.

The composite material and stainless steel were considered as two candidates from which the cryostat could be built from. The thermal and mechanical properties of composite material are largely dependent on the internal structure of the material, like glass (or carbon) fiber density and orientation. Some of the composite materials and its properties can be found in Table.4.3 (107, 145, 146, 147, 148, 149). The data are presented for stainless steel and fibers individually and for composite with 60% of the fiber content. The G.fib. stands for Glass fiber composite and C.fib. stands for Carbon fiber composites. Next letter identifies orientation of the fibers. B stands for Balanced orientation with fibers placed at 0° and 90° while Q stands for Quasi – isotropic orientation with fibers placed at 0°, 45°, -45° and 90°. The number after, specifies the direction of the specified properties of the composite material. The table indicate that with a carefully engineered composite material, it is possible to achieve very good combination of thermal and mechanical properties (strong material while a good thermal insulator).

However, stainless steel was chosen mainly due to better workability (turning, welding...) and the cost of material, even though the thermal conductivity was higher compared to most of the composite materials shown in the table. This choice has particular implication for the TTE design where if composite material was used, even better performance could be achieved.

Material	Thermal expansion $[K^{-1}]$	Thermal conductivity [W/m ·K]	Stiffness (E) [Pa]
SS316L	1,30E-05	7.60E+00	2,00E+10
G.fib.-Q 0°	1,17E-05	6,59E-01	2,46E+10
G.fib.-Q 90°	1,17E-05	6,59E-01	2,46E+10
C.fib.-Q 0°	2,82E-06	2,94E+00	5,36E+10
C.fib.-Q 90°	2,82E-06	2,94E+00	5,36E+10
G.fib.-B 0°	1,17E-05	6,59E-01	3,06E+10
G.fib.-B 90°	1,17E-05	6,59E-01	3,06E+10
C.fib.-B 0°	2,82E-06	2,94E+00	7,44E+10
C.fib.-B 90°	2,82E-06	2,94E+00	7,44E+10
AS4 C.fib -0°	-3,60E-07	8,65E+00	2,28E+11
AS4 C.fib -90°	1,80E-05	5,19E+00	1,66E+10
E-Glass fibers	5,40E-06	1,28E+00	7,24E+10
E-Glass fibers	5,40E-06	1,28E+00	7,24E+10
Epoxy	-4,09E-05	1,88E-01	4,28E+09

Table 4.3: Thermal and mechanical properties of composites and steels at 77 K.

4.3.3 Design details

The design constraints for the outer diameter of the cryostat, the integral thickness of the cryostat in the radial direction, the mechanical clearance between the outer wall and the rotating armature, the inner wall, and the HTS winding are all set to be 158 mm, 9 mm, 1 mm and 0.5 mm, respectively. The overall length of the cryostat is 1,15 m, where no strict constraint has been defined for the axial length of the cryostat.

The resulting magnetic air gap between the rotating armature winding and the stationary field winding is 10 mm including all clearances. For comparative reasons, it is noteworthy to state that the induction machine from which the armature winding was adopted had the air gap of 0.9 mm (based on measurement of rotor radius) which is 1.25% of armature bore radius. This HTS machine will have a magnetic air gap of 12.5% of the armature bore radius.

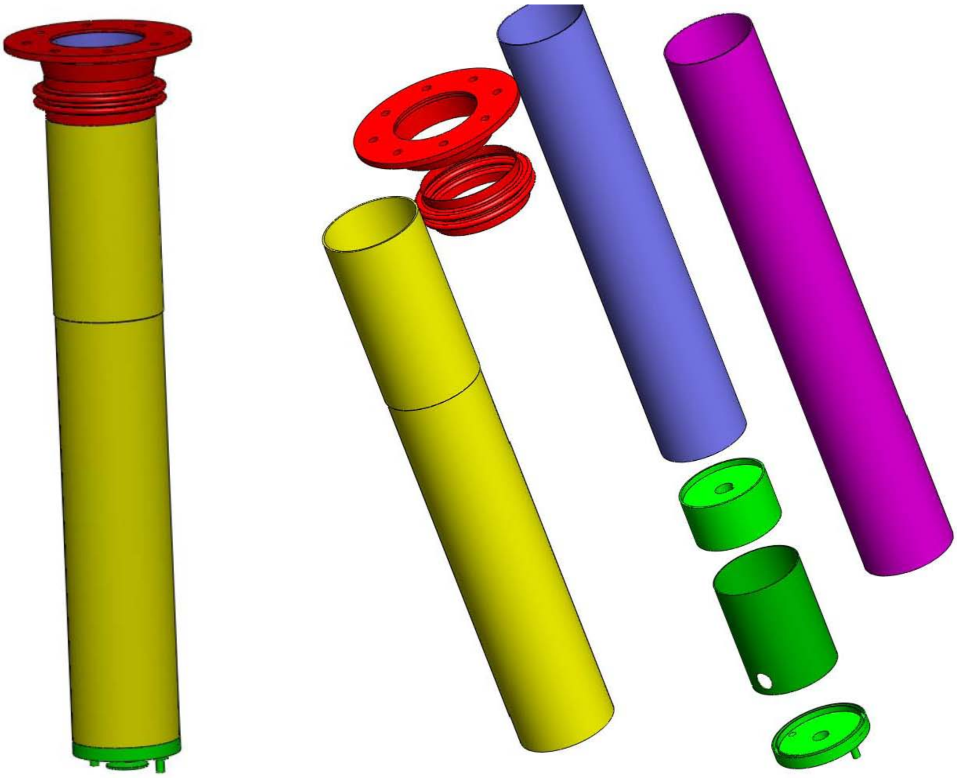

Figure 4.6: The exploded view of the cryostat. - The cryostat is composed from the inner wall (purple) and outer wall cylinder (yellow). The vacuum chamber is in between inner and outer wall. The MLI insulation (magenta) is wound on the inner wall. The torque Transfer Element (green) is located at the bottom of the cryostat. The HTS field winding shaft will lock into the hole on top of the TTE when the HTS field winding is lowered down into LN_2 chamber. The expansion/compression compensator (red) is placed at the warm wall of the cryostat to accommodate thermal expansion/compression of the inner wall of the cryostat due to temperature difference.

4.3.4 Thermal expansion

The thermal contraction of materials have a large implications on the design of a HTS machine. The thermal expansion coefficient for SS is $\sim 0.2\%$. This means that the cold wall of the cryostat will shrink up to 3 mm in the axial direction and 0.3 mm in the radial direction when cooled from 300 K to 77 K.

A corrugated bellow, shown as a part of the cryostat in Fig.4.6 and close up in Fig.4.7 is used to accommodate this difference between the outer and inner walls. Two layers of 0.5 mm SS316L have been shaped as illustrated in Fig.4.7 and welded at the ends. The maximum compression/elongation for the corrugation element is 12 mm while the axial spring constant is 670 N/mm. The stress caused by the cool down of the inner and outer wall was estimated using FE, where the maximum stress found of 6.7 MPa was deemed to be well within the material limits.

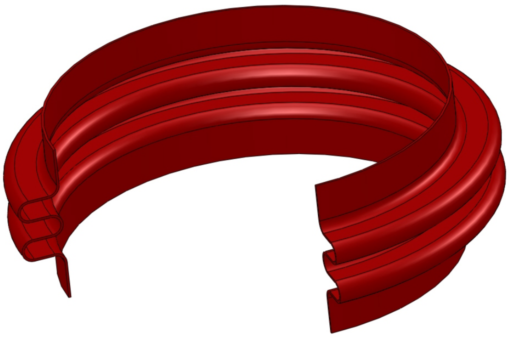

Figure 4.7: The SS corrugation. - The corrugation is placed at the top of the outer wall of the cryostat and it is introduced to compensate the mechanical stress caused by thermal expansion of the material during thermal cycling. A quarter of the corrugation has been cut away to increase visibility.

4.3.5 Torque Transfer Element integrated in the cryostat design

The TTE, fashioned as a SS cylinder with 72 mm for an outer radius and 1.5 mm wall thickness, is illustrated in Fig.4.8. The thermal and mechanical aspects of candidates for a TTE are discussed in more detail in Sec.3.3.2.1.

The following stands as derived in Sec.3.3.2.1: the larger the radius the lower the heat transfer. It was convenient to have a TTE that is naturally continuing onto the inner wall of the cryostat to allow the MLI to be wound without tailoring. This means that the outer radius of the TTE should be the same as the cryostat inner wall, 72 mm (the air gap). With the help of the expression, 3.3, for thickness of the wall of the cylinder derived in the previous chapter, where the value of the 20×10^6 Pa for maximum allowed sheer stress and safety factor n of 3 were used and the design input for the maximum torque set to 250 Nm, the minimal wall thickness for the TTE, $\delta_{wall_{min}}$, is expressed with 4.4. As the thickness of the SS316L cylinder used for the cryostat walls was 1.5mm, the TTE is also made from a cylinder with δ_{wall}= 1.5 mm and $R_{TTE_{out}}$= 72 mm.

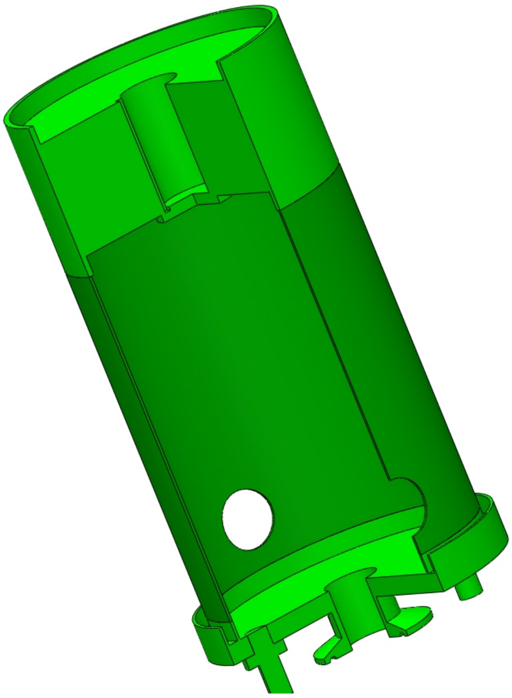

Figure 4.8: The Torque Transfer Element integrated in the cryostat. - The TTE is shown with one quarter cut away to increase visibility. It is welded to the bottom of the LN_2 chamber of the cryostat which accommodates the torque locking shaft socket the HTS field winding is lowered into. The vacuum valve is placed at the bottom of the TTE as an evacuation access point.

Due to orientation, full weight of the cryostat and the field winding will rest on the cryostat walls which will cause some additional stress in the material. The axial load on the TTE comprises the weight of the cryostat, the HTS field winding and LN_2 which in total adds to the 40 kg and the stress caused by the thermal contraction of the inner wall. The total weight would correspond to the stress ~$0.5 \cdot 10^6$ Pa for the δ_{wall}= 1.5 mm. This stress is well within the limits of the material (where $\geq 200 \times 10^6$ Pa is usually observed for SS316L stainless steel at 0.2% strain).

$$nT_{max} = \frac{\pi}{2}(R^4_{TTE_{out}} - (R_{TTE_{out}} - \delta_{wall})^4)\frac{\tau_{max}}{R_{TTE_{out}}} \longrightarrow \delta_{wall_{min}} > 1.18mm \qquad (4.4)$$

The corrugation will distribute the weight of the structure mostly on the outer wall. The spring constant of the corrugation is ~ 670 N/mm in the axial direction and the compression of the inner wall of the cryostat is ~3 mm in axial direction which results in the 2010 N force pulling upwards the inner wall and pushing downwards at the outer wall. The total stress caused by the thermal stress and the weight of the structure in the outer wall of the cryostat is found to be 3.4×10^6 Pa. This discussion proved that the thermal stress and rated electromagnetic torque are not compromising mechanical integrity of the cryostat.

4.3.6 Vacuum

The cryostat vacuum chamber consists of the volume of the space between the inner and outer cryostat walls and the volume inside of the TTE (the chamber inside the TTE is connected to the space between the walls with two holes visible in Fig.4.8). The vacuum chamber was evacuated and the vacuum valve was closed off when the pressure inside of the vacuum chamber was at 10^{-5} mbar (10^{-3} Pa). First pumping took approximately one week and with the cool down, pressure went below 10^{-6} mbar (10^{-3} Pa) due to the cryopumping effect (144, 150, 151).

The out gassing in the vacuum chamber caused by residual impurities on the walls of the cryostat and the MLI insulation was substantial after the first pumping. The pressure increased after the thermal cycle (pumping → cool down → room temperature) to 10^{-2} mbar (10^{-1} Pa).

This issue was planned to be tackled by 'baking' the cryostat were the heaters are introduced around the cryostat and the temperature is raised up to 80°C – 90°C (caution must be exercised with maximum temperature due to MLI limitation) while the vacuum chamber is being evacuated. All humidity and impurities contained in the vacuum chamber would evaporate much faster, leading to higher, longer lasting and faster achievable vacuum. After third pumping the vacuum stayed below 10^{-4} mbar after several thermal cycles and backing was not necessary. However, if the longevity of the vacuum is important, the 'baking' combined with introduction of the 'getter' compounds in to the vacuum chamber of the cryostat is highly recommended (152).

4.3.7 Manufacturing and assembling consideration

Assembling procedure is shown in Fig.4.9. The MLI insulation was wound around the inner wall after the inner wall and TTE were welded to the bottom of the LN_2 chamber. The space in the radial direction of the cryostat is limited due to the magnetic air gap and thus tight tolerances for the concentric accuracy of the walls of the cryostat had to be set. To achieve high concentric accuracy and roundness over the length of the cryostat was a challenge.

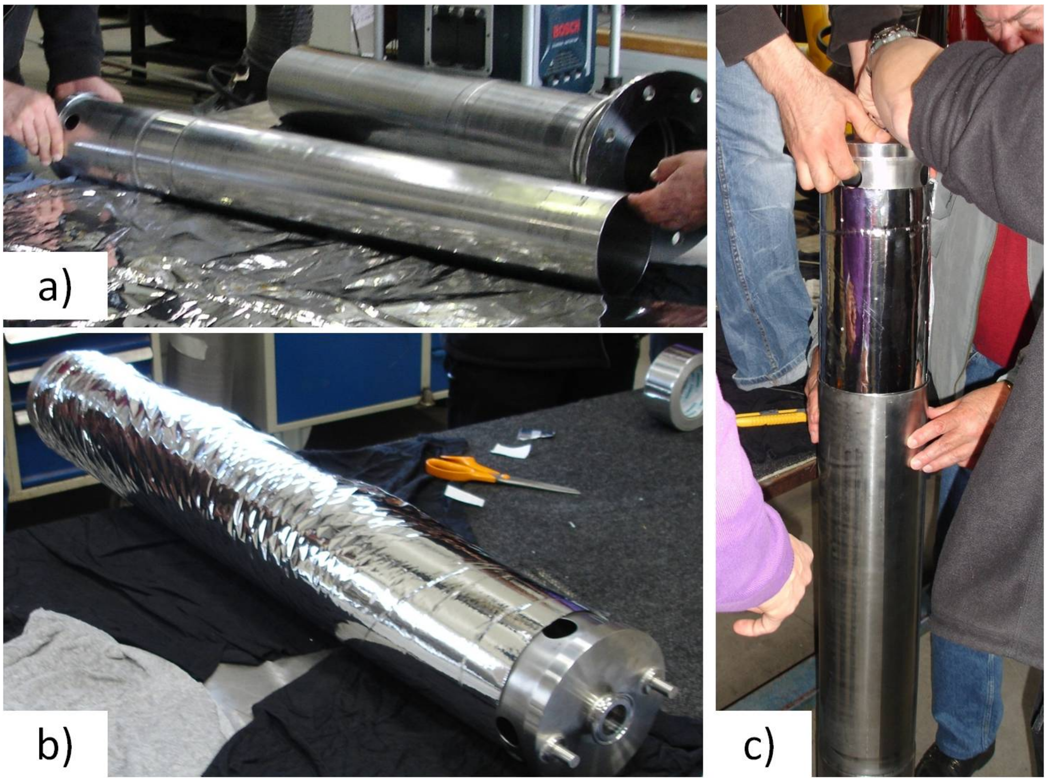

Figure 4.9: The cryostat during assembly phase. - The cryostat was fashioned from two parts, inner and outer wall, welded together at the bottom and the top. (a) The preparation step for applying the MLI insulation on inner wall of the cryostat. Both walls are shown in the photo. (b) The MLI is wound on the inner wall of the cryostat and tied with low emissivity aluminum adhesive tape. (c) Assembling stage for the cryostat. Insertion of the inner wall with MLI insulation into the outer wall of the cryostat.

The sub millimeter tolerances can be achieved by turning the element in a lathe. That usually calls for minimal wall thickness of the cylinder to be $\geq$3 mm, which in this case made turning unfeasible. The highest tolerance achievable with a press rolled sheet of the SS316L stainless steel (SS) to desired radii was found to be 0.5 mm. Thus, two SS316L stainless steel (SS) sheets of 1.5 mm thickness have been pressed rolled and welded into two cylinders with an outer diameter of 158 mm and 143 mm respectively.

The mechanical clearance between the inner and outer wall of the cryostat for both the HTS field winding and the armature winding were set to 1 mm and 0.5 mm, respectively. The radial tolerances were set in such a way that the mechanical clearances defined are the absolute minimum distance allowed between the two parts. This means that the dimension for the outer wall of the cryostat had specified dimensions of 157.5 mm ±0.5 mm to maintain mechanical clearance of at least 1 mm between the armature teeth and the cryostat. As a consequence the vacuum chamber may not be perfectly cylindrical and will not have constant distance between the inner and outer walls (maximum variations of 1 mm).

4.3.8 Heat transfer consideration

To evaluate the integral heat transfered to the LN_2 chamber of the cryostat, it is useful to simplify the geometry of the cryostat. Three sections of the the cryostat were identified and illustrated in Fig.4.10, each of which with different boundary conditions.

The radiation and conduction through residual gas will be dominant in the middle section. The middle section of the inner wall of the cryostat, $750mm$ high, left in Fig.4.10, will be at $77K$ while for the outer wall it can be assumed that it is at room temperature. The top and bottom sections will have temperature gradient from $77K$ to $300K$.

However, to estimate the heat transferred via conduction through the residual gas in the vacuum chamber and radiation, it is better to assume that the inner wall of the cryostat is on $77K$ across the whole length of the cryostat, $1065mm$ (calculated in Fig.4.10). This will cause somewhat higher values for the heat transferred.

4.3.8.1 Conduction heat transfer

The contributions of the heat transfer through the solid for the top and the bottom section of the cryostat and conduction through gas over the middle section of the cryostat will be taken into account in this section.

Conduction in the gas: As the space between the outer and inner wall is much smaller than the length of the cryostat, the problem can be observed as two parallel planes 1065 mm. The walls (planes) are spaced apart 6 mm, but since MLI insulation is wound on the inner wall the space have been reduced to ∼2 mm (details are presented in Appendix.??). The mean free path for air at 77 K and 0.133 Pa ($1.33 \cdot 10^{-3}$ mbar) is ≈9 mm which is a good reference for the minimum value of the pressure that needs to

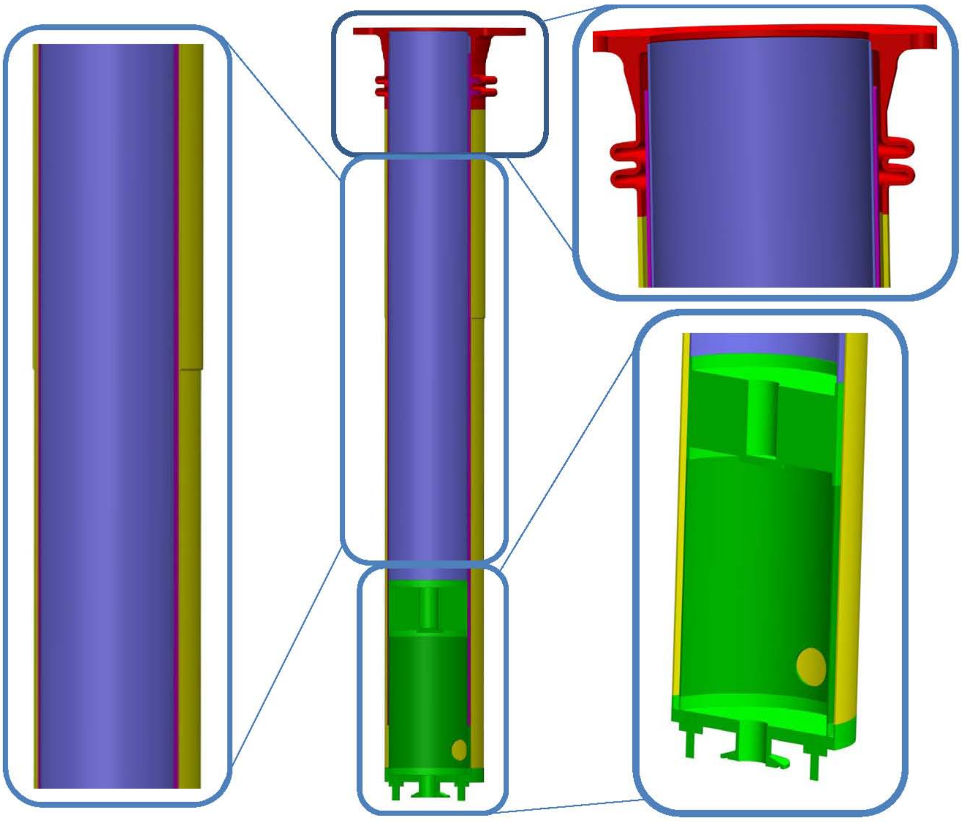

Figure 4.10: Sections of interest for the heat transfer analysis of the cryostat. - The cross section of the 3D CAD model of the cryostat with three sections emphasized. The top of the inner part, not directly exposed to the LN_2, is approximately 120mm. The section exposed to the LN_2, the middle section, is approximately 750mm and bottom section which is actually the TTE is 200 mm long. (The surface between the inner and outer wall of the cryostat including the whole height of the cryostat: $A_{cryo} = 2 \cdot \pi \cdot R \cdot L = 2 \cdot \pi \cdot$ 0.075[m]·1.065[m]=0.501m^2)

be ensured in the vacuum chamber in order to suppress the heat conduction through gas. The heat transfered per surface area for two parallel plates (107) can be expressed as 4.5

$$\dot{Q}_{gas-conduction} = \hat{\alpha}\frac{(\gamma+1)}{(\gamma-1)}\sqrt{\frac{R}{8\pi MT}}P(T_2 - T_1) \tag{4.5}$$

where α is the mean accommodation coefficient of the gas molecules at two planes, γ is the ratio of specific heats at constant pressure and constant volume C_p/C_v, R is universal gas constant, M is the molecular weight of the gas molecules, P is the gas pressure and T_2 and T_1 the temperatures of the planes with higher and lower temperature, respectively. The above equation can be reduced to

$$\dot{Q}_{gas-conduction} = const \cdot \hat{\alpha} \cdot P \cdot (T_2 - T_1) \tag{4.6}$$

where the *const* will be ≈ 2 and $\hat{\alpha}$ will be ≈ 0.9 for the air at $T = T_1$=77 K. The pressure is in units of Pa, temperature in K and specific heat transfer is in Wm^{-2}. The heat transfered through residual gas is a linear function of the pressure between two planes expressed with

$$\dot{Q}_{gas-conduction}[W/m^2] \approx 402 \cdot P[Pa] \tag{4.7}$$

An estimate of 1.90 W heat transfered via gas conduction was calculated taking the value 10^{-4} mbar (10^{-2}Pa) for the gas pressure and A_{cryo}=0.501m^2 for the active gas heat exchange surface. The pressure of the residual gas in the vacuum chamber is indeed a crucial parameter. The value of 10^{-5} mbar and lower would make this heat transfer negligible. Is is noteworthy to say that maintaining a high vacuum is not trivial and proper measures have to be taken to ensure vacuum quality over a long time (getter compounds, regeneration of vacuum by pumping).

The heat conduction through the solid: The heat transfered through the inner wall from the top and bottom section is determined by the thermal conductivity of the material, $K(T)$, and is given by

$$Q_{conduction} = \frac{A}{L} \int_{T_1}^{T_2} K dT \tag{4.8}$$

where A is the cross section area normal to the heat transfer propagation and L is the distance from the high temperature end (T_2=300 K) to the low temperature end (T_1=77 K). The inner cryostat wall is a cylinder with radius of 72 mm and a wall thickness of 1.5 mm. The cross section area of the wall is $A = \pi(R^2 - (R - \delta)^2)$=671.5 mm^2.

The resulting conduction heat transfer of the cryostat including the cross section area and lengths for bottom and top of the cryostat together with integral thermal conductivity for the temperature range from 300 K to 77 K (64 K) are presented in Table.4.4.

Section	A [m^2]	L [m]	$\int K(T)dT$[W/m] (107)	Q_{cond}[W]
Via Gas @10^{-4}mbar	0.4818	-	2720 @77K (2850 @64K)	1.90 (1.95)
Top	6.7 10-4	0.115		15.90 (16.60)
TTE	6.7 10-4	0.195		9.35 (9.80)
Shaft	2.8 10-3	0.115		66.90 (70.00)

Table 4.4: Heat transferred by conduction through the residual gas and different sections of the cryostat for 77 K (64 K).

Thus, the estimated heat transfer through the TTE is ~10 W which is comparable to the design from (105, 118) where TTE was made from composite material (G10) and 60W of heat in total was estimated for 77 K. The table includes the heat transfer estimate for the top shaft. This is included because the cryostat is operated as open LN_2 bath and the HTS field winding had the shaft as a top TTE. This is not optimal and in the future with closing the cryostat, the top TTE will be similar to the existing one at the bottom of the cryostat.

4.3.8.2 Radiation heat transfer

Radiation heat transfer can be a big part of the integral heat transfer in low temperature equipment design. To estimate the heat transfered by radiation, two cylinder walls of the cryostat are assumed to be parallel plates where the heat transfer is given(107) by:

$$Q_{radiation}[W/m^2] = \sigma F_A F_B A_1 (T_1^4 - T_2^4) \tag{4.9}$$

where σ=5.67×10^{-8} Wm^{-2}K^{-4} is the Stefan-Boltzman's constant, A_1 is the surface area of the outer wall, T_1 and T_2 are temperatures of the outer and inner wall, respectively. The emissivity related coefficients for two planes, F_A and F_B are defined as

$$\begin{aligned} F_A &= 1 \\ F_B &= (1/e_1 + 1/e_2 - 1) \end{aligned} \tag{4.10}$$

Values for the emissivity of the stainless steel e is in the range of 0.02-0.1 (107) depending on the surface finish. If the value of 0.03 is taken for both walls, one gets

$$Q_{radiation}[W] = 5.67 \cdot 10^{-8}[\frac{W}{m^2K^4}] \cdot 1 \cdot 0.01526 \cdot (300^4[K] - T_2^4) \tag{4.11}$$

The heat transfered by the radiation for the plates with the total surface of A_{cryo}=0.501 m^2 (along the whole length of the cryostat) and for the 77 K was found to be 3.48 W. This value was over estimated because effective radiation surface was somewhat smaller. Nevertheless, the 3.5 W heat is not small (especially if the cryostat is to operate at lower temperatures, i.e. $\leq$64 K) and thus the MLI was employed to reduce this value. Ten layers of Multi Layer Insulation (MLI) CoolCut 2NW foil (153) was wrapped three times around the outer side of the inner cryostat wall and tied with stainless steel wire and low emissivity aluminum adhesive tape (see Fig.4.9). Each aluminum layer is 12 μm thick and is coated on 0.13 mm polyester substrate (153).

In the ideal case, n layers of MLI should allow only 1/(n+1) part of the radiation (152). For 30 layers of the MLI, which was reported as an optimum number of layers (107), the radiation has been reduced by a factor of 31 resulting in 0.112 W for the total heat transported via radiation. This number would not change much if the cryostat is operated at lower temperatures (double value for 20 K operation).

4.3.9 The evaporation test

The integral heat transfer is the sum of the conduction and radiation heat transfered from 300 K to the low temperature chamber. The dominant influence on the sum is the conduction through the TTE and the top section of the cryostat. The sum of the heat without the shaft contribution is 27.27 W according to the Table.4.4. It is possible to evaluate the heat transfer that the low temperature chamber will experience experimentally by monitoring the evaporation rate of LN_2. The evaporation test was performed, and results are shown in Fig.4.11 for the case where the cryostat is without the HTS field winding.

In this standalone test, the conduction heat through the shaft is not included. The main contributors to the integral heat transfer rate are the TTE, conduction in the residual gas and the radiation. The heat conduction at the top of the cryostat is also not significant here because as the LN_2 evaporates, the cold N_2 gas will per-cool the top section of the inner wall of the cryostat. Two 'boil-off' tests have been performed, one after first pumping and another after several cooling cycles. The heat transfer

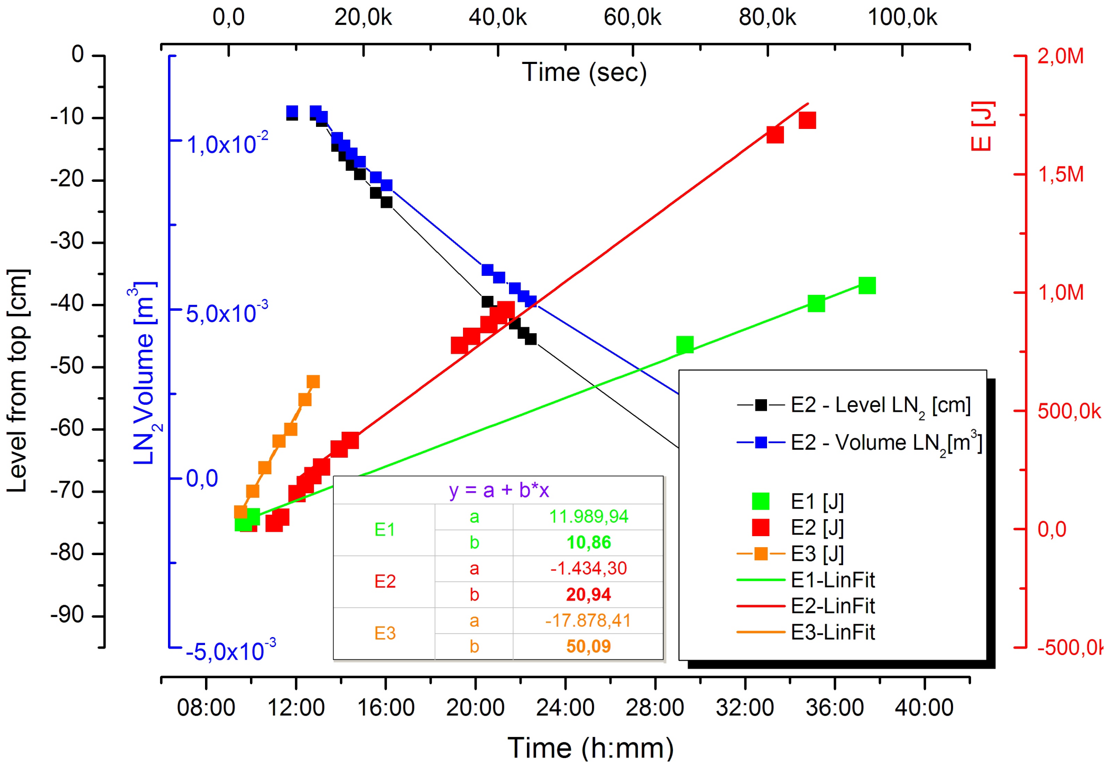

Figure 4.11: The LN_2 'boil-off' data for the cryostat. - The data for evaporated LN_2 are presented for three cases: (a) The cryostat alone after evacuation of the vacuum chamber. (b) The cryostat after few thermal cycles. (c) The cryostat and the HTS field winding including all current leads. Linear fit was performed where the slope represents the average rate of heat transfer in Watts.

rate derived from the first test was in average 10 W where the pressure in the vacuum chamber was below $5{\cdot}10^{-6}$ mbar throughout the whole test. This is in agreement with the results for the conduction and radiation heat transfer, reported in the Table.4.4. In the second test, the vacuum pressure was not measured during the test and the average integral heat transfer rate was determined to be 21 W. The higher heat load is probably due to the higher pressure in the vacuum chamber which was caused by out-gassing. The rate of evaporation was monitored when the HTS field winding was under test too. Here, the added contribution from the shaft and current leads (8 cables in total, each with 10 mm^2 cross section) are of the same order of magnitude as the heat load of the cryostat. The derived integral average heat transfer rate was found to be 50 W. It is important to mention that during the experiments, the level of the LN_2

was maintained in the range of 10 cm to 30 cm from the top of the cryostat.

4.4 The field winding

The field winding is comprised of a number of HTS coils, maximum 8, supported by the housing for the coils. The field winding steel is optional and can be omitted if the test calls for it. If the cold steel is part of the HTS field winding, the coils are stacked on the steel and the whole structure is supported by the coils housing.

4.4.1 HTS coil

HTS conductors are commercially available in the form of tapes 4 mm – 12 mm wide and 0.1 mm – 0.3 mm thick. Both BSCCO and YBCO are ceramics, brittle by nature. Because of it, 1G and 2G tapes have certain mechanical constraints like minimal bending radius and maximum yield stress. In addition, tapes have also limited twisting ability around the longitudinal axis. As a result only simple, racetrack, coil geometry have been wound with an HTS tape. Constructed coils are listed in Table.4.5 and the illustration of the proposed coil design is shown in Fig.4.12.

All coils have access to the voltage measurement across the whole coil as well as several sections (one or more) in the middle of the winding. All voltage measurement points are accessible on the printed board mounted on the outer frame. Thus, the difference in the performance of the outer and the inner section of the HTS coil can be evaluated, as all turns are not exposed to the same magnetic field and will thus have different critical currents.

4.4.1.1 The HTS coil frame

All coils have the same design. In this way space allocated for the turns in the coil is the same for all coils. Thus, the coil performance can be evaluated. This is very important for an electrical machine design because the critical engineering current density of the coil, $J^e_{c_{coil}}$ is not only a function of the performance of an HTS tape used in the coil but also depends on the insulation material employed, the coil former (structural support) design, cooling requirements of the design (additional channels or conducting cooling bars), etc. So, it is not just an HTS conductor but the HTS coil design and production

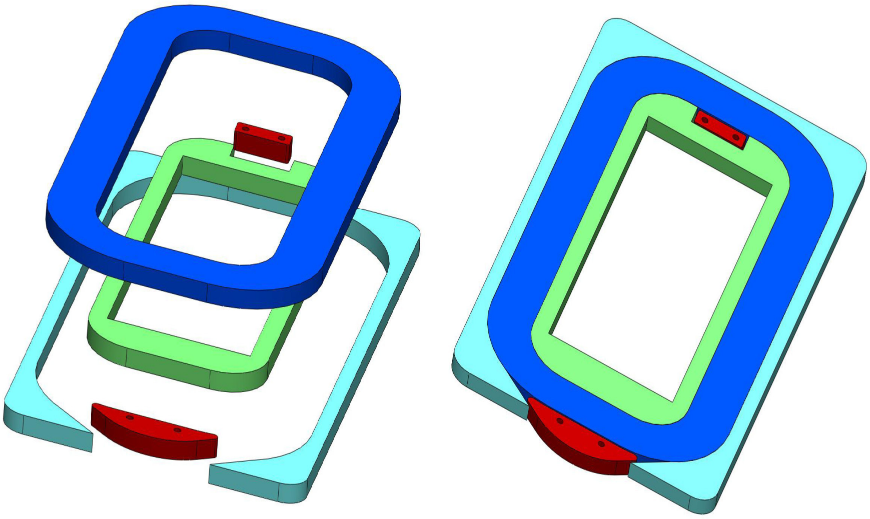

Figure 4.12: The 3D CAD illustration of the Superwind HTS coil design. - The HTS coil is shown in the exploded view at the left, making all parts identifiable. The inner and outer frames, green and light blue, respectively, are made from SS316L. The coil terminals, made from copper are colored red. The ends of the coils are positioned at both the outer and inner frame. The winding process was as follows: The inner frame was mounted on the winding machine. The insulated HTS tape was wound on to the inner frame. All access points for the measurement of the voltage and coils terminals have been soldered at appropriate place during the winding process. The outer frame was added to the wound coil, measurement wires are lead to the circuit board mounted on the outer frame (not shown in the figure) and coil is vacuum impregnated with the epoxy(5).

approach together with the performance of HTS conductor that are being assessed in this way.

The coil *Coil*#4 (not used in experiments) is shown in Fig.4.13. Frame is made form SS316L and both inner and outer frames have a series of holes that are used as a mechanical interface between the coils during the field winding assembling. The design of the coil frame was primarily intended for double pancake coils, where two racetrack coils have been coupled together into one. In that arrangement, the double pancake coil would have both of its accesses to the coil terminals at the outer frame, allowing for a denser packed field winding. However, the coils were operated with individual

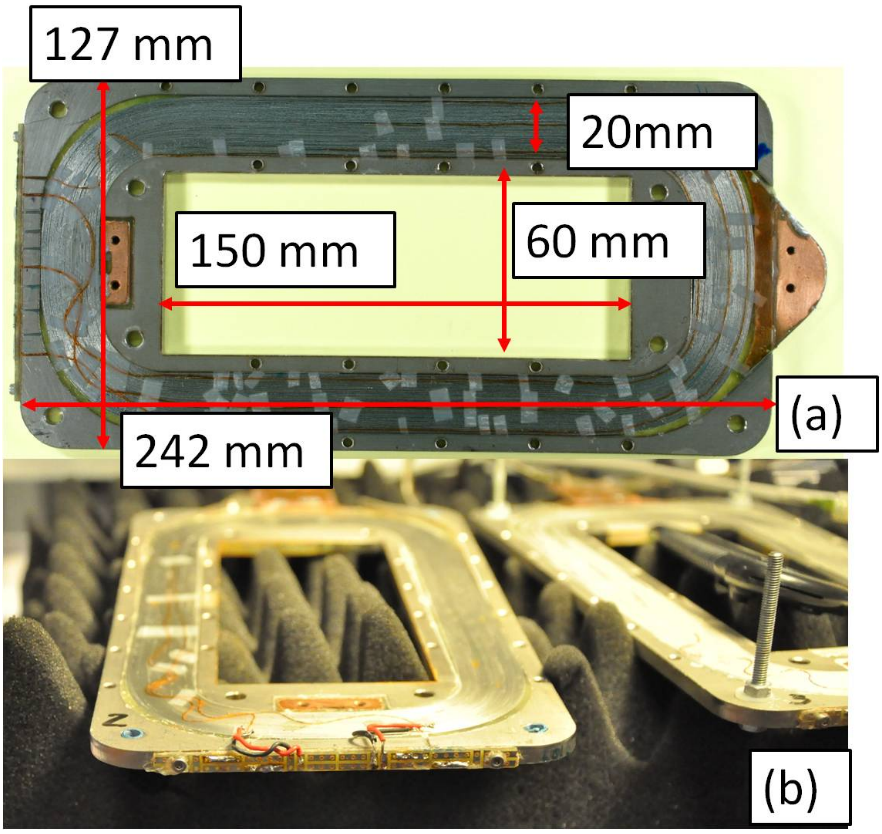

Figure 4.13: The HTS coil - (a) *Coil#4*; (b) *Coil#2*.

supplies and current leads which resulted in a less compact but more flexible setup.

4.4.1.2 Electric insulation for HTS coil

The number of materials that can be used as a electrical insulators at low temperature is limited. Next to having appropriate electrical strength, the insulation material must be able to cope with thermal and also mechanical stresses that the HTS tape will be exposed to during machine operation. The few materials that could be an option include composite (glass fiber tape), Mylar tape, Kapton tape, etc. The insulation level for each coil is determined by transients of the field current and self inductance of the coil. As these are small coils, a voltage insulation level of 100 V would suffice.

As implied in the previous section, electrical insulation has a major implication in the coil performance. The most obvious impact on a coil performance is the critical engineering current density $J^e_{c_{coil}}$ of the coil. If the electrical insulation of the coil needs to be thick, where the thickness primarily depends from the electrical strength of the material, the $J^{e}_{c_{coil}}$ of the coil will decrease.

Coil ID	L_{coil} [cm]	No. of Turns	HTS Type	I_c^{sf} , 77 K [A]	Insulation	Voltage access points	Add-In probes
Coil2	2540	48	AMS-1G	120	Glass Fiber	3	Hall sensor
Coil3	2880	51	AMS-1G	120	Glass Fiber	3	Hall sensor
Coil5	2500	46	AMS-1G	120	Glass Fiber	6	Hall sensor, RTD
Coil6	3165	56	AMS348C-2G	120	Glass Fiber	6	Hall sensor
Coil7	7000	125	SP4050-2G	120	Epoxy	3	-
Coil8	7000	125	SP4050-2G	120	Epoxy	3	-

Table 4.5: The HTS coils constructed for the testing. AMS-1G (1) is BSCCO wire from American Superconductor, AMS348C-2G (1) is YBCO coated conductor 348 from American Superconductor and SP4050-2G (2) is YBCO coated conductor from Super Power Inc.

Depending on the type of the HTS tape and insulation employed, the number of turns for different coils can vary. Details about completed HTS coils are presented in Table.4.5.

4.4.2 The HTS field winding

The space allocated for the HTS coils can accommodate a maximum of 8 single HTS coils, each 5 mm thick or 5 double pancake coils (10 single coils) all stacked together. In the HTS field winding, illustrated in Fig.4.14, all coils are placed between 4 aluminum bars which are screwed into the top and bottom flange. The aluminum bars are acting as a housing for the HTS coils with the steel providing all the mechanical support. The position of the coils can be adjusted with spacers placed in between the coils. The coil stack is fixed together with four treads and 8 nuts placed in each corner of the coil. To utilize the versatility of the HTS field winding coils have separate leads, two for each coil.

The current leads are lead to screw terminals where the coils connections can be altered without interfering with the coil arrangement itself. Maximum flexibility is

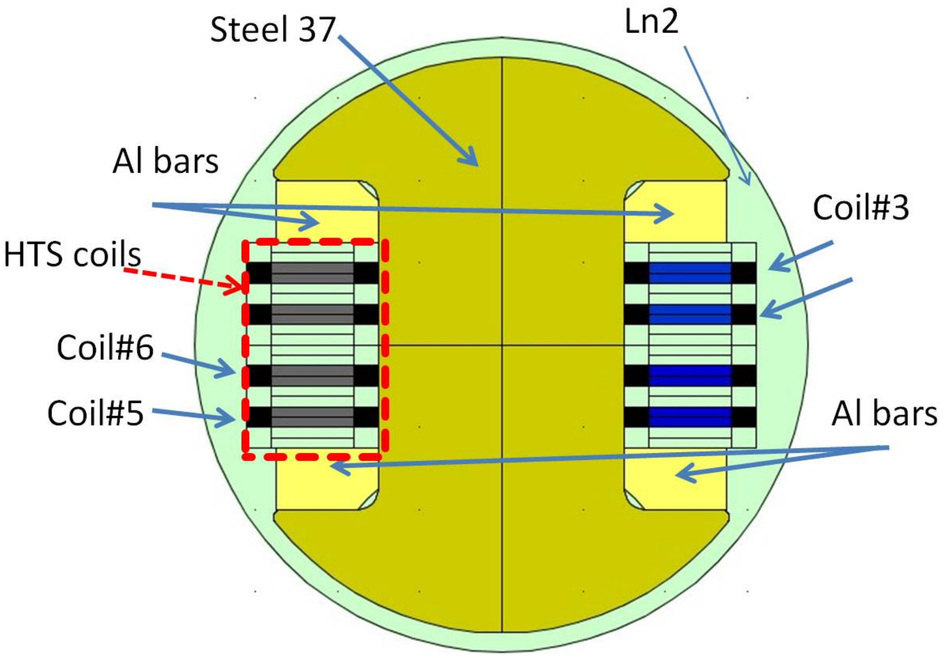

Figure 4.14: HTS field winding - 2D cross section of the HTS field winding with the HTS coils. The arrangement of the coils is the same as in the conducted tests. The space allocated for the HTS coils can accommodate maximum 8 coils (single racetrack coil), each 5 mm thick. The coils are placed between four aluminum bars (yellow) acting as a mechanical support structure. Steel 37, the field winding steel (light green) is fixed by screwing the pole shoe into the steel body and thus exerting the pressure on the aluminum bars.

achieved if each of the current leads are brought outside of the cryostat. Consequently, the increase in the heat input to the LN_2 chamber should be expected as reported in Sec.4.3.8.

4.4.3 Cold steel

The HTS field winding can stand alone (without steel) or the HTS coils could be wrapped around the cold steel. This corresponds to the two types of the HTS machine, so-called air-core machine and the HTS machine more similar to the conventional synchronous machine where the steel is a part of the field winding, as discussed in Ch.3.

The soft carbon steel, named Steel37, has been employed as the field winding steel. The Steel37 was machined from a single piece of steel into three parts, two pole caps and

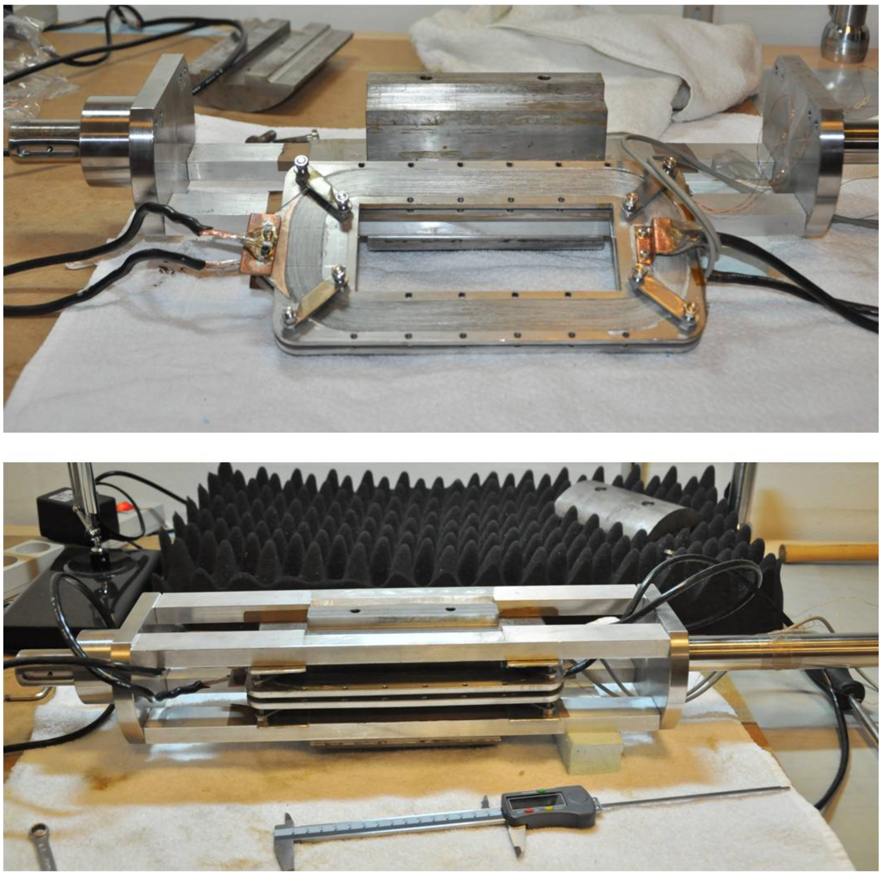

Figure 4.15: HTS field winding - The HTS field winding is shown in assembly phase with two HTS coils mounted on the cold steel.

the middle. The pole caps are screwed into the middle piece (see Fig.4.16). The choice of the steel was made with following consideration. The material should be low cost and the steel should be a monolithic piece and not laminations. In addition, even though in this setup the magnetic air gap is large compared to the conventional machines, the HTS machine flux is in general air dominated (either because of the absence of the steel or because the steel is saturated). Thus, it was of interest to employ the steel with relatively low saturation (see Fig.4.17) in order to examine the implication of the saturation with regard to HTS machine operation (an HTS will experience more leakage flux).

Air gap flux density distribution The pole caps are circular (no pole shaping) with the pole angle τ_{pole}=103.7°. The harmonic content of the air gap distribution can

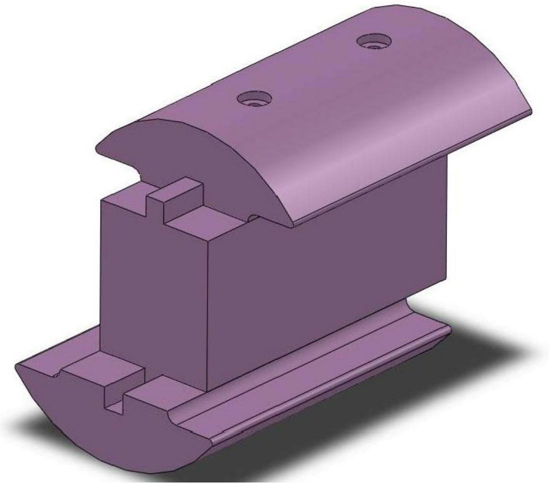

Figure 4.16: The 3D CAD model of the field winding steel - The cold steel where the pole caps are skewed in the middle part.

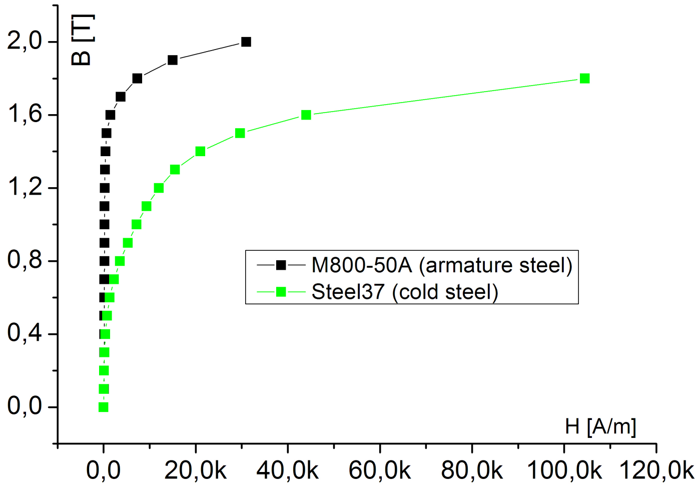

Figure 4.17: The field winding steel - The comparative diagram of permeabilities of armature steel, M800, and the field winding steel, Steel37.

be estimated by assessing the harmonic of the simplified air gap flux density angular distribution. The distribution of the flux density of one pole ($-\pi/2 \leq \theta < \pi/2$) can be represented as a constant value B_m for the angles $-\tau_{pole}/2 \leq \theta \leq \tau_{pole}/2$ and zero for other angels.

$$B_g(\theta) = \begin{matrix} B_m, -\tau_{pole}/2 \leq \theta < \tau_{pole}/2 \\ 0, -\tau_{pole}/2 \geq \theta > \tau_{pole}/2 \end{matrix} \tag{4.12}$$

where the ν is harmonic ordinal. The amplitude of the each harmonic present in the field winding produced air gap flux is expressed with

$$B_{\nu g} = \frac{2}{\pi}\int_{-\tau_{pole}/2}^{\tau_{pole}/2} B_m cos(\nu\theta)d\theta = \frac{4B_m}{\nu\pi} sin(\frac{\nu\tau_{pole}}{2}) \tag{4.13}$$

A considerable amount of harmonics is expected in the air gap flux density with the 5^{th} leading with 25%. The content of the harmonics is illustrated in Fig.4.18 where harmonic content is derived with approximation presented above (with expression 4.13) is compared to the results derived from FE model.

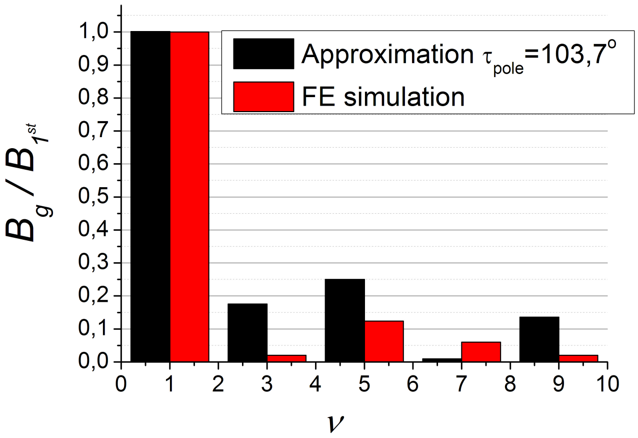

Figure 4.18: The HTS field winding steel harmonic content - The harmonic content for the pole with constant radius of R_{pole}=70 mm and $\tau_{pole} = 103.7°$

In this setup the 5^{th} and the 7^{th} harmonics were deliberately kept in the machine design with intention to allow the analysis of its impact on the HTS coils as they are most common in the conventional machines and are not filtrated in the three phase system (machines or transformers connected into delta). The simplified approach to estimate the harmonic content of the pole cap was verified by means of FE model. A Fourier transform was performed on the air gap flux density derived from FE simulation of one particular case presented in Fig.4.19 where the harmonic content is compared to estimate in Fig.4.18.

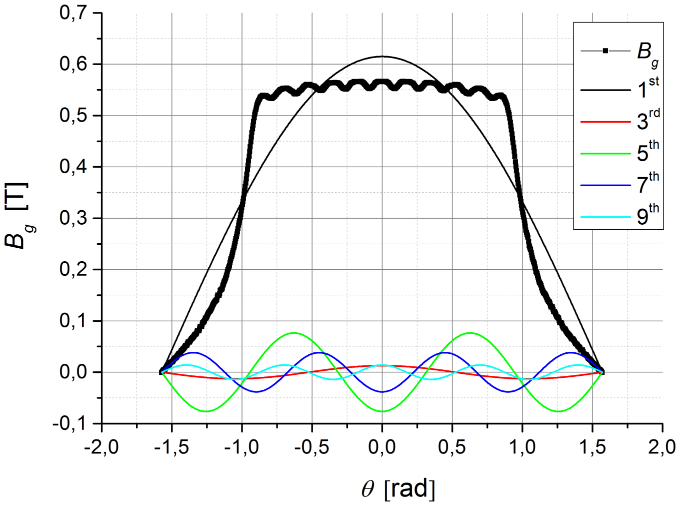

Figure 4.19: Air gap flux density harmonic content - Harmonic content of the air gap flux density derived from the FE model where the field winding had MMF∼12k Ampere-Turns. The figure includes the first five odd harmonics.

Additionally, the harmonic content of the induced voltage could be suppressed in various ways like pole shaping, choice of appropriate armature winding factor.

4.4.4 The field winding housing

The HTS field winding is fixed in between 4 aluminum bars which are screwed into the top and bottom shaft. In that way the coils and steel could be mounted independently and a number of field winding arrangements can be investigated (from absence of the field winding steel, experiments with different types of steels used as a cold steel, shapes of pole caps, etc.). Bars are screwed into the top and bottom shaft (see Fig.4.20) with 4 screws per bar. The aluminum bars are acting as a housing for the HTS coils and the steel providing mechanical support. A slot exists in each aluminum bar (see Fig.4.20b) that is adopted to the shape of the cold steel, fixing it to a specific position. The maximum stress of $3.2{\cdot}10^6$ Pa have been found in the coil support structure for the rated electromagnetic torque of 250 Nm, which is well in the material capabilities (where $20{\times}10^6$ Pa is maximum allowed stress for aluminum).

The HTS housing bars are placed at the far outer radius and not concentric as the shaft would be. The reasoning for this is found in the magnetic design of the HTS field

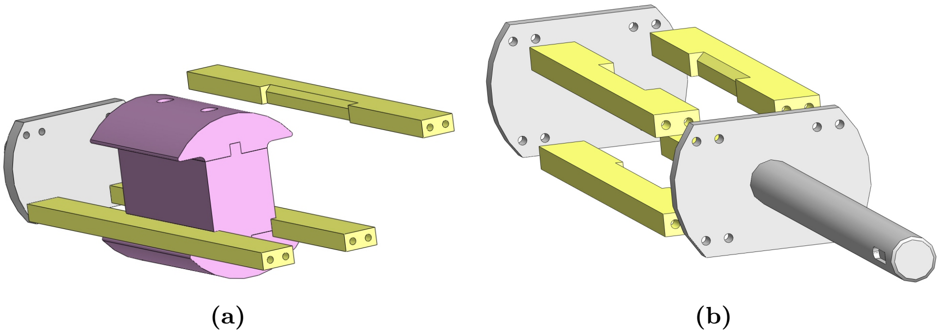
(a) (b)

Figure 4.20: The field winding support -

winding. The racetrack coils are planar coils and if the bars are placed at the middle, similar to how the shaft would have to be, no coils could be placed at the middle of the poles where the best performance of the HTS coils would be expected due to the low amount of stray flux. Secondly, if instead the bars were in the middle and the coils were at the outer, the volume allocated for coils would be smaller.

4.5 Torque Measurement

Several brands of torque meters are commercial available (Himmelstein, HBM, Scaime and others). But, with the setup positioned vertically and the absence of the shaft, the commercial torque meters would need to be adopted and their measurement performance could not be guaranteed. Additionally, the cost of the commercial torque meters is substantial.

Instead, the setup is equipped with a custom built torque measurement option, illustrated in the Fig.4.21. Two SS316L plates are placed at the bottom of the cryostat. One plate (bottom plate) is fixed to the frame of the setup (not able to move). The other plate (top plate) has an imprint of the TTE at the bottom of the cryostat, so when lowered down on to that plate, the cryostat and the plate will be locked with respect to the torsion. A spacing between the two planes is maintained with a SS316L ring. The ring fits into concentric slots machined in the top and bottom plates. In this way, the top plate is not able to move in any other direction except to rotate around its axial axis. The vacuum valve for the vacuum chamber of the cryostat is placed at the bottom of the TTE, hence both plates have openings in the center.

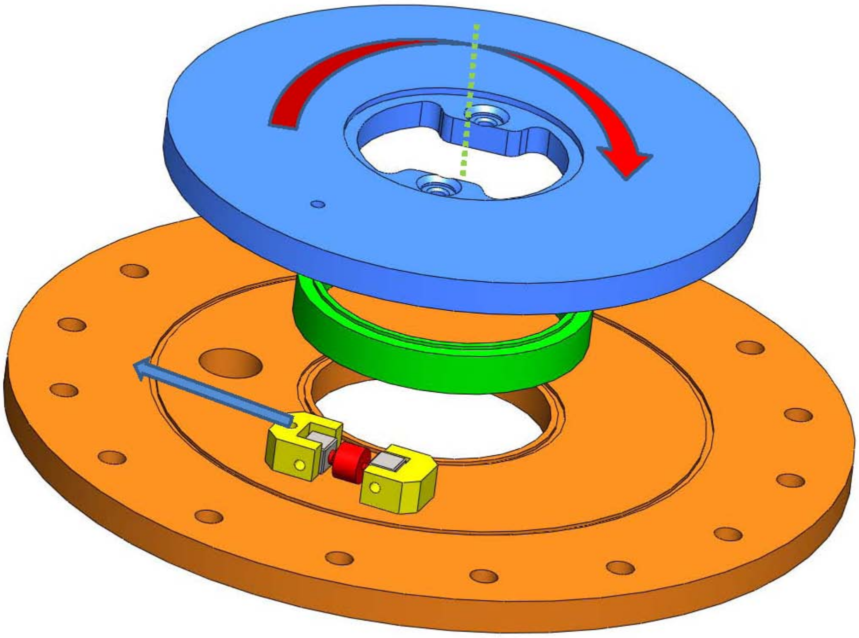

Figure 4.21: Superwind torque measurement assembly - The 3D CAD model of a torque measurement assembly consisting of two plates and a force transducer in between. The bottom plate (orange) is fixed to the frame while the top plate (blue) is fixed to the cryostat's TTE. The ring (green) has the purpose of simple bearing. It allows the rotation around the cryostat's axial axis. The force transducer element (red) is fixed to the bottom plate at one side and to the top plate on the other side (yellow). The torque (red arrow) experienced by the top plate is translated into an elongation force of a force transducer (blue arrow) and finally into a voltage signal from a strain gauge which is proportional to the torque.

The electromagnetic torque is transferred from the HTS coils and cold steel through the field winding housing and TTE to the top plate of the torque measurement assembly. If the load cell (force transducer) is placed in between the two plates, bottom being fixed to the frame and top to the TTE of the cryostat, the output voltage from the load cell will be proportional to the torque. By adjusting the distance from the axial center of rotation to the load cell, the torque measurement range and sensitivity can be tuned which makes this assembly very flexible.

The HBM-UB9 500 N bidirectional force transducer (154) is used as a load cell. The UB9 transducer, illustrated in Fig.4.22a, has an integrated full bridge strain gauge with a linear voltage output. The load cells are general very sensitive to the load in the

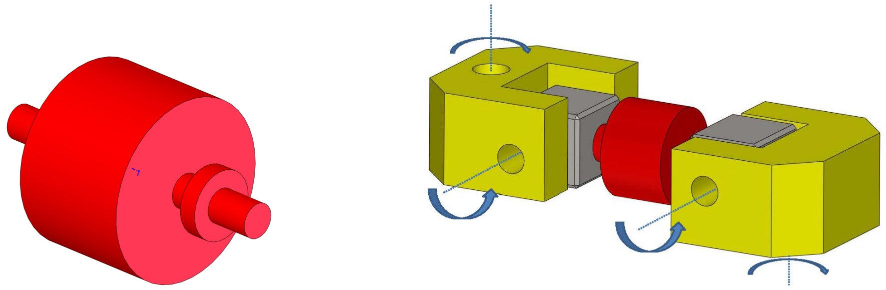

(a) Force transducer HBM-U9B **(b)** Force transducer HBM-U9B

Figure 4.22: Force transducer HBM-U9B - (a) The HBM-U9B 500N force transducer with axial load direction; (b) The force transducer (illustrated red) is screwed into the steel elements (illustrated gray) and fixed with contra screws. The steel elements (gray and yellow) are coupled with the horizontal shafts so that free rotation is allowed, as the blue arrow illustrates. A similar shaft exists for the vertical direction, connecting the plates and joint (yellow)

lateral direction (different than the rated direction). To avoid damage of the force cell, there should be no force acting in any other direction than the direction specified as a rated load direction. Thus, the force cell is connected to the plates through custom made joints with two degrees of freedom per joint. As illustrated in Fig.4.22b, the free rotation around the two axes of the joints will make sure that the position of the force transducer will adapt so that the rated load direction is maintained. During the operation the force cell nominal strain is measured in microns which means that the whole torque measurement assembly will be practically stationary. To minimize the friction between top and bottom plate, a 0.5 mm layer of Teflon lubricated with silicon oil was introduced.

The calibration of the torque measurement add-in had to be performed to experimentally determine the output from the load cell and applied torque. In order to carryout the calibration, a Newton meter was connected to a 0.8 m long bar (arm) connected to the top plate of the torque measurement assembly and several values of torque have been applied. The results of the calibration test are presented in the Fig.4.23.

During the calibration, the difference between strain gauge voltages and applied torques when torque was increased or decreased was observed. Thus, since the volt-

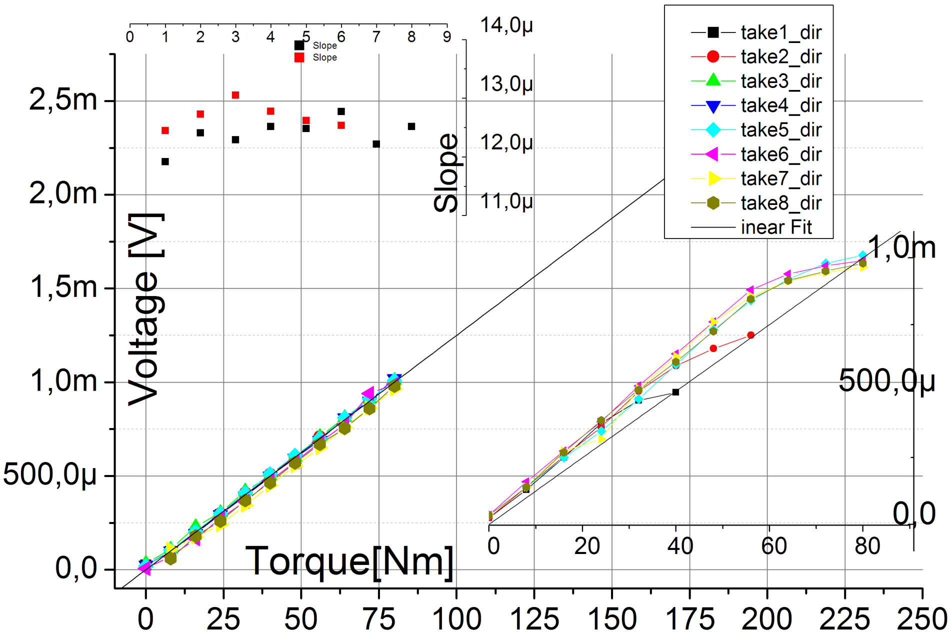

Figure 4.23: Torque measurement assembly calibration. - The relationship between the output voltage of the force cell and the applied torque for eight repeated measurements. The system is experiencing hysteresis, which is reported in the bottom inset, due to the static friction. The linear fit is performed on all 'takes' and the slopes derived are reported in the top inset. The black and red markers are denoting raising path (raising the torque) and returning path (lowering the torque) in the torque cycle.

age value depends on the direction of the change of the applied torque (increasing or decreasing), the measurement assembly performance will have hysteresis nature. The hysteresis present in the voltage - torque relationship is illustrated on the lower inset in the Fig.4.23. This effect is the consequence of the static friction between the top plate and the bottom plate. By averaging the slopes from all experiments, the conversion factor between voltage and torque is found be $12.6{\cdot}10^{-6}$ V/Nm.

4.6 Speed and Position Measurement

The speed and position measurement are custom fitted and integrated into the setup. A two channel optical encoder Honeywell HOA0901 – 012 (155) , with optical resolution of 0.45 mm was used. Accordingly, a code–wheel was designed to fit the encoder specification. The code-wheel was drawn in CAD software and printed on the transparent polyester foil (overhead foil) with the standard laser printer and with the standard resolution of 600 dpi. The code-wheel has an optical radius of R_{op}=197.8 mm and $N_{encoder}$=1350 dark–transparent cycles.

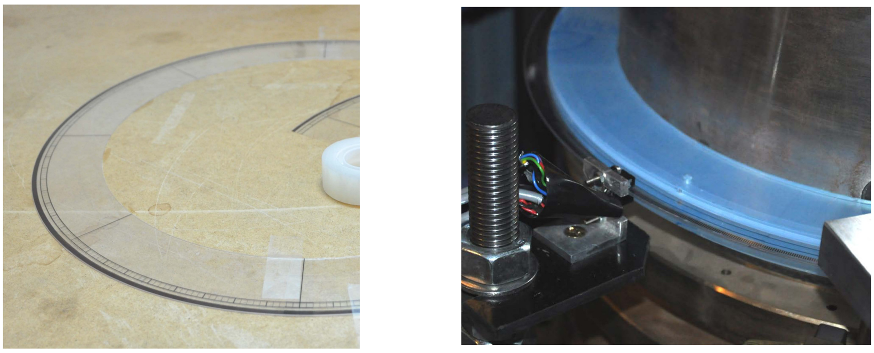

(a) The code-wheel for the encoder under construction

(b) Assembled encoder mounted on armature housing

Figure 4.24: The encoder add-in - (a) The code-wheel drawn with AutoCAD software was printed on a transparent polyester foil (overhead foil) with a standard laser printer in 600 dpi resolution. The code-wheel has an optical radius of R_{op}=197.8 mm and $N_{encoder}$=1350 optical windows. The transparent foil is glued on a 1 mm Plexiglas layer to make the code wheel more rigid. After, the code-wheel was pressed in between two 10 mm Plexiglas rings acting as a encoder housing. (b) The encoder mounted on the armature housing and encoder IC.

The two quadrature counter channels can resolve the direction and the magnitude of the movement with an accuracy of the 0.1 mm which at the R_{op} corresponds to an angle resolution of 0.033°.

4.7 Armature Position Locking

The electromagnetic torque is a function of the magnitudes of the magnetic fields and angle between them, as presented in Ch.3. These parameters, the magnitude of magnetic field and angular displacement of the armature winding with respect to the HTS field winding and their implication to HTS machine operation are important. At a later time, these parameters can be referred to the performance of the machine under different load conditions. With that purpose, a custom add-in was designed to lock the armature position at arbitrary angle with respect to the field winding (see Fig.4.25). The position of the armature can be monitored with high resolution with the encoder.

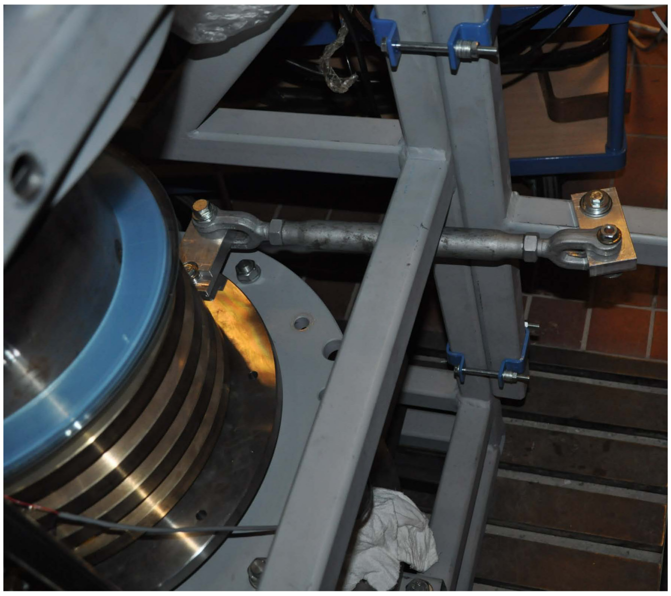

Figure 4.25: Armature winding lock assembly -

The disc attached to the armature housing at the bottom was used as coupling interface between the armature and an adjustable rod. The disk has axial holes along the circumference spaced by 45°. The position of the armature winding is set by adjusting the length of the adjustable rod. The armature position is locked by tightening the two contra nuts on the adjustable rod. The armature is able to rotate up to 60° with full change of the length of the adjustable rod after which the point of coupling on the disk needs to be changed to cover the next 60° (see Fig.4.26).

To investigate the performance of the HTS field winding at different armature fields (armature reaction) and different angles, the static tests were planned where the position of the armature winding with respect to the HTS field winding was controlled with the Armature Position Locking add-in. The test is illustrated in Fig.4.26 where the armature will rotate 60° for a full change of the length of the adjusting thread. The armature winding, static in space, is powered with a dc current entering one phase and exiting at the other two phases. The direction of the armature flux is thus controlled by the physical position of the armature winding and with the choice of the pairs of

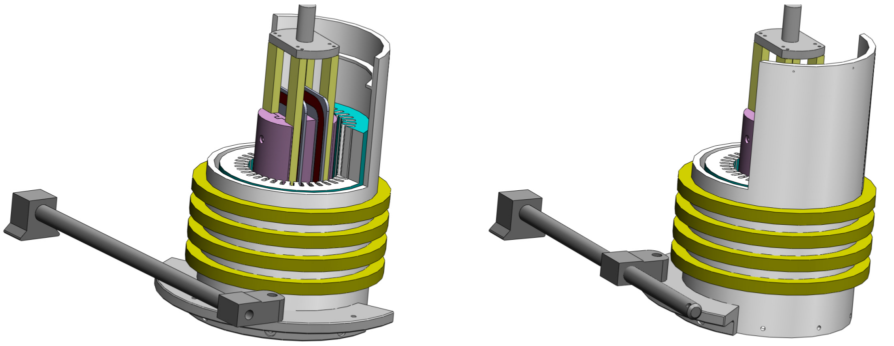

(a) The Armature Position Locking add-in at arbitrary position

(b) Position of the armature winding controlled

Figure 4.26: Procedure for Armature Locking experiment - (a)The Armature Position Locking add-in at arbitrary position. The armature winding is displayed in cut-off mode to correlate its position to the HTS field winding (b) Position of the armature winding controlled with the adjustment of the length of the rod in the Armature Position Locking add-in.

A	B	C	Stator field	A	B	C	Stator field
Two phases				All phases*			
1	-1	0	-30°	1	-0,5	-0,5	0°
1	0	-1	30°	-1	0,5	0,5	180°
0	1	-1	-90°	-0,5	1	-0,5	120°
0	-1	1	90°	0,5	-1	0,5	-60°
-1	1	0	150°	-0,5	-0,5	1	-120°
-1	0	1	-150°	0,5	0,5	-1	60°

Table 4.6: The armature winding field position with respect to the choice of the phases and current direction of each phase.

phase windings supplied with a current. Table.4.6 contains the angular shift of the armature field direction with respect to the magnetic field axis of phase A for various phase pairs.

As it can be seen from Table.4.6, for an angular span of the armature winding of 60°, every direction of the armature field can be covered by varying phase pairs, as illustrated in Fig.4.27. Using both two and three phases combinations, the number of angles could be doubled (from 6 to 12) but using all three phases calls for two power supplies (or some other way of achieving the half of phase current in other two phases). Due to a limited number of power supplies, just two phases at the time were used in the static experiments.

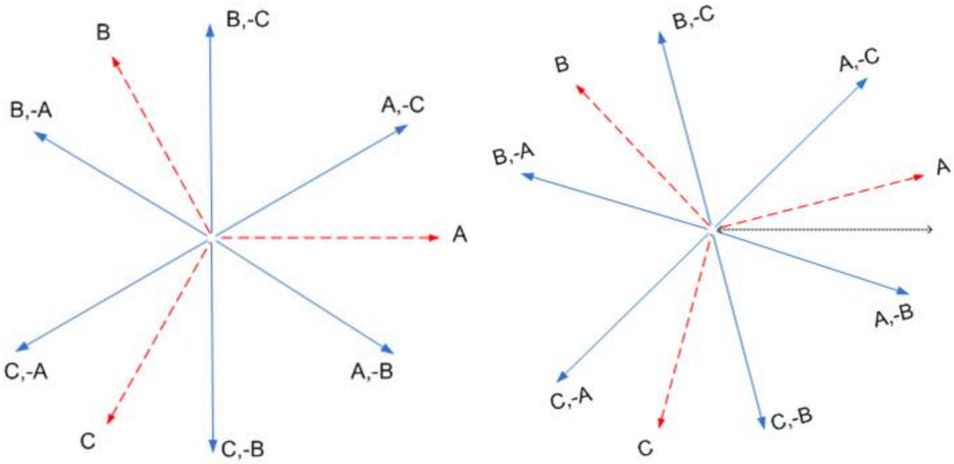

(a) The Armature Position Locking add-in at arbitrary position

(b) Position of the armature winding controlled

Figure 4.27: Armature Locking experiment: angular shift -

The armature reaction with a current I running through two phases is $\sqrt{3}/2$ lower compared to the the armature reaction when supplied with symmetric three phase currents where I is the amplitude of the current waveform. Thus, a correction factor needs to be taken into account when the analysis is carried out.

Chapter 5

Experimental Results and Discussion

"An Experiment, like every other event which takes place, is a natural phenomenon; but in a Scientific Experiment the circumstances are so arranged that the relations between a particular set of phenomena may be studied to the best advantage. " **by James Clerk Maxwell**.

This chapter will describe performed experiments intended to compare the performance of two configurations of the HTS coils in the field winding of the machine. In total, six HTS coils have been employed and all experiments were carried out at 77 K.

First, the HTS coils are characterized individually by determining the critical current and n value. Afterward, the coils were connected into a series connection and performance of both configurations of the field winding were analyzed. Section voltages of the coils were used to confirm critical parameters defined from a coil voltage both for the individual coils and for the field winding. The impact of an armature current on the HTS coils in the field winding was studied in depth where both armature current and an angle between the armature winding and the HTS field winding magnetic axis were varied. The interaction was quantified with the derived relation between the critical current of the field winding and the armature current. Consequently, the operational window of the HTS field winding was defined.

Furthermore, two methods to increase the performance of the HTS field winding are proposed and their implication discussed. Finally the HTS machine parameters are determined and discussed.

5.1 Field winding configurations

Flexibility of the experimental setup was one of the primary milestones of the design as described in the previous chapter. Thus, two different configurations of the field winding were planned to be subjected to experiments in order to investigate conceptual differences between 1G and 2G coils and their position in the field winding.

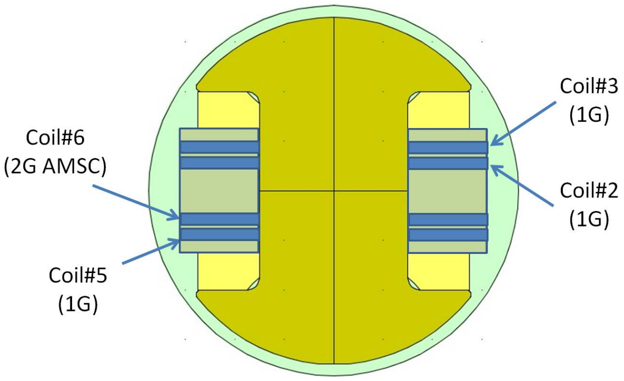

(a) Arr1

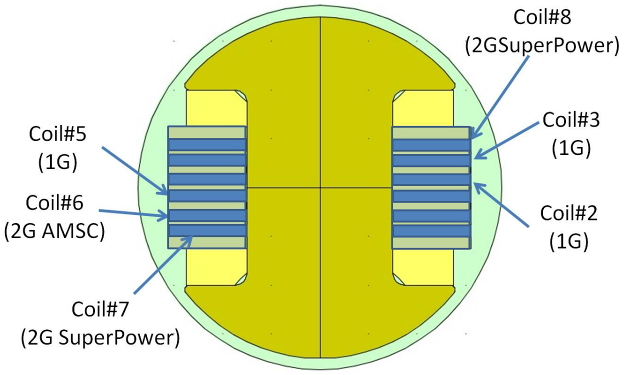

(b) Arr2

Figure 5.1: Field winding configurations - Two arrangements of the field winding.

Two arrangements of the HTS field winding are presented in Fig.5.1. In the first arrangement (Arr1), the HTS field winding comprises 4 coils in total with three 1G coils ($Coil\#2$, $Coil\#3$ and $Coil\#5$) and one 2G coil ($Coil\#6$). The 1G coils are placed closest to the poles while $Coil\#5$ and $Coil\#6$ are in the middle of the field winding. In the second arrangement, Arr2, the HTS field winding carries 6 coils where additional 2G coils, $Coil\#7$ and $Coil\#8$, have been placed closest to the poles. It may be noticed that the placements of the $Coil\#6$ and $Coil\#5$ were exchanged and $Coil\#5$ is moved to the middle of the field winding. Thus, the performance can be compared to the first arrangement where it is closest to the pole shoe and 1G and 2G technology can be evaluated with respect to the position in the HTS winding.

To make the comparison between Arr1 and Arr2 more transparent, a subset of four coils (from six) in Arr2 have been isolated as a coil set of interest. This includes the same coils as in Arr1 but with alternated positions of $Coil\#5$ and $Coil\#6$ during which $Coil\#7$ and $Coil\#8$ were inactive. This configuration of the field winding will be referred to as Arr2. In addition, the case where all six coils are active ($Coil\#7$ and $Coil\#8$ are active too) will be referred as Arr2-b or Arr2-c, depending on the current of $Coil\#7$ and $Coil\#8$.

Preformed experiments can be divided into two groups, static experiments where the armature winding is stationary and spinning tests where the armature winding is revolving at a given speed. Static experiments are carried out in order to determine and compare performance of the HTS coils in different configurations of the field winding and to define the operational window of the field winding. In addition, these tests will also provide insight in the machine performance as the interaction between the armature and the field winding is analyzed.

The spinning experiments are on the other hand preformed to experimentally determine parameters of the HTS machine such as direct and quadrature inductance, leakage inductance, induced electromotive force and so on.

5.2 HTS coils operation and individual IV curves

The design and performance of the HTS machine is largely governed by the performance of the HTS coils. Thus, the first step is to determine the amount of MMF the HTS coils can generate. As the I_c presents the maximal current the HTS tape can sustain for an indefinite time, it will be used as a parameter defining the boundary of the maximal performance of each HTS coil and ultimately, the field winding. The operational current in an industrial application should be 40%-90% of I_c (156) in order to ensure safe operation of the winding over its lifetime and minimize the energy loss in the field winding. The choice of operating point and safety margin for an HTS current loading highly depends on the machine design specifications, HTS tape parameters and coil thermal stability (157, 158, 159). Regardless, the critical parameters of an HTS winding must be identified first.

The I_c and n as characterization parameters of superconductors, defined in Ch.2, are derived under assumption that the HTS is in homogeneous conditions with respect to the temperature and magnetic flux (which is the case in the *short sample* experiment (21)). For HTS coils and complex superconducting devices (cables, FCL, machines, magnets, etc.), temperature and flux conditions are not uniform, but the voltage - current relations can be described with a power law dependency. The connection between I_c and n value derived from a *short sample* test and derived from the coil could be made (160) but is not straightforward.

The I_c and n value for the HTS coils are derived from an integral voltage across the entire length of the HTS tape in the coil, U_{coil}, which can be expressed with

$$E_{coil} = \frac{U_{coil}}{L_{coil}} = \frac{E_0}{L_{coil}} \int_0^{L_{coil}} \left(\frac{I}{I_c(\mathbf{B},T)} \right)^{n(\mathbf{B},T)} dL \rightarrow \frac{U_{coil}}{L_{coil}} = E_0 \left(\frac{I}{I_c} \right)^n \tag{5.1}$$

where L_{coil} is the length of the HTS tape in the coil winding, I is the current of the coil, I_c is the critical current of the HTS coil and n the transition coefficient describing how abrupt the transition between superconducting and resistive state is.

It is important to keep in mind that the I_c determined from the coil voltage could lead to overestimation of the current rating of the HTS coil, especially if the flux distribution across the HTS coil contains large gradients. Therefore, 5.1 should be used with caution when deriving the I_c of the coil where flux gradients are large. Consequently, the analysis of IV curves from different sections of HTS coil coupled with FE simulations can be used as a supplemental analysis in order to verify the critical parameters (I_c and n) derived from the coil voltage (ensuring that all coil segments are operating under similar conditions).

5.2.1 *I-V* of individual HTS coils

Experiments where the current is increased stepwise and the coil voltage is monitored, resulting in characteristic nonlinear current - voltage relation (so called IV curves), were conducted for each coil separately. The current steps were 0.25 A – 5 A depending on desired resolution of the IV curves and the HTS type. The pace of current increase was maintained very slowly, allowing $\sim$ 1 min between each step, so the coil voltage could stabilize.

The IV curves for each coil in the field winding are shown in Fig.5.2 and Fig.5.3 for Arr1 and Arr2, respectively. The I_c of the coil in the self produced leakage flux of the machine is derived from these IV curves and reported in Table.5.1. The values of I_c and n are almost the same for both configurations of the field winding, which is expected.

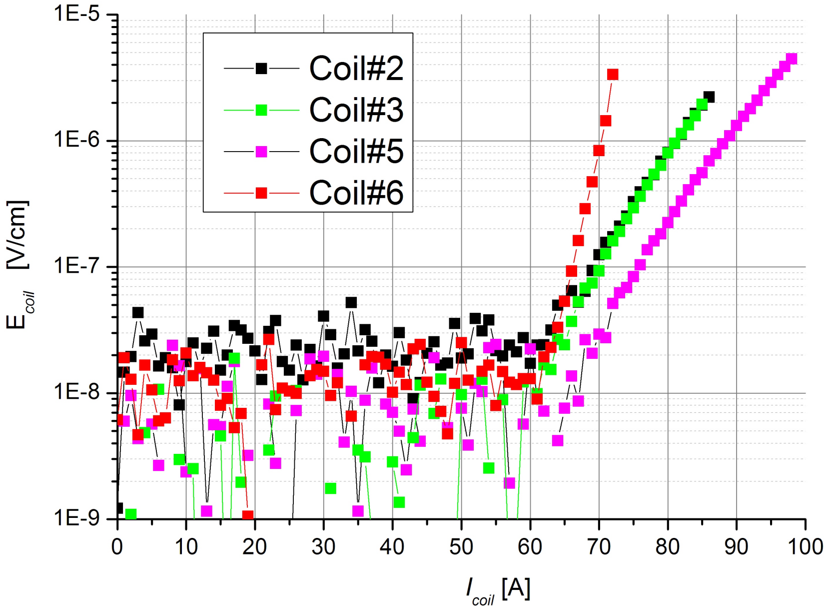

Figure 5.2: The individual IV curves for the four HTS coils in Arr1. - The individual IV curves for *Coil*#2, *Coil*#3, *Coil*#5, *Coil*#6 are presented. Power law fits were preformed and the obtained I_c and n values are listed in Table.5.1 for each of the coils using E_0=1μV/cm (E_0=100μV/m) as a critical voltage criteria.

The coils are mounted on the cold steel in both arrangements and the MMF created by the individual coil ($\sim$ 4000 AmpTurns) is not enough to saturate the cold steel. Most of the flux is contained in the cold steel and the stray flux is mostly parallel to the HTS tapes. Thus the flux conditions are favorable for the HTS tape performance and are independent from the position of the coils in the field winding.

Derived values for I_c of individual coils are in line with expectations for most of the coils. 1G coils are performing very well in low field conditions with relatively low n value. The 2G coil in Arr1 has significantly higher n value with slightly lower critical current.

The field winding in Arr2 consists of six coils, with $Coil\#7$ and $Coil\#8$ added to the previous set of coils. Unfortunately, the IV curves for the two new 2G coils indicate that the coils were damaged during winding or cool–down. Consequently, defect has reduced their I_c to 12 A and 30 A for $Coil\#7$ and $Coil\#8$ respectively. This is lower than the expected (40 A – 60 A) considering the I_c of the HTS tape in self field. Since the coils are with defect, the IV curves have also a dominant resistive nature seen in the very low n value.

Coil ID	L_{coil} [cm]	No. of Turns	Arr1 $I_c[A]$ - n	Arr1 $J_c^e[A/mm^2]$	Arr2 $I_c[A]$ - n	Arr2 $J_c^e[A/mm^2]$
Coil2	2540	48	81.2 - 15.3	39.0	81.3 - 14.9	38.9
Coil3	2880	51	81.3 - 14.8	41.4	80.8 - 13.9	41.4
Coil5	2500	46	88.5 - 14.5	40.7	88.3 - 14.2	40.7
Coil6	3165	56	70.2 - 52.3	39.3	70.6 - 46.2	39.3
Coil7	7000	125	N/A	N/A	12.4 - 2.8	15.4
Coil8	7000	125	N/A	N/A	31.6 - 3.0	39.5

Table 5.1: Critical parameters derived from IV experiments for six HTS coils. The critical current I_c, n value and engineering current density of a coil, J_c^e, are listed for both configurations of the field winding. The J_c^e was calculated as a ratio of the Amp-Turns the coil has at critical current I_c with the cross section of the coil, A_{coil}=20 mm × 5 mm.

5.2.2 Coil sections

The voltage of the sections for all coils was monitored during IV experiments and was used to verify the value for I_c, derived from the coil voltage. Fig.5.4 displays the IV trace for the inner and outer sections of $Coil\#3$ (details about HTS coils and sensing points are presented in Ch.4 and are included in Appendix.**??**).

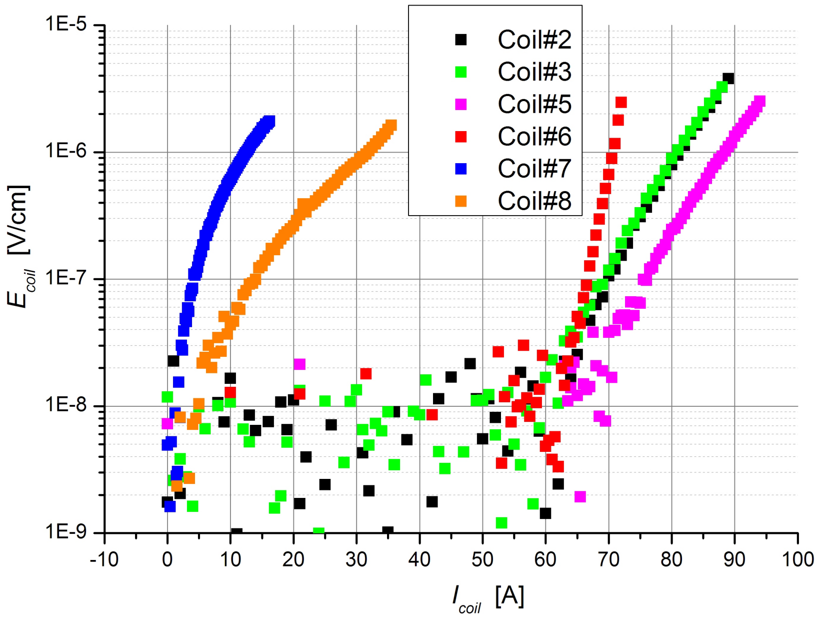

Figure 5.3: The individual IV curves for all six HTS coils in Arr2. - The individual IV curves for *Coil#*2, *Coil#*3, *Coil#*5, *Coil#*6, *Coil#*7, *Coil#*8 are presented. The power law fit was performed and I_c and n values are reported in Table.5.1 for each of the coils using E_0=1μV/cm (E_0=100μV/m) as a critical voltage criteria.

The coil *Coil#*3 shows a noticeable difference between the performance of the inner and outer sections of the coil for both configurations of the field winding. The difference in the I_c is ~5 A (the I_c for the inner section is 84 A while the I_c for the outer section is 79 A) for Arr1 and just ~3 A in the second arrangement of the field winding. According to the IV curves for sections of other coils, the difference between the sections was small and thus it is believed that the I_c derived from the voltage of the coil is sufficiently precise.

Interesting results were obtained when the sections of coils with defects were analyzed. After a closer look into the IV curves of the inner and outer sections of *Coil#*8, presented in Fig.5.5, it was clear that the inner section of the coil is the one that suffered the damage. Similar performance of sections was observed with *Coil#*7. Even though this finding has little impact on this particular coil, the information that the inner section of the coil contains defect is very valuable. It indicates that the inner section of the 2G coils based on the SuperPower tape needs to be debugged. At a later stage this information can be used as a useful input for analysis of the winding

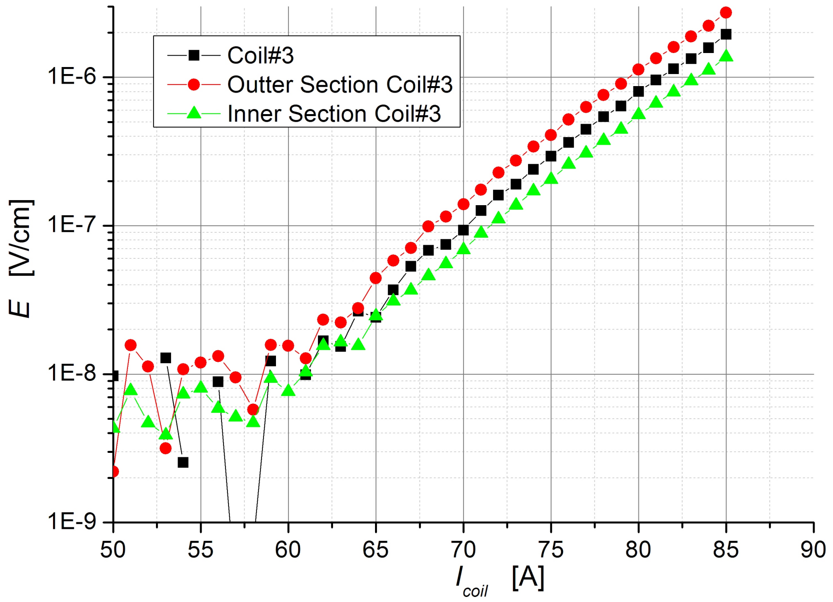

Figure 5.4: The IV curves: Sections of *Coil*#3. - The figure shows the IV curve for *Coil*#3 including the coil sections. Only coil *Coil*#3 demonstrates noticeable difference between the performance of the inner and the outer section of the coil. The difference in the I_c is ~5 A (the I_c for the inner section is 84 A while the I_c for the outer section is 79 A) when the coil is in Arr1.

approach and coil design revision.

Fig.5.5 is showing one more interesting thing. It is noteworthy to mention that during testing, Coil#8 actually quenched at 36 A. A quench is a thermal runaway of the HTS conductor (159) that conducts a current where voltage instantly (vary fast) rises until either HTS tape is destroyed (burnout) or the quench protection system intervenes. The Superwind setup does not have a distinct quench protection system. Instead, the voltage limit of the power supplies used in experiments was kept close to the voltage that the HTS coil would have at critical current (approximately 150%–500% of the critical voltage). In this way, even if a thermal runaway occurs, the voltage and thus the power dissipation of a quenched section will be limited. That is the reason why the voltage of *Coil*#8 stopped at approximately $10E_0$=10 μV/cm. The IV tests were repeated twice after quenching and it was concluded that quenching did not degrade the previously determined value of I_c. The outer section of the coil shows the tendency towards voltage increase at currents above 30 A. This can either be because I_c value of

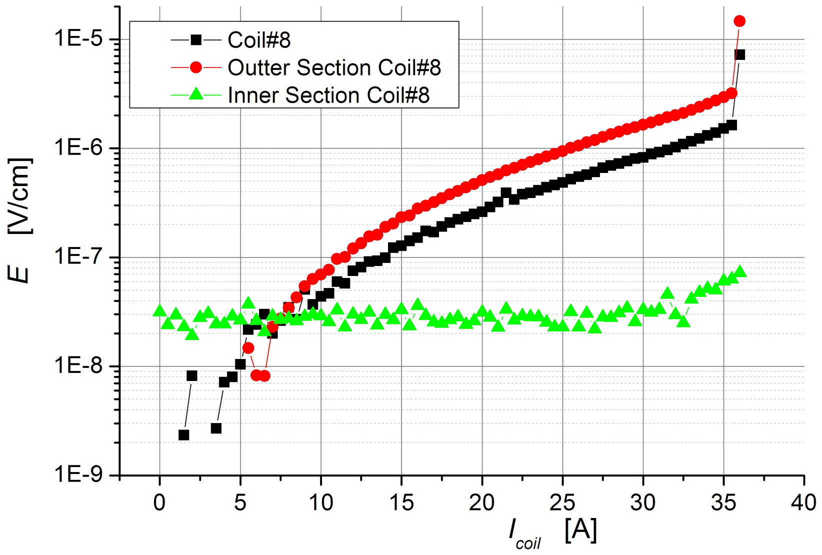

Figure 5.5: The IV curves for outer and inner section of *Coil#8*. - The inner section of the coil shows resistive character and indicates that the coil was damaged. The inner section of the coils experienced the quench at 36 A.

the healthy portion of the coil is close (45 A – 55 A) or because the hot spot (quench section) had caused a slight increase in temperature of the whole coil.

It may be an exaggeration because of the defect, but both *Coil#7* and *Coil#8* are perfect examples of the value closer investigation of the coil sections have and how largely overestimated the value for I_c based on the coil voltage can be.

5.2.3 Magnetic conditions during IV tests

Before going any further it is important to state that FE simulations used to evaluate the magnetic conditions that the HTS coils were exposed to during the experiments did not include superconducting physics. Thus the current distribution in each of the HTS tapes was simulated as a uniform engineering current density. In reality, the current distribution in the cross-section of the HTS tape will be a function of magnetic field (both vector and history) and the local properties of HTS material (161). Consequently, even though the net current of each turn is the same, each turn of the coils will have a different current distribution where for example edges of the tapes could have J_c and the middle $-J_c$/(22). Taking this into account and incorporating this effect into FE simulation is possible (162) and will yield correct magnetic and current distribution in the coil.

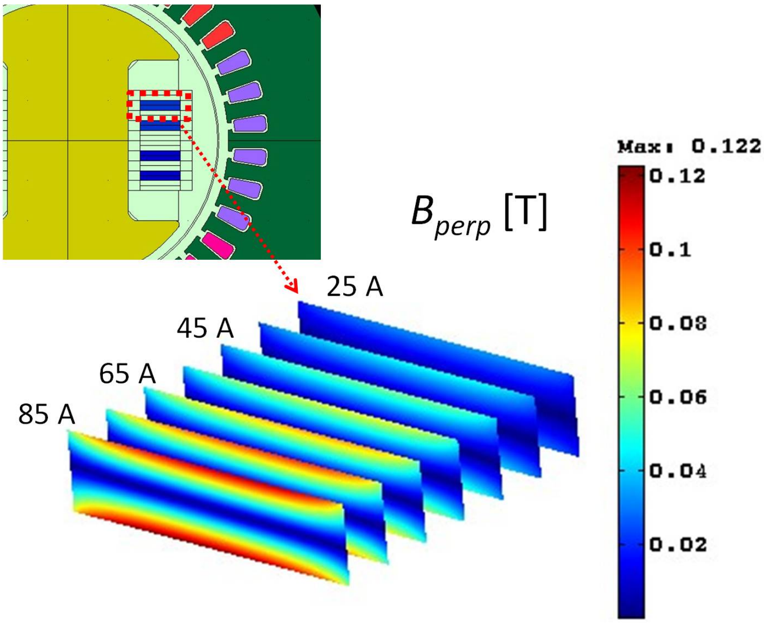

Figure 5.6: The distribution of the flux density perpendicular to the HTS turns in *Coil*#3. - The FE simulation results of the flux density perpendicular to the HTS turns while current of the coil is ramped up from 25 A to 85 A, in steps of 10 A. The FE simulation assumes uniform current distribution in the HTS turns.

However, this chapter will use FE simulations to estimate global magnetic conditions in the field winding and the HTS machine, on which the local current distribution in the turns of the HTS coils has a very limiting effect. To evaluate magnetic conditions during individual IV experiments, FE simulation of the corresponding experiments are analyzed. The coils have during the individual tests generated approximately 70 mT of self field at critical current. The distribution of perpendicular flux to tapes for *Coil*#3 is shown in Fig.5.6.

5.2.4 Summary of IV tests for individual coils

For performed IV tests and critical parameters derived from the measurements, the following stands out:

- The coils *Coil*#2, *Coil*#3, *Coil*#5, *Coil*#6 have performed as expected. The values for the I_c of the coils are in agreement with the values for the I_c of the

HTS tape.

- Both $Coil\#7$ and $Coil\#8$ were found to be defective with significantly lower values of I_c than expected. A portion of the coils have failed to become superconducting and the distinct resistive IV relation was observed.
- During IV experiments, the inner section of $Coil\#8$ survived the quench that happened at 36A.
- Monitoring the voltages of the sections of a coil has proved to be a valuable diagnostic tool for detection of defects, troubleshooting the coil design and coil production process and finally verifying the I_c and n values.
- With exception of $Coil\#3$, the inner and the outer sections of coils have the same tendencies and thus it can be concluded that the I_c derived from the voltage of a coil is sufficiently precise for this particular case. The inner section of $Coil\#3$ exhibits a 5A lower value for I_c.

5.3 The HTS field winding in series

An HTS coil can be seen as a number of short pieces of HTS tape with individual IV curves, where the coil voltage will be a sum of all voltages from short pieces. Ideally, the short section exhibiting the lowest I_c would set the I_c of the coil, but as this information is almost never available, the average I_c is derived using 5.1. A similar approach can be used for a set of HTS coils. If the coils in a field winding are connected into a series connection in such way that individual MMF adds up, all coils will have the same current. The operating point for the HTS field winding connected in to a series will be defined by the coil with the lowest I_c value. In other words, among a number of coils operating with the same current, a coil with voltage equal to the $E_0 L_{coil}$ will be the one with lowest I_c. This is expressed as,

$$MAX\left(\frac{U_{coil}^{i}}{L_{coil}^{i}}\right) \leq E_0 \tag{5.2}$$

where the coil index i takes values from the coil ID array for coils present in the field winding. For Arr1 the index i would take values from $[Coil\#3, Coil\#2, Coil\#5, Coil\#6]$.

In the next section results for the Arr1 and Arr2 will be presented and implications of coil placement will be discussed. The IV curves recorded for both configurations of the HTS field winding are presented in the Fig.5.7 and Fig.5.8.

5.3.1 Field winding in Arr1 – series connection

In the first arrangement, the coil limiting the MMF of the HTS field winding is $Coil\#3$ closely followed by $Coil\#5$. As a result, the field winding is able to operate with currents $\leq$52 A. The reduction of I_c of $Coil\#3$ is large (from 81.3 A down to 52.2 A) if I_c of the individual coil and series connected coils are compared. The reduction of the I_c of $Coil\#5$ is even larger (from 88.5 A down to 54.3 A). The I_c reduction is due to the increased magnetic flux density these coils are exposed to.

$Coil\#3$ and $Coil\#5$ are showing larger reductions in the I_c value because their position in the field winding is unfavorable. Due to their proximity to the pole shoes and the tendency of the flux lines to escape cold steel close to pole shoes, these coils will experience significantly higher magnetic flux perpendicular to HTS tape. As the cold steel gradually saturates with increase in the MMF, the leakage flux of the coils will increase, making the reduction of I_c even higher.

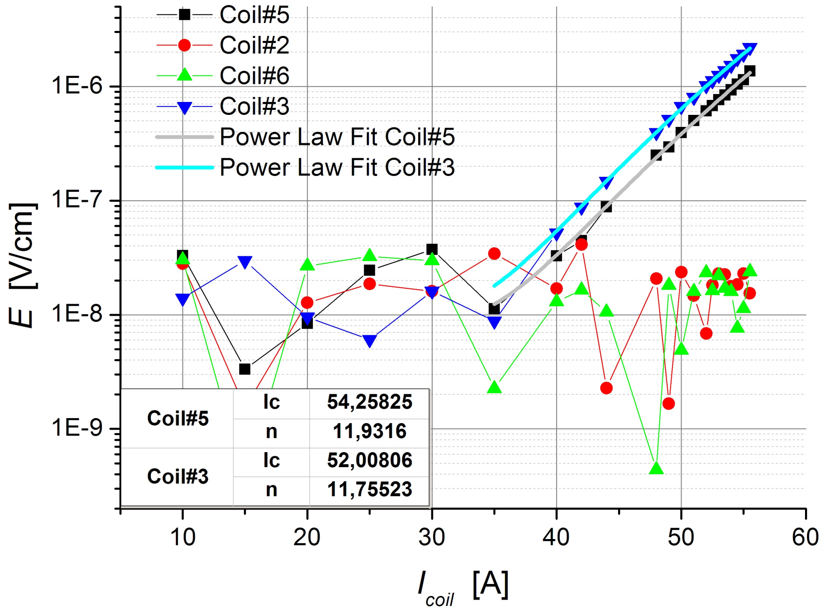

Figure 5.7: The IV curves for HTS field winding in Arr1 - The IV curves recorded for the series connected HTS field winding in the first arrangement.

This is a validation of a well known feature of a 1G HTS conductor, i.e. 1G has high sensitivity to magnetic field (especially to the flux perpendicular to an HTS tape) at high operating temperatures (77 K). The effect of magnetic anisotropy in 1G HTS tape is lower at lower temperatures. The inner coils, *Coil*#2 and *Coil*#6 are according to Fig.5.7, far from critical values. The implication that *Coil*#2 shows no I_c degradation (at least not as same as *Coil*#3) is the indicator that inner coils are exposed to a lower value of magnetic field.

5.3.2 Field winding in Arr2 – series connection

With the field winding in Arr2 and four coils connected in series (excluding the coils *Coil*#7 and *Coil*#8), the IV curves are shown in Fig.5.8. Now the *Coil*#5 is in the middle of the field winding together with *Coil*#2, while *Coil*#3 remained at the same place and *Coil*#6 was placed closer to the pole shoe.

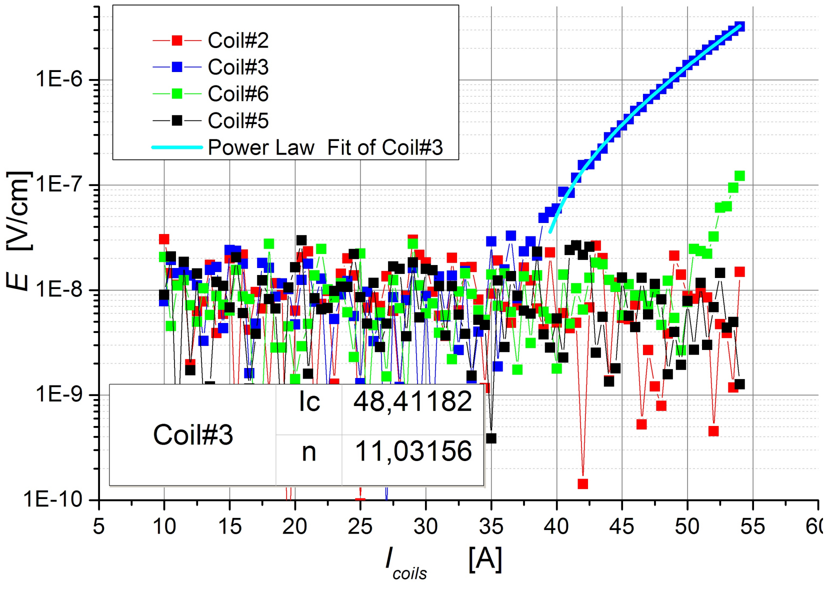

Figure 5.8: The IV curves for HTS field winding in Arr2 - The HTS field winding in Arr2 connected in series.

Here, similar to the Arr1, *Coil*#3 has the lowest I_c, setting at 48.7 A, a slightly lower value then in Arr1. A significant difference in the performance between these two arrangements is seen for *Coil*#5 as expected. Placing *Coil*#5 in the middle of the field winding once again confirms the significance of the magnetic flux density for the coils wound with 1G tape. As a consequence, $Coil\#5$ in this arrangement indicates that the I_c value is substantially higher than in Arr2. On the other hand, placement of $Coil\#6$ at the outer layer of the field winding did not noticeably degrade its critical current. This will be discussed in more details later on.

5.3.3 $Coil\#3$, a weak link in the field winding

The coil which limits the current of the field winding in both arrangements is $Coil\#3$ and it is of special interest to investigate the nature of the I_c dependence from MMF of the field winding for this coil.

5.3.3.1 Critical current of $Coil\#3$ vs. MMF

To investigate the I_c reduction with respect to the current in the other coils, an experiment was carried out in Arr2, where $Coil\#3$ has slightly lower I_c. The set of IV curves for $Coil\#3$ with the background magnetic field, was recorded. The starting (offset) magnetic field was provided by the other three coils connected in series. Their current was increased stepwise (in steps of 5 A) and kept constant while the IV experiment was performed on $Coil\#3$.

Fig.5.9 presents the results from this experiment. Each contour separating the region in the graph with single color represents specific level of the electric field of $Coil\#3$. The color legend is included in the graph, wherein the number of levels is identified. Instead of fitting a number of IV curves, the I_c tendency can be derived from the electric field level. The contour for electric field equal to E_0 will represent that critical line and it is marked with a wider line (contour) in the graph.

It can be observed that the reduction of I_c is a nonlinear function of background MMF. The reduction can be as high as 50% for Arr2. This is an expected result as the performance of 1G HTS tape at 77 K will strongly depend on magnetic field (both intensity and direction).

5.3.3.2 Magnetic conditions for $Coil\#3$

The magnetic flux density (intensity and distribution) across the field winding for individual coils was reported to be approximately 70 mT for the individual coil IV experiment. Since we saw a high reduction of the I_c when connecting the coils in series,

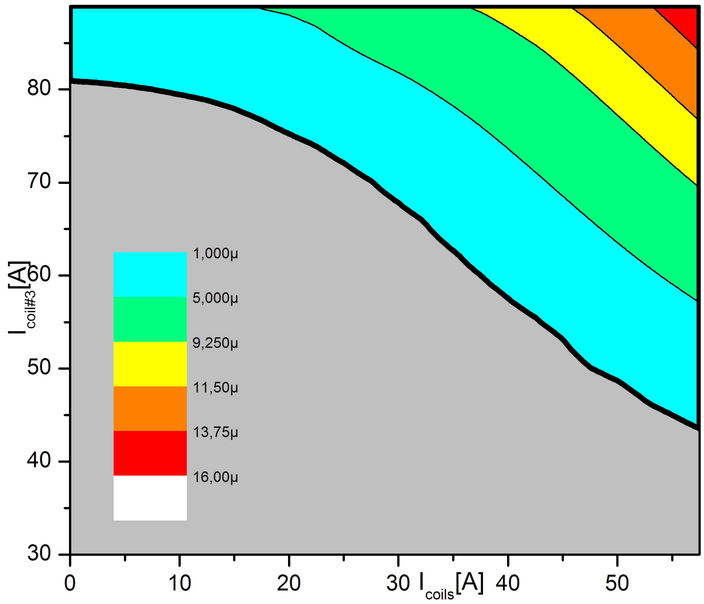

Figure 5.9: Critical current of $Coil\#3$ as a function of background MMF. - The electric field of $Coil\#3$ is presented with different colors. The contour with value equal to E_0 will correspond to the I_c of $Coil\#3$. This contour is emphasized in the graph with increased width of the line. The background magnetic field is generated by current in $Coil\#2$, $Coil\#5$ and $Coil\#6$ connected into series.

it is of interest to see what magnetic conditions are present at the field winding in this case.

An estimate of perpendicular magnetic flux density for $Coil\#3$ in both arrangements are presented in Fig.5.10 and Fig.5.11. The results are showing that the HTS tapes of $Coil\#3$ are exposed to the maximal magnetic flux density of $\leq$200 mT at I_c which is three times higher than in the individual IV test. The simulation shows slightly lower value of 183 mT for $Coil\#3$ in Arr1 compared to 195 mT observed for Arr2. Even though these simulations do not represent precise flux distribution in the HTS coil, the results from FE and experiments are in agreement (Since $Coil\#3$ has I_c=52 A for Arr1 and I_c=49 A for Arr2). This confirms that uniform current density of the HTS coil used in the FE model is sufficient to predict the magnetic conditions of an HTS coil.

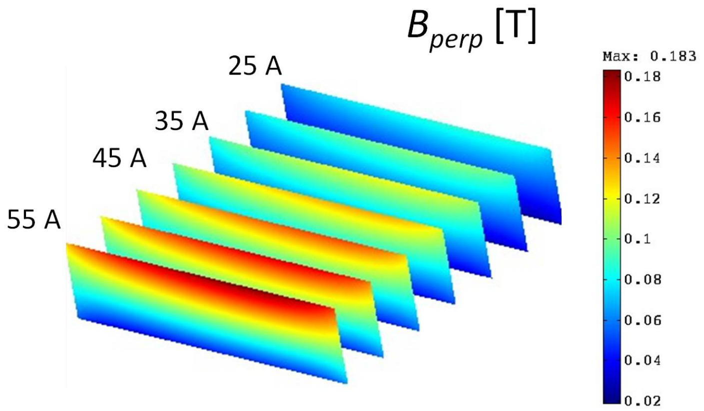

Figure 5.10: Arr1 - The distribution of the perpendicular flux density for *Coil*#3 while field winding in Arr1 is connected in series. Each color-plot slice represents the perpendicular flux distribution turns of the coil *Coil*#3 are exposed to. Current of the winding was increased from 25A–55A in steps of 5A.

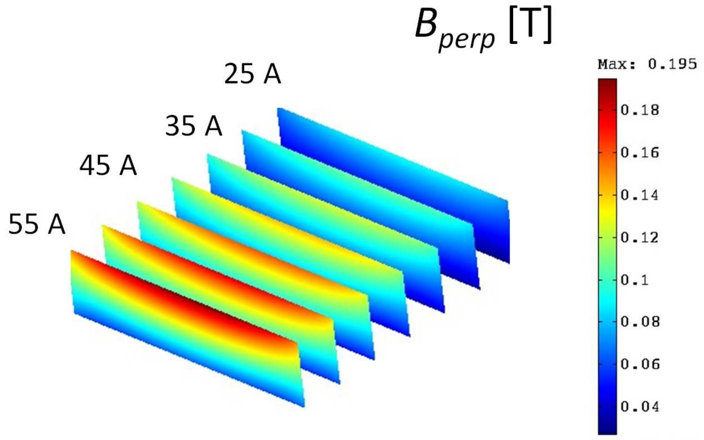

Figure 5.11: Arr2 - The distribution of the perpendicular flux density for *Coil*#3 while field winding in Arr2 is connected in series. Each color-plot slice represents the perpendicular flux distribution turns of the coil *Coil*#3 are exposed to. Current of the winding was increased from 25A–55A in steps of 5A.

5.3.4 Comparing 1G and 2G coils

The premise of the Superwind setup in part was to investigate both 1G and 2G HTS technology. One way to compare the performance of these could be by comparing the performance of 1G and 2G coils in different configurations of the field winding. With that reason, field winding was assembled and tested in two arrangements, and the coils in the focus of the discussion are $Coil\#5$ and $Coil\#6$.

Comparing Arr1 and Arr2, the tendencies of $Coil\#5$ to have larger reduction of I_c if placed closer to the pole shoe (Arr1) than if placed in the middle of the coil stack (Arr2) implies that the performance of 1G coils could be improved substantially if they are strategically placed in the field winding. To investigate the degree of the improvement the change of position can cause, we will analyze $Coil\#5$ in Arr2 and compare it to Arr1. Even though, $Coil\#6$ was far from its I_c in both arrangements, according to Fig.5.7 and Fig.5.8, in order to compare 2G coil performance to 1G coils, we need to investigate how the performance of $Coil\#6$ changed between arrangements. This will be presented in next section.

5.3.4.1 Performance of $Coil\#6$ (based on AMS348 2G HTS tape)

The reduction of the I_c value for $Coil\#6$ can be observed in Fig.5.12, where the family of the IV curves was recorded in the background field (generated by the other three coils). The current in the three coils was increased in steps of 10 A from 0 A to 60 A and kept constant during the IV experiment. The results in Fig.5.12 are for Arr1.

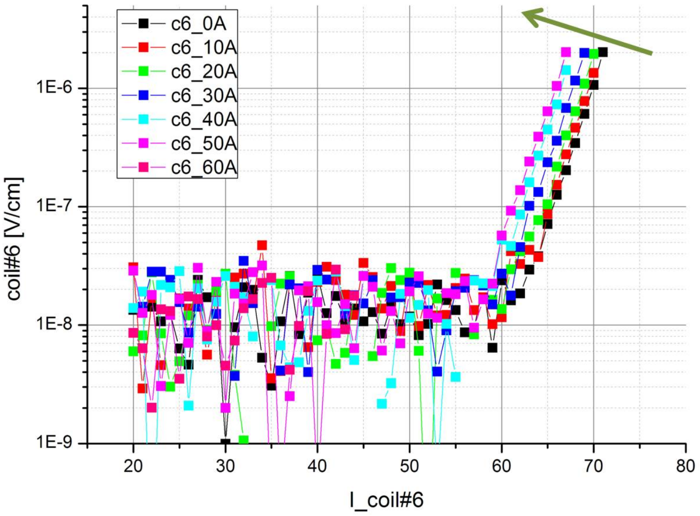

Figure 5.12: The IV curves of $Coil\#6$ in the field winding - The IV curves have indicated a change in I_c due to background flux of $Coil\#6$.

The increase in the magnetic field of the field winding will cause the IV curve of the coil to gradually move to the left as indicated in the Fig.5.12 with the green arrow.

This can be quantified with a reduction in I_c value of the coil. The critical current of $Coil\#6$ as a function of the current in the other three coils is presented in the Fig.5.13 for both arrangements. For the Arr1, the plot is constructed from a number of power law fits performed for the IV curves presented in the Fig.5.12 where the power law fit was performed in order to investigate the change in I_c of the coils but also of the n value as a function of the current in other three coils. We can see that the reduction in critical current of this coil is approximately 6% (from 70 A down to 65.8 A) while the n value stayed more or less the same. For the field winding in the second arrangement no power law fits have been performed, but instead the average electrical field defined by 5.1 equal to 1μV/cm (100μV/m) was identified as a function of $I_{Coil\#6}$ and the current in other three coils connected in series, I_{coils}. The decrease of I_c of $Coil\#6$ in Arr2 is ~15% (from 71A down to 61A) which is larger than in Arr1.

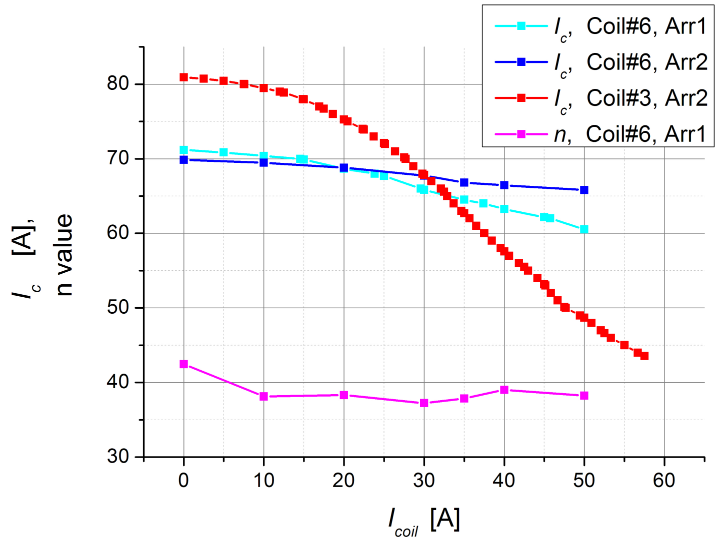

Figure 5.13: The I_c and n of $Coil\#6$ versus current in the other three coils for Arr1 and Arr2. - The influence of background field from other coils in the HTS field in the Arr1 and Arr2 on the I_c and n value of $Coil\#6$. The I_c of $Coil\#3$ is included to illustrate the degree of difference between two types of HTS. The 1G HTS has substantially higher I_c in the low field where the 2G HTS is less susceptible to the magnetic field.

5.3.4.2 Performance of *Coil*#5

Coil#5 is the representative of the 1G coils which had both outer and inner positions in the field winding in Arr2 and Arr1, respectively. For Arr1, the I_c of the field winding presented in Fig.5.7 reveals that *Coil*#5 has a critical current of 54.2 A. Thus, from the individual coil IV experiment to the series connected field winding, the I_c of the coil has reduced from 88.5 A (see the Table.5.1) to 54.2A which adds to the 39% reduction due to the increase in magnetic flux.

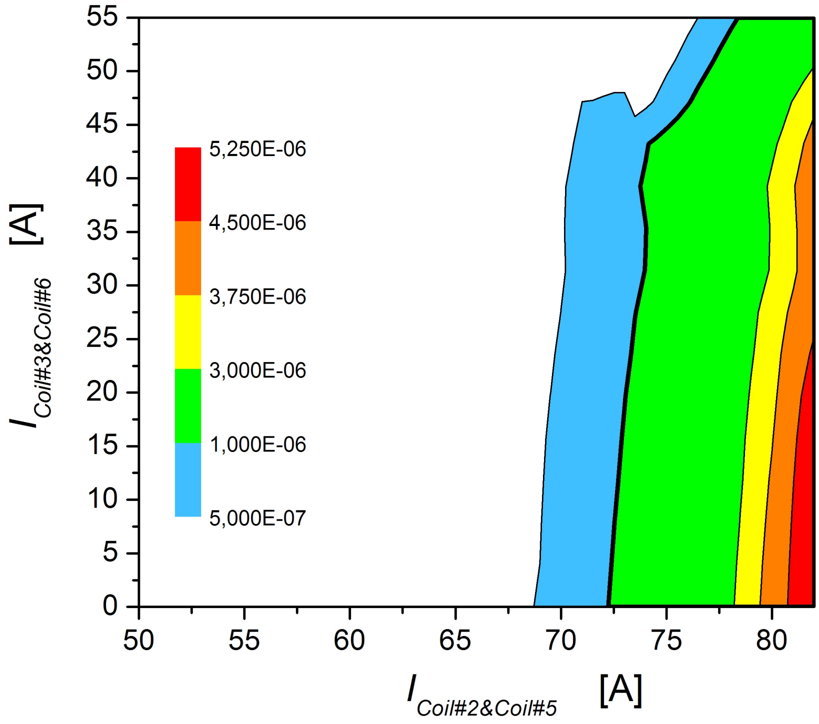

Figure 5.14: Electric field of *Coil*#5 in Arr2 - The electric field of *Coil*#5 in Arr2 is shown as a function of the current in *Coil*#5 and *Coil*#2 at X axis and the current in *Coil*#6 and *Coil*#3 at Y axis. Color legend of the electric field level is included where the E_0 level is between blue and green surface.

A slightly different experiment was carried out in the case of the field winding in Arr2. The inner and outer coils were paired up, making *Coil*#2 and *Coil*#5 the first and *Coil*#3 and *Coil*#6 the second coil pair. Each pair had one current supply. This was done in order to maintain the symmetry of the magnetic flux in the field winding and still show improved performance of *Coil*#5. Thus, here the background field is created by the second pair of coils and the IV experiment included both coils in the first pair. The voltage of $Coil\#5$ is presented in Fig.5.14 as a function of these two currents.

This experiment cannot be directly compared to the $I_c(I_{Coils})$ derived for other coils ($Coil\#3$ and $Coil\#6$) since $Coil\#2$ and $Coil\#5$ are paired together. Still, if we know that the I_c of $Coil\#5$ in Arr1 is ~55 A and compare this to the I_c of $Coil\#5$ in Arr2 of ~75 A for the described experiment, it is clear that 1G coils perform much better if placed in the middle of the coil stack. The E_0 electric field level is at the range of ~70 A at the far right of the plot and with increasing $I_{Coil\#3Coil\#5}$, this line migrates further right. This effect will be discussed in more depth further on in the Sec.5.6.2.

5.3.5 Summary for the HTS field winding connected into a series

- Field winding connected in series in Arr1 has I_c=52.0 A which is limited by $Coil\#3$.
- Field winding connected in series in Arr2 has I_c=48.7 A which is also limited by $Coil\#3$.
- The $I_c(I_{Coils})$ for $Coil\#3$ have showed a nonlinear reduction of I_c with reduction equally great in both arrangements of field winding (40% for Arr2).
- Analysis of sections of $Coil\#3$ have confirmed that the outer section of the coil has ~3 A lower value of I_c than the inner section.
- The $I_c(I_{Coils})$ for $Coil\#6$ have showed mild nonlinear reduction tendency of I_c with reduction of 6% for Arr1 and 15% for Arr2 at corresponding critical currents.
- The performance of $Coil\#5$ was found to be better for Arr2. The coil was capable of carrying $\leq$75 A for much higher values of MMF of the field winding than the MMF of the field winding at 48.7 A which is the critical current for Arr2.
- Comparison of 1G and 2G coils in both arrangements have clearly identified 2G coils as less sensitive to the placement variations in the coils stack.
- Comparison of 1G and 2G coils in both arrangements have also clearly identified 1G coils as extremely sensitive to the placement variations in the coils stack.

5.4 Interaction of Armature and HTS field winding

The analysis of the operation and performance of the HTS field winding described so far did not include an interaction of the field winding with the armature winding. Since both arrangements of the HTS field winding have shown sensitivity to magnetic field (self generated), the effects of the armature reaction as a source of external field should not be neglected.

Two parameters have been used to describe this interaction: the armature reaction or I_a in Amps and the angle between the armature winding and the field winding magnetic axis or γ in degrees. An additional parameter was used during the experiments, ϕ, which afterwards was used to derive γ. In the Locked Armature experiment, it was not possible to precisely align the magnetic axis of the phase A and the field winding. Instead, arbitrarily position of the armature was chosen for which ϕ=0°. The correlation between γ and the ϕ will be derived later on when the measured torque as a function of ϕ is examined.

To get a proper scaling between the amplitude of the three phase armature reaction, I_{a3ph} and the armature reaction generated with two phases running with I_a and -I_a, the correction coefficient of $\sqrt{3}/2$ should be applied. The rated amplitude of the phase armature current is $I_{a3ph} = \sqrt{2}{\cdot}23.5$ A= 33.2 A, which means that the value of I_a corresponding to the rated armature reaction (maximal value) is 28.8 A. During the Locked Armature experiments, the armature reaction had to be restricted to $I_a \leq 20$ A in order to limit the temperature rise of the winding and also due to the voltage limit of the DC power supply which was used.

During the experiments with locked armature winding, described in the Sec.4.7, the voltages of the HTS field winding have been monitored as a function of I_a and ϕ. As *Coil#*3 is the 'bottleneck' of the field winding with lowest I_c in both arrangements, the results shown will mainly focus on *Coil#*3.

5.4.1 $E_{Coil\#3}$ for Arr2 Locked Armature experiment

The electrical field of *Coil#*3 in Arr2 shown in Fig.5.15, Fig.5.16 and Fig.5.17 are presented as a function of the armature reaction at X axis and the ϕ at the Y axis.

For the field winding in Arr2 with current of 40 A, the electric field is presented as a 3D surface in Fig.5.15. The voltage is well below E_0 for all angles and all armature

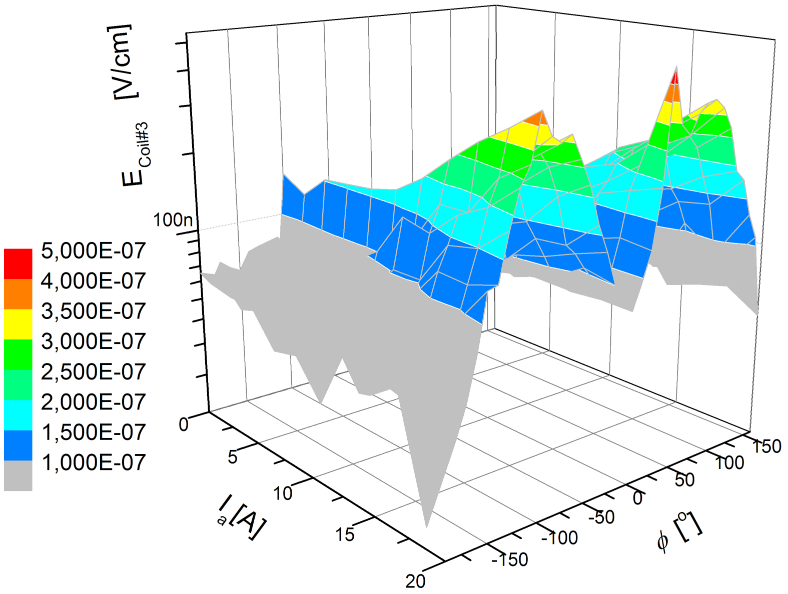

Figure 5.15: *Coil#3* **in Arr2 with I_{coil}=40 A** - The HTS field winding in Arr2 is connected in series and is supplied with I_{coil}=40 A. The average electric field of the coil is at the Z axis with color legend corresponding to electric field levels. The armature reaction, I_a, with values from 0 A – 20 A is at the X axis and the span of 360° of the ϕ at Y axis.

reactions and because the measured voltage was very small, a certain level of noise is present in the graph. We can see from Fig.5.16, where the field current is 45 A, that the electric field of *Coil#3* reaches $E_0 = 100\mu\text{V/m}$ for I_a =20 A for angles ϕ ~85° and ϕ ~-95° while for all other angles it is well below E_0. This clearly indicates that the performance of the HTS field winding will be a function of the armature reaction.

The case where the HTS field winding operates with 50 A in Arr2 is presented in Fig.5.17. The electric field of the coil has the same tendency of having the maximal value at the ϕ ~85° and ϕ ~-95°. The level of electric field indicates that with 50 A, the HTS field winding almost always operates with current above I_c, except for the ϕ ~-185°. For this value, we can observe that the electric field that was initially above E_0 for I_a=0 A, but is below E_0 with increasing armature reaction. These results could be used to define the critical current of the HTS field winding, defined as the field winding current for which the nominal armature reaction at any angular displacement would not cause the coil voltage to become higher than $E_0 L_{coil}$,which would present

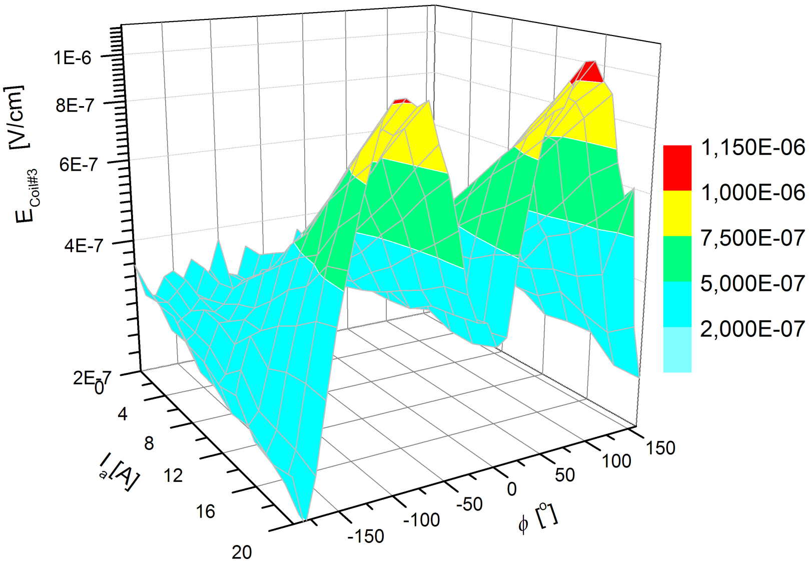

Figure 5.16: ***Coil*#3 in Arr2 with I_{coil}=45 A** - The HTS field winding in Arr2 is connected in series and is supplied with I_{coil}=45 A. The average electric field of the coil is at the Z axis with color legend corresponding to electric field levels. The armature reaction, I_a, with values from 0 A – 20 A is at the X axis and the span of 360° of the ϕ at Y axis.

the maximal operating current of the field winding. In order to define this current, the presented result will need to be extrapolated to I_a=28.8 A. None of the operation safety margin is considered here since we are interested in critical parameters. However since the armature current of an electric machine during its lifetime will have excursions to the higher values than nominal (short time overload and fault conditions), the process of defining the maximal HTS current loading will need to take that into account too.

The same experiment was performed for the field winding connected in Arr1 where *Coil*#3 showed similar tendencies. The results are included in the Appendix.**??**

5.4.2 Torque-angle correlation

As the basis of electric machine operation is an interaction between two magnetic fields, consequently an electromagnetic torque developed by this interaction is an important parameter for the machine analysis. Electromagnetic torque acting on the field winding

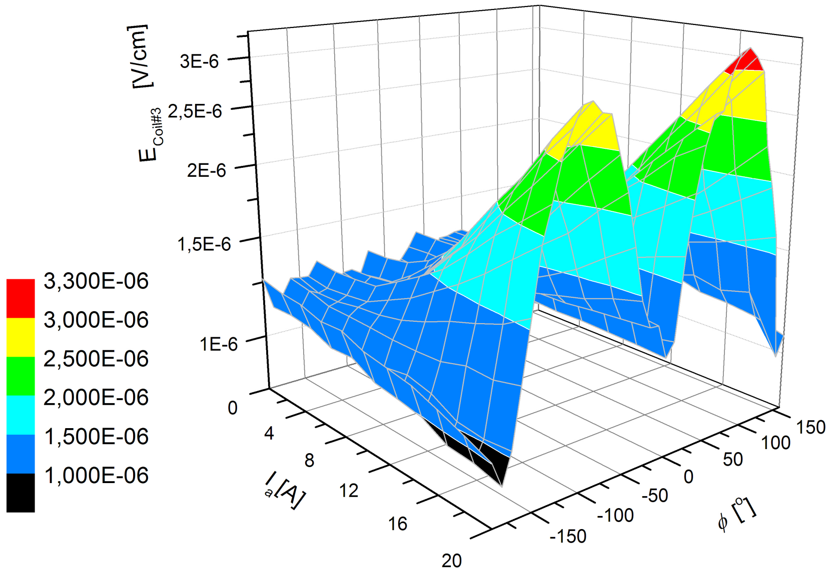

Figure 5.17: ***Coil*#3 in Arr2 with I_{coil}=50A** - The HTS field winding in Arr2 is connected in series and is supplied with I_{coil}=50A.

was measured during experiments with the Locked Armature. The results for the case when the field winding is in Arr2-c where four coils (*Coil*#3, *Coil*#2, *Coil*#5, *Coil*#6) are supplied with 50A and two damaged coils (*Coil*#7, *Coil*#8) supplied with 10A, is presented in Fig.5.18. More about this operating mode will be discussed in the following section Sec.5.6.2. The torque as a function of the armature reaction and the current of the field winding corresponds closely to the magnetic permeability of the cold steel where the effects of saturation are becoming visible at higher currents. It is also noticeable that the 2^{nd} torque harmonic, ie. reluctance torque, is very weak.

The torque versus angle 2D plot for I_a=20 A is compared to the torque-angle derived with FE simulation corresponding to the same conditions and is shown in Fig.5.19.

The measured results are in good agreement with the FE simulation. For the presented case, the torque was fitted with the sum of harmonic functions, presented in 5.3, where the main harmonic $T_{1^{st}}$=49.54 Nm and the reluctance torque $T_{2^{nd}}$=0.16 Nm for the presented case. The reluctance torque has been estimated by FE model and the value of $T_{2^{nd}} = 4.5$ Nm was observed for no field current (when Steel37 is not saturated) and with $I_a = 20$ A. Its value decreased rapidly with the increase of the

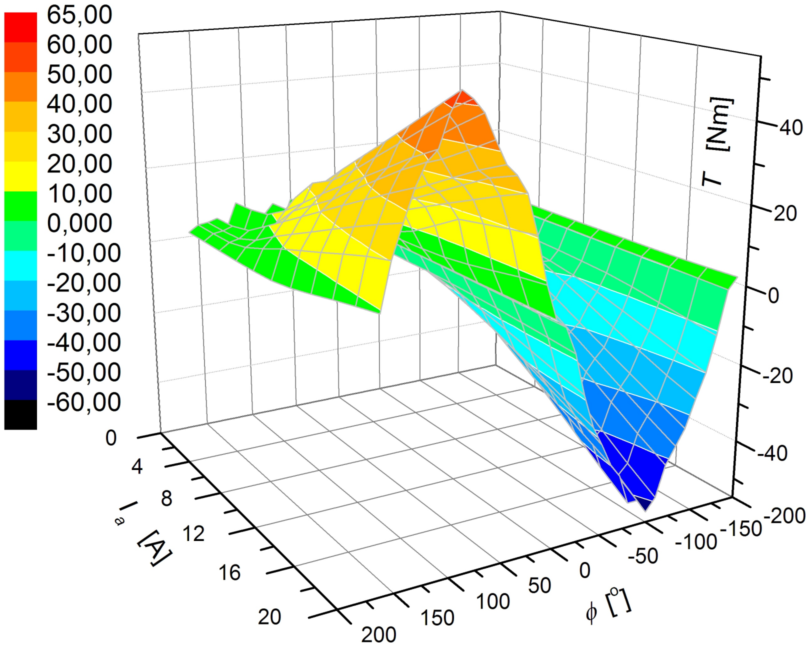

Figure 5.18: The torque $T(\phi, I_a)$ for Arr2-c with $I_{Coil} = 50A$ - The HTS field winding in Arr2-c was supplied with $50A$

MMF of the field winding since the cold steel started to saturate, resulting in 0.16 Nm for the above presented case.

$$T(\gamma) = T_{1^{st}} sin(\gamma) + T_{2^{nd}} sin(2\gamma) \tag{5.3}$$

From Fig.5.19 the correlation can be found between the mechanical angle, ϕ and the angle between magnetic axis of the armature winding and the field winding, γ. We will adopt the convention that γ is zero when the armature magnetic axis is collinear to the magnetic axis of the field winding (d-axis), as illustrated in the Fig.5.21. Consequently, at γ=0° the torque will be zero as well. After including $\gamma = \phi + 5°$, the measured and simulated results will become angularly synchronized as presented in Fig.5.19.

The linear approximation was made to derive the relation between the torque, MMF of the field winding and the armature reaction at the ϕ=90°. The equation used for the fit is defined with 5.4 and the performed fit resulted (for the data presented in the 5.20) with the K_T=2.64×10^{-4} NmA^{-2}.

$$T_{1^{st}} = K_T \cdot MMF \cdot I_a \tag{5.4}$$

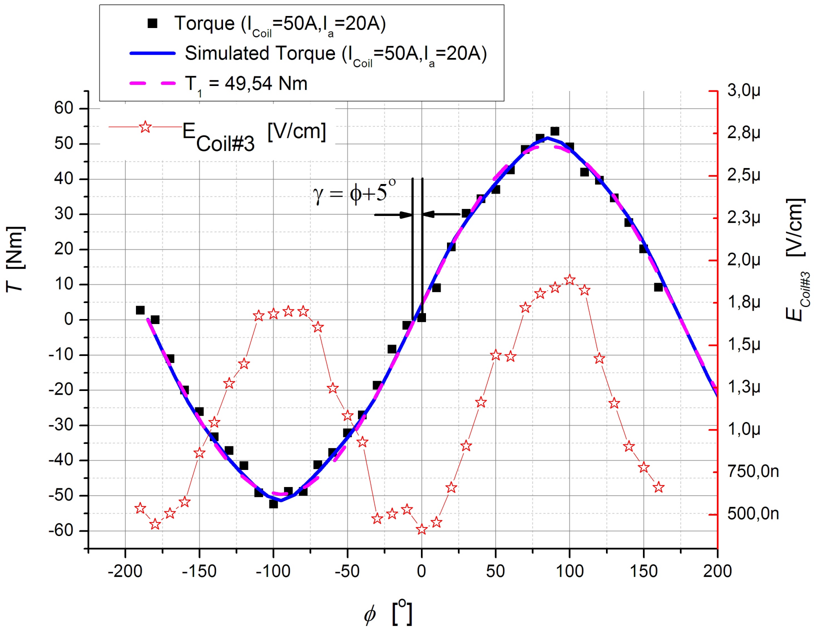

Figure 5.19: Comparison between measured torque and FE simulation. - Comparison between measured torque for the current of 50 A of the HTS field winding in Arr2-c and the corresponding FE simulation of Locked Armature experiment. The figure includes derived first harmonic of the torque for angular shift of $\gamma = \phi + 5°$. The figure also includes the electric field of the $Coil\#3$ during the experiments which allows conclusions on the correlation between the HTS field winding performance and the relative position (instead of absolute expressed with ϕ) of the armature reaction with respect to the HTS field winding.

where MMF the magneto motive force of the field winding and I_a is the value of dc current flowing in two phases.

5.4.3 Locked Armature Experiment - Extrapolation of the results

In order to estimate what would be the maximal operating current of the HTS field winding with the rated armature current, we need to extrapolate recorded results (to the rated or higher values or armature reaction). Considering that (in theory) an armature reaction could be at any angle with respect to the field winding, it would be useful to spend a few words to identify the characteristic operating positions and their implication. Four characteristic cases are illustrated in Fig.5.21.

From the previous section we derived the $\gamma(\phi) = \phi + 5^o$ relation for both arrange-

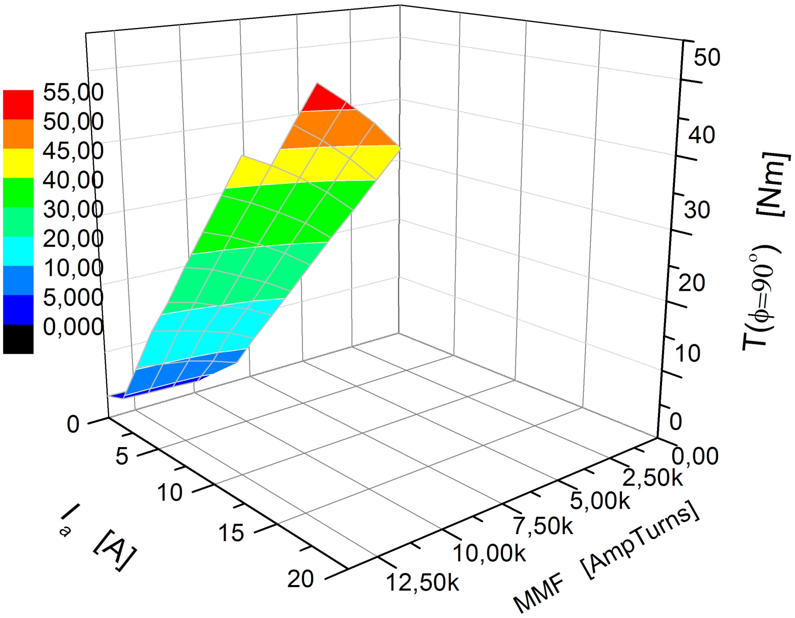

Figure 5.20: The torque $T(MMF, I_a)$ for Arr2-c at ϕ=90° - The $T(I_a, I_{Coil})$ for $35A \leq I_{Coil} \leq 50A$ and $0A \leq I_a \leq 20A$.

ments and thus the electric field graphs presented so far can be related to γ and to the characteristic positions presented in Fig.5.21. Consequently, the angles where armature reaction has the largest impact on the coils are corresponding to the angles where the electromagnetic torque has its extremes, ie. γ=±90° (Fig.5.21b and Fig.5.21c). The slight difference between these two was observed in the electric field of the analyzed coils presented in Fig.5.19 but this was deemed insignificant to account for any of the physical aspects which are in the focus.

The other two characteristic positions presented in Fig.5.21 where the MMF of the armature and the field winding are collinear, ie. for γ=0 and γ=180°, would correspond to the sections with lowest impact of armature reaction on the electric field of analyzed coils. Between these two positions considerable difference in measured electric field can be observed. The case where the electric field of the coils is slightly increasing with an increase in armature reaction would correspond to Fig.5.21a, while if the position of the MMF are as in Fig.5.21d, the electric field of the coils will experience slight decline with an increase in armature reaction. As these characteristic positions are corresponding to specific load regimes in the machine (as boundary cases defined in Fig.5.21), it is

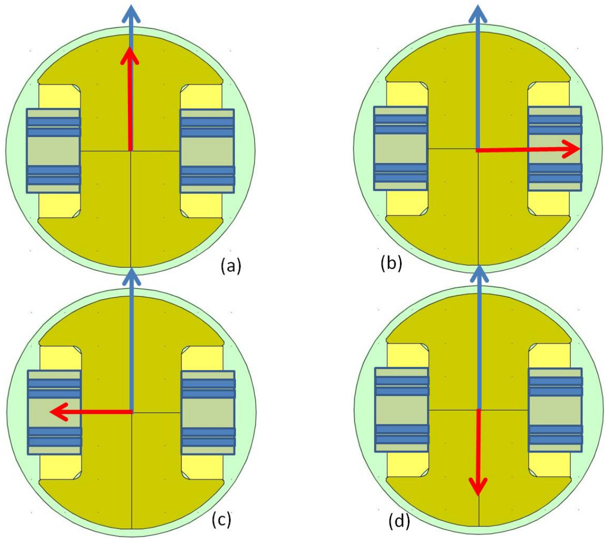

Figure 5.21: Four (boundary) cases of armature and field winding interaction. - This figure presents four characteristic operating regimes for an electric machine. These are identified as positions of interest for the analysis of field winding (the blue arrow) and armature (the red arrow)interaction with respect to the HTS field winding performance. (a) The γ=0°, which corresponds to the reactive (capacitive for generators or inductive for motors) load; (b) γ=90°, which corresponds to the maximal active load; (c) γ=180°, which corresponds to the maximal active (breaking) load; (c) γ=-90°, which corresponds to the reactive (capacitive for motors or inductive for generators) load.

important to understand the implications that each load would have on the HTS field winding as we proceed to extrapolate and define the operating window of the same field winding.

From Sec.5.4.1, we can identify ϕ=85° as the one where the coil ($Coil\#3$) exhibits highest voltages. Thus, recorded data for voltage of $Coil\#3$ at ϕ=85° (corresponding to γ=90°) is presented as a 3D graph where the coil voltage is presented as a function of the current in the field winding and the armature reaction, shown in Fig.5.22. By identifying electric field level equal to E_0, the critical current of the coil (and thus field winding too) can be expressed as function of armature reaction. Hence, in order to derive this function, first a surface fit needs to be performed for the surface presented in Fig.5.22. Since the electric field of the coil follows the power law regardless if it is the armature current or coil current that is increasing, this dependence would be a linear function of both I_a and I_{coil} if it is presented as a *log* plot. This is a convenient way

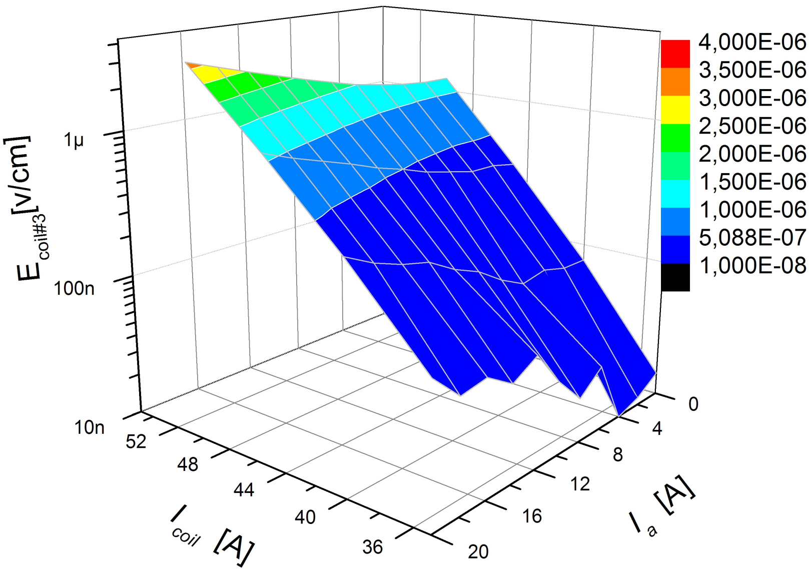

Figure 5.22: Electric field of $Coil\#3$ for ϕ=85° - The figure is presenting the HTS field winding in Arr2 where the level of the electric field can be identified with the color legend. The particular cases have been presented: where the armature reaction has significant impact on the I_c of the coils, i.e. ϕ=85°.

to express the tendency of the electric field of the coil and hence it was adopted here. The equation for the plane which the data were fitted to had the form presented in 5.5.

$$Log(E_{Coil\#3}) = Log(E_{offset}) + a \cdot I_{coil} + b \cdot I_a \tag{5.5}$$

The coefficients for the fitted plane are as follows $Log(E_{offset})$=-11.92, a=0.1176, b=0.0327. Next, by finding the cross between planes defined with 5.5 and $E_{Coil\#3} = E_0$ will finally result in $I_c(I_a, \gamma = 90°)$ of the HTS field winding. The derived critical current of the field winding is shown in Fig.5.24 together with recorded data (used for extrapolation). For the rated armature current, I_a=28.8 A, the estimate of the critical current of the field winding would be $I_c(I_a = 28.8A, \gamma = 90°)$= 42.3 A, as illustrated with 5.6. This represents approximately 15% reduction of the field winding MMF current capacity compared with no load (I_a=0 A).

$$I_c(I_a, \gamma = 90°) = \frac{1}{a}(Log(E_{offset}) - Log(E_0)) - \frac{b}{a} \cdot I_a = 50.34 - 0.28 \cdot I_a \tag{5.6}$$

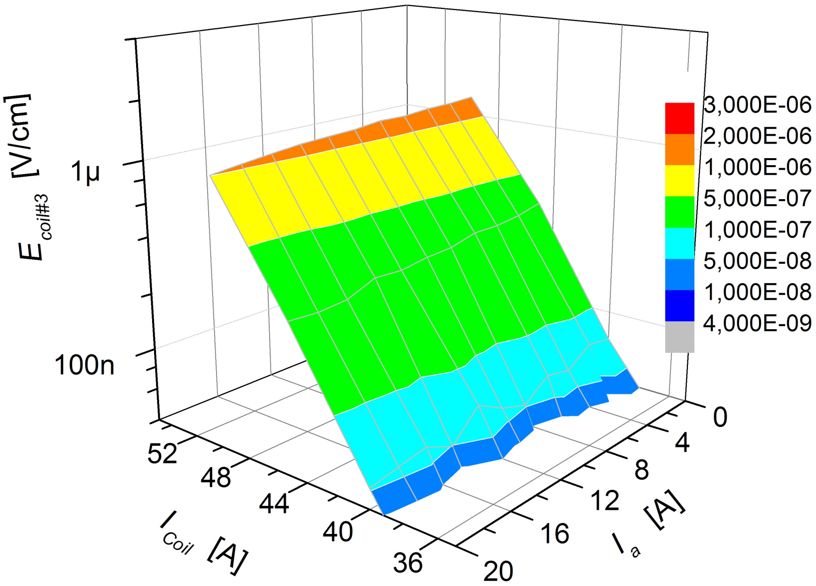

Figure 5.23: Electric field of *Coil*#3 **for** ϕ**=-185°** - The figure is presenting the HTS field winding in Arr2 where the level of the electric field can be identified with the color legend. The particular cases have been presented: where the armature reaction has small impact on the I_c of the coils, i.e. ϕ=-185° (γ=90°).

At the other hand, electric field of the coil for ϕ=-185° (or γ=-180° which is illustrated by Fig.5.21d) as a function of both the field winding current and the armature reaction is presented in Fig.5.23. The same procedure was carried out for this case (surface fit and the cross between the fit and E_0) and the resulting extrapolation of the critical current, $I_c(I_a, \phi = -185°)$, is also presented in Fig.5.24. Thus, the HTS field winding current $I_c(I_a = 28.8A, \gamma = -180°)$=50 A at ϕ=-185° would correspond to the critical current at rated armature reaction, as expressed with

$$I_c(I_a, \gamma = -180°) = \frac{1}{a}(Log(E_{offset}) - Log(E_0)) - \frac{b}{a} \cdot I_a = 49.15 + 0.0197 \cdot I_a \quad (5.7)$$

The fits and recorded data presented in Fig.5.24 are not perfectly aligned. Performed fits were made to be a conservative prediction of I_c for the HTS field winding. Furthermore, this extrapolation did not include effects of additional saturation of magnetic teeth and pole shoes due to the higher armature current. However, results from FE simulations have confirmed that the flux of *Coil*#3 (parallel and perpendicular), was in fact a linear function of armature current including rated armature reaction.

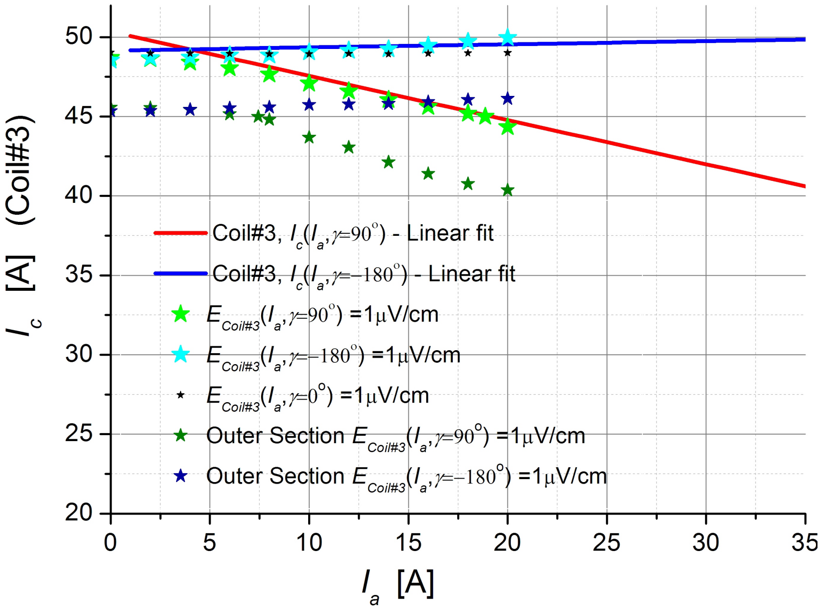

Figure 5.24: The I_c of $Coil\#3$ as a function of the armature reaction for Arr2. - The plot contains data from experiments, shown by a data markers, and extrapolation lines. The extrapolation was performed for ϕ=85° (γ=90°) and ϕ=-185° (γ=-180°). The experimental data include also ϕ=-5° (γ=0°).

$$I_c(I_a,\gamma) = \frac{I_c^q(I_q) + I_c^d(I_d)}{2} + \frac{I_c^d(I_d) - I_c^q(I_q)}{2} cos(2\gamma) \tag{5.8}$$

The $I_{coil} = I_c(I_a, \gamma = 90)$ represents the maximal value of the field current when the armature reaction is in the q axis while $I_{coil} = I_c(I_a, \gamma = 180)$ represents the maximal value of the field current when the armature reaction is in the d axis. It is also true that $I_c(I_a, \gamma = 180°) \geq I_c(I_a, \gamma = 90°)$. Hence, a second harmonic function expressed in 5.8 can be used as a first approximation for $I_c(I_a, \gamma)$ instead of deriving full angular dependence.

If $I_c(I_a, \gamma = 90°)$ is named I_c^q and $I_c(I_a, \gamma = 180°)$ is named I_c^d, since each are caused by the armature current in the corresponding axis, the expression 5.8 can be used to define the critical current as a function of the armature reaction and the load angle. To verify this approximation for all angles, the expression 5.8 was compared to the experimental data for I_a=16 A. Both are presented in Fig.5.25, where it can be seen that approximation and experimental data are in good agreement.

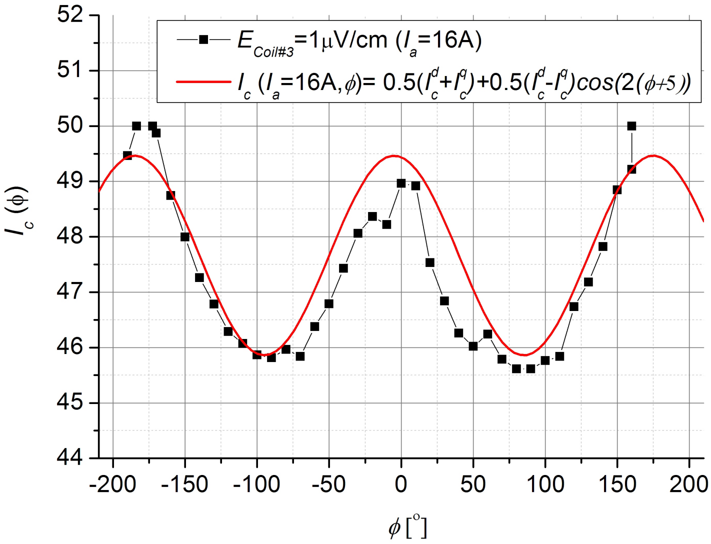

Figure 5.25: Comparison of $I_c(I_a, \phi)$ from experiments and second harmonic approximation for I_a=16 A - Experimental critical current for Ia=16 A was derived from the condition $E_{Coil\#3}$=1 μV/cm while second harmonic approximation is plotted with the help of 5.6, 5.7 and 5.8 and for I_a=16 A

5.4.4 Performance verification - *Coil*#3 sections

So far, a low level of discrepancy, if any, has been observed between inner and outer sections of the turns in individual IV curves of the coils. Yet, the armature reaction can have a prevailing influence on the HTS coil performance, as seen in previous sections. Consequentially, sections of the critical coils should be investigated for Locked Armature experiments as well in order to confirm the derived critical parameters of the HTS field winding. The illustration in Fig.5.26 shows the nature of the change in more detail.

The tendency of the electric field of sections of *Coil*#3 have been presented as a ratio of the electric field for the outer and for the inner section and are presented for the case when the field winding was supplied with 45A in Arr2. The ratio, presented in Fig.5.27, which for this case have values between 1.7 and 2.1, is a function of ϕ too. For the outer section of the coil *Coil*#3, the electric field profile is presented in Fig.5.28. Comparing this profile to Fig.5.16, it is obvious that the outer section has a much larger portion of the electric field above E_0. Consequently, in order to take into account reduced capacity of the outer section of the coil, the adjustment of the extrapolation procedure from Sec.5.4.3 is in order. After analysis of the data from the

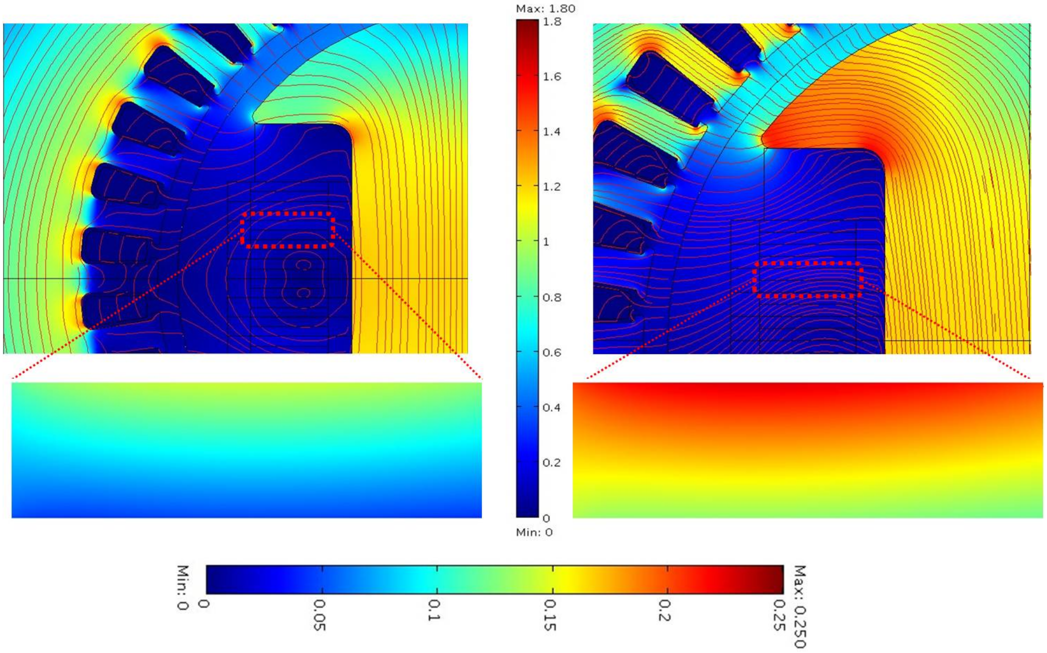

Figure 5.26: The FE simulation of Locked Armature Experiment for γ=90°, $I_{Coil\#3}$= I_{Coil}= 40 A, and I_a=0.0 A and I_a=30 A - This figure represents the FE simulations corresponding to the Locked Armature Experiment condition. The plot of magnetic flux density for I_a=0 A is presented on the left side of the figure while for I_a=30 A is at the right side. The vertical color legend with maximum of 1.80 T at dark red and 0.0 T at dark blue end is common for both flux plots. Additional graphs of the perpendicular magnetic flux density at $Coil\#3$ have been enlarged and placed below corresponding plots as the dashed red lines suggests. These plots share a common horizontal color legend with 0.25 T as a maximum at the dark red and 0.0 T as a minimum at the dark blue end. Perpendicular flux will increase linearly with the increase if armature reaction at γ=90°. The flux lines have been included as well.

outer section with respect to the extrapolation prediction, the reduction of ∼4 A was observed in I_c, which means that revised extrapolation lines would be paralleled to the previously derived extrapolation lines (vertically migrated down). Only experimental data (not corrected prediction linear fits for the outer section of $Coil\#3$) are presented in Fig.5.24 in order to illustrate the effect of sections current rating.

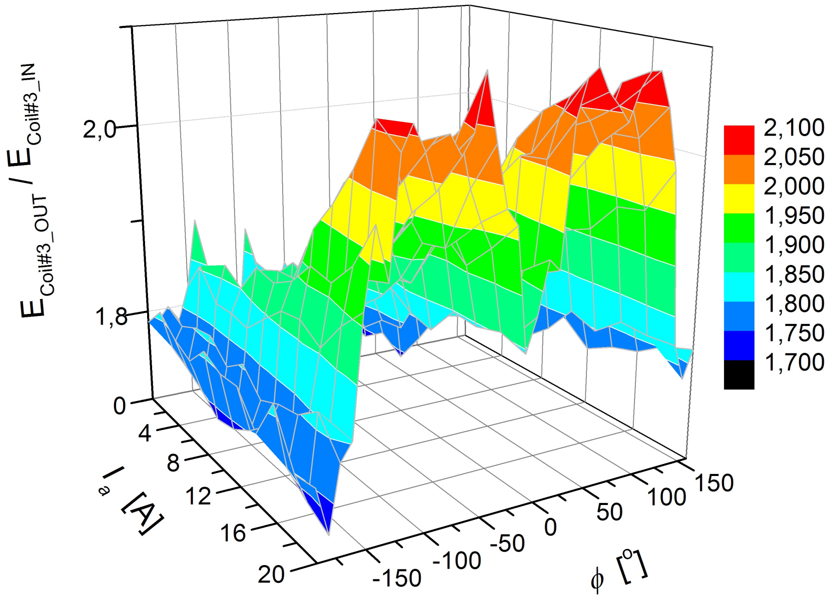

Figure 5.27: $E_{Coil\#3-OUT}/E_{Coil\#3-IN}$ - The figure illustrates the tendency of the ratio of electric fields of the outer and the inner section of Coil#3 for the field winding in Arr2. The ratio indicates that the outer section of the coil has higher voltage drop and is exposed to a higher value of the perpendicular magnetic flux than the inner section. This is in line with the simulation results in Fig.5.26.

5.4.5 Summary for HTS field winding - armature interaction

- The armature reaction does have significant influence on the HTS performance.

- The influence of the armature reaction on HTS field winding depend on the angle between a magnetic axis of the armature winding and the HTS winding.

- In both arrangements *Coil#3* was the coil with lowest I_c, which implies that conclusions derived regarding coil placement recommendations will not be affected by the armature current.

- Extrapolation of recorded results was performed for the HTS field winding in Arr2 and values of I_c^d=49.95 A and I_c^q=42.3 A were found for rated armature reaction.

- A second harmonic approximation of maximal field current as a function of γ (or ϕ) was proposed: $I_c(I_a, \gamma) = 0.5(I_c^d + I_c^q) + 0.5(I_c^d - I_c^q)cos(2\gamma)$ and compared

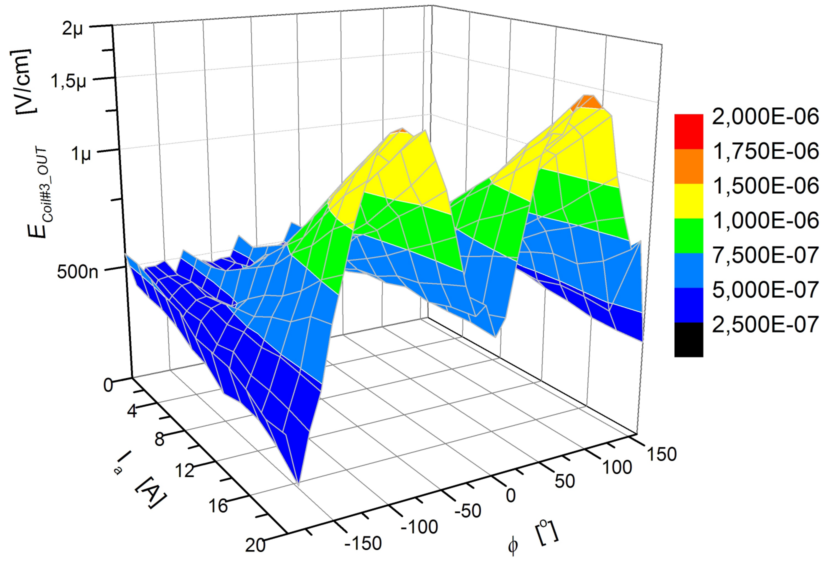

Figure 5.28: $E_{Coil\#3-OUT}$ - The figure indicates the impact of the armature reaction, both intensity and angular displacement, on the discrepancy in the performance of the coil turns. The I_a=30A which is slightly higher than the rated armature reaction.

to the experimental data. The approximation is in the good agreement with experimental data.

- Electromagnetic torque was analyzed for one configuration of the field winding. A small value of the reluctant torque was observed in recorded results (which is due to saturation of the cold steel). A surface fit of the electromagnetic torque resulted with $T_{1^{st}}$[Nm]=2.64 $\times 10^{-4}$ [NmA^{-}2] × MMF [AmpTurns] × I_a [A], where MMF is the magneto motive force of HTS field winding and I_a is armature current (two phase, dc as in the experiments) in q axis.

- The discrepancy in performance of the turns in $Coil\#3$ is a function of the armature reaction. Approximately 4 A higher I_c was observed for the inner section of $Coil\#3$.

5.5 Armature driven HTS supply - General recommendation

As seen so far, magnetic anisotropy of the HTS field winding has caused different responses of the HTS field winding to the armature reaction at different angles. Thus, the operation conditions could be formulated for both an armature winding and a field winding of an HTS machine, such that the maximized power output is maintained (assuming these are in controllable configuration). The boundary conditions for the maximal operating current of the HTS field winding have been defined as functions of an armature reaction, ie. $I_c(I_d, I_q)$.

The conventional design of the HTS machine would specify the maximal value of MMF of the field winding which corresponds to the rated (or maximal taking into account safety margin) armature reaction and its impact on the I_c of the field winding. From Sec.5.4.3, this would correspond to the $I_{Coil} \leq I_c^q$= 42.3 A for any armature current (less or equal to rated value). If instead, the field current is adjusted to follow the $I_c(I_d, I_q)$[1], higher MMF would become available for lower values of armature current. This in turns means that same power output (torque) can be achieved with a lower value of armature current which in turns will result in lower loss in the armature winding and better partial load efficiency of the machine.

For the Superwind machine, the difference between maximal current of the field winding with rated armature current in the q axis and with no armature current in q axis is 50 A/42 A$\sim$1.19. If the machine was designed in a conventional way, the maximal field current corresponding to the rated torque would be I_{Coil} $\leq$42 A or 40%–80% of this value if the safety margin is included. For a 50% loaded machine (half of the rated torque at rated speed, ie.τ=0.5 p.u.), the armature current in q axis would need to be half of the rated value, ie. τ= MMF $\times$ I_q = 1 p.u.$\times$ 0.5 p.u. = 0.5 p.u. Now, with the proposed method, since the armature current is lower than the nominal value, in the case of Superwind machine, a 10% higher field current can be allowed.This will in turn reduces I_q from 0.5 p.u. to 0.45 p.u. which would decrease armature loss by $\sim$18% compared to the previous example. Thus, if an HTS machine is to operate substantial time in partial load (which is the case for wind turbine generators), a significant savings

---

[1] Note: Described control concept for a field winding of an HTS machine is pending for a patent application with Dr.Bogi B. Jensen and Nenad Mijatovic listed as inventors.

in the both energy and cost can be achieved through proposed control strategy. On the other hand, the dynamic changes in the field current of the HTS field winding will generate ac loss in the winding. This loss and the time constant of the field winding (inductance and voltage insulation) will be limiting factors for the dynamics (how fast the tracking of I_q can be) of the proposed control of the field winding current. Hence, a balance between these will need to be obtained.

5.6 Boosting an HTS field winding's performance

In this section two methods for increase of maximal operating MMF of the HTS field winding are proposed. The first method is based on the difference between the HTS coils and their current capacity. This method suggests multiple power supplies as a way of achieving higher values of MMF from an HTS winding. The second method proposes the placement strategy for 2G coils and it presents the analyses of its impact on the neighboring coils.

5.6.1 Multiple current supplies

It is clear from the figures Fig.5.7 and Fig.5.8 that the inner coils, namely $Coil\#2$ and $Coil\#6$ in Arr1 and $Coil\#2$ and $Coil\#5$ in Arr2 are substantially far from critical currents in the series connected field winding. If each coil is supplied from an independent power supply, the current in the coil could be set to a value that is optimal with respect to a number of objectives, where maximizing the MMF of the HTS field winding would be an obvious one.

If the HTS coils in the HTS winding are allowed to carry different currents, the same MMF can be achieved with a substantially lower amount of HTS tape (133) where a 50% reduction was reported as a theoretical maximum that could be achieved for 2G coils at 20 K. Several examples of the multiple power supplies have been experimentally tested in order to examine the potential of this method. As far as to the author's knowledge, this approach is novel to an HTS machine design and it was not suggested in any of the published HTS machine designs. With four Hewlett Packard DC power supplies in Arr1 or six in Arr2, the setup allowed each coil to have an independent current supply. Thus, 5.2 will become 5.9

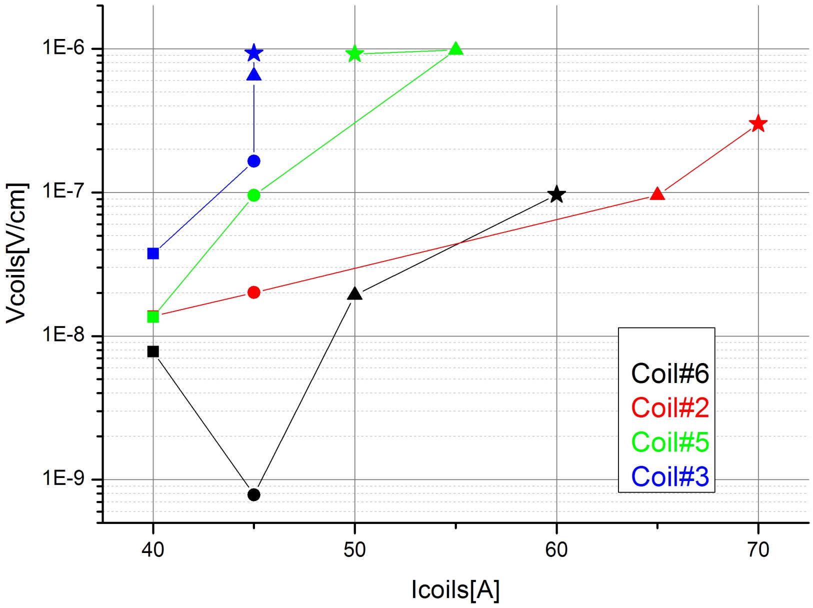

Figure 5.29: The trace of voltages of the coils with four power supplies while the HTS field winding is in Arr1. - Coil current in the plot are: square - $[Coil\#2-40A; Coil\#3-40A; Coil\#5-40A; Coil\#6-40A]$, circle - $[Coil\#2-45A; Coil\#3-45A; Coil\#5-45A; Coil\#6-45A]$, triangle - $[Coil\#2-65A; Coil\#3-45A; Coil\#5-55A; Coil\#6-50A]$ star - $[Coil\#2-70A; Coil\#3-45A; Coil\#5-50A; Coil\#6-60A]$

$$\forall \left(\frac{U^i_{coil}}{L^i_{coil}} \right) \leq E_0 \tag{5.9}$$

where the coil index i takes values from the coil ID array for coils present in the field winding. For Arr1 the index i would take values from the array of the coils ID present in the winding, i.e $[Coil\#3, Coil\#2, Coil\#5, Coil\#6]$. The current limit for HTS winding in the Arr1 connected in series is I_c= 52 A (set by $Coil\#3$). Any additional increase in the current of any other coil would cause exponential voltage increase of $Coil\#3$ due to increase in the perpendicular flux. Setting the current of $Coil\#3$ to some lower value, for example 45 A, allows higher flux density $Coil\#3$ is exposed to and thus an increases in the total MMF. To demonstrate the potential of the multiple power supplies, two sets of coil currents have been found to satisfy the condition expressed with 5.9 and are illustrated in Fig.5.29, where electric field of each coil is presented for the corresponding current. The points with same data markers are identifying one combination of composition of coils currents. Because the number of sources is not small (four), and due to the time constraints only several operating points with higher MMF have been identified, hence the degree of the improvement may be even higher than presented here but that would call for extensive experiments and purpose built search algorithm in LabView. Nevertheless, even for presented cases, having the coils carrying currents close to their individual I_c, the total MMF of the HTS field winding in Arr1 was increased by 12% compared to the series connected HTS coils with current of 50 A. The coil exhibiting the highest increase in operating current is *Coil*#2 with 40% higher current compared to the series connected HTS coils.

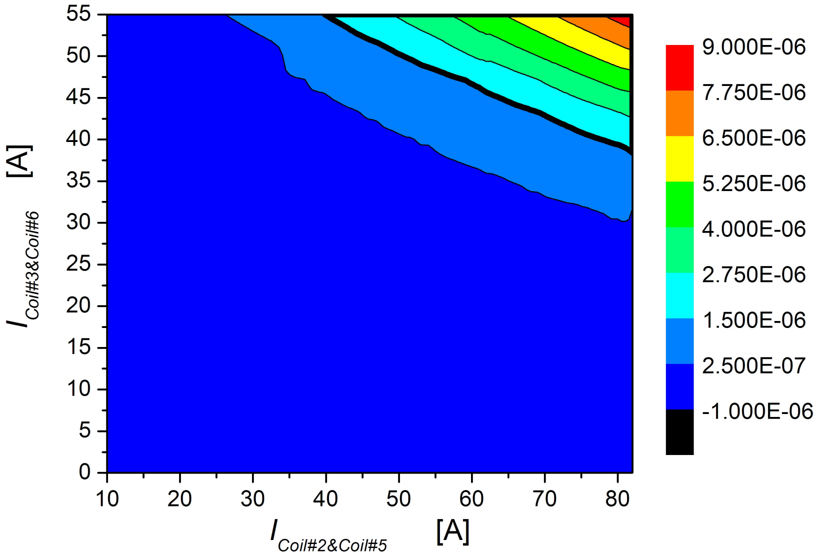

Figure 5.30: *Coil*#3 - This figure presents the I_c contours for *Coil*#3 and *Coil*#5. Two power supplies have been used, one for each pair, and I_c contours are presented as function of these currents. It can be observed that the inner pair of coils, *Coil*#5 and *Coil*#2, has much higher I_c compared to *Coil*#3 and *Coil*#6.

The question of the system complexity should be raised, since the higher number of current leads or complex low temperature power electronics elements and multi terminal brushless exciters would increase the system complexity. Thus, in the spirit of minimizing the complexity of the proposed system, it is also of interest to investigate how much increase in MMF can be expected from each additional power supply.

In Arr2, two pairs of coils have been connected in series. Two power supplies are used where the first one is connected to the coil pair comprised of *Coil*#3 and *Coil*#6 and the second power supply to the coil pair comprised of *Coil*#2 and *Coil*#5. The

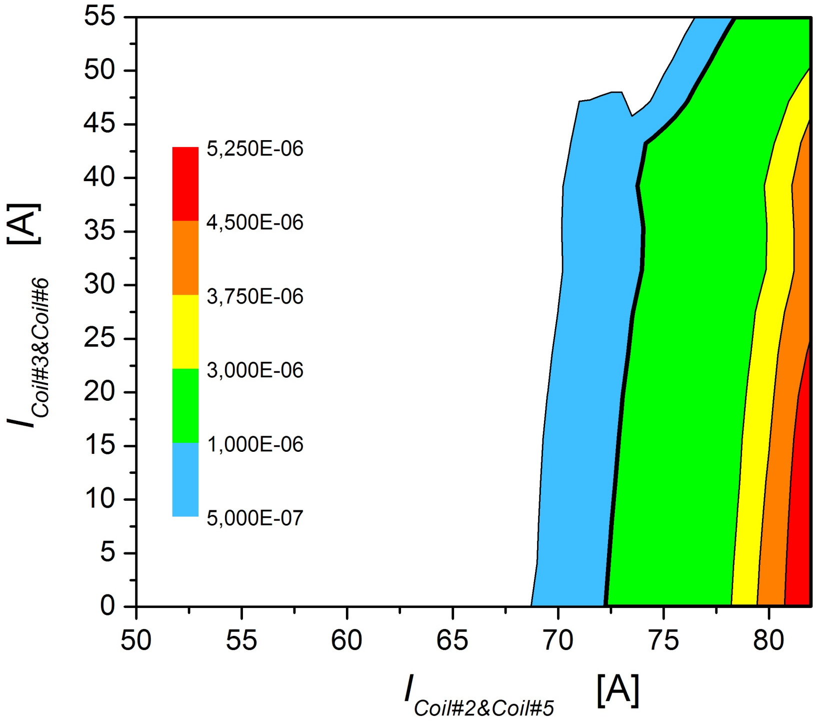

Figure 5.31: *Coil*#5 - This figure presents the I_c contours for *Coil*#3 and *Coil*#5. Two power supplies have been used, one for each pair, and I_c contours are presented as a function of these currents. It can be observed that the inner pair of coils, *Coil*#5 and *Coil*#2, has much higher I_c compared to *Coil*#3 and *Coil*#6.

I_c lines for *Coil*#3 and *Coil*#5 are illustrated in Fig.5.30 and Fig.5.31. For a winding connected into a series, with I_c ~50 A, the MMF of the field winding would be 50 A (48+51+46+56)= 10050 AmpTurns. From Fig.5.30 and Fig.5.31, we can see that if the current of *Coil*#3 is set to be 42 A, *Coil*#5 will be able to carry 72 A. The MMF of the field winding in this case would be 42 A (51+56) +72 A (48+46) =11262 AmpTurns which represents an increase of 12%. The same level of increase was achieved with only two power supplies instead of four as in the previously presented example. This implies that the substantial increase in MMF of the field winding is possible with only one additional power supply.

The cost of the HTS tape is the prevailing cost of the HTS machine and the multiple current supplies approach can be an effective method to reduce the amount of HTS required for a given MMF. However, the implications a multi power supply method would have on the cost of the whole system needs to be evaluated before this method can claim any advantage.

5.6.2 Effective Flux Shielding by HTS coils

From the previous section we have seen that with the introduction of additional power supplies, the performance of the individual HTS coils can be substantially increased which will ultimately result in better utilization of HTS material and could reduce cost for HTS machine. Also, the importance of HTS coils placement was shown in Sec.5.3.4 with the example of $Coil\#6$ and $Coil\#5$ as representatives of 2G and 1G technology in both the field winding configurations.

Coils with defects, $Coil\#7$ and $Coil\#8$, were not in any of the discussions so far, since they would limit the performance of the field winding. Yet, they are capable of carrying low currents and provide some MMF. In Arr2, $Coil\#7$ and $Coil\#8$ have been placed strategically at the outer position in the HTS field winding (close to the pole shoes) as representatives of 2G coils due to its lower magnetic sensitivity, compared to 1G coils. This section explores the additional value of having $Coil\#7$ and $Coil\#8$ active in the field winding, not in the terms of MMF of these coils but their effects on the performance of the HTS field winding in Arr2. Thus, Arr2 with $Coil\#7$ and $Coil\#8$ active will be referred to as Arr2-b and Arr2-c for the case when these coils are fed with 5 A and 10 A respectively.

The electric fields of $Coil\#3$ for I_{Coil}=50A running in Arr2-b and Arr2-c are shown in Fig.5.32a and Fig.5.32b. Comparing these with the case when only four coils are active, presented in Fig.5.17, it is obvious that the percentage of the electric field of $Coil\#3$ that is below E_0 is increased with the increase of the current of $Coil\#7$ and $Coil\#8$. The increase in the critical current of $Coil\#3$ including the influence of armature reaction can be derived following the same procedure presented in Sec.5.4.3. The experimental results for γ=90° are shown in Fig.5.33 where it can be observed that with the increase in current of $Coil\#7$ and $Coil\#8$, the critical current of $Coil\#3$ will increase as well. The maximal increase of 3 A can be observed.

As this increase is mainly due to corrective action of the MMF of $Coil\#7$ and $Coil\#8$ on the stray flux lines seen by $Coil\#3$, this increase is highest for low values of I_a. This is validated with FE simulations as illustrated in Fig.5.34, where the effects of the flux shielding were extrapolated for the case if the defected coils were operational and are able to operate with $\geq$25 A. The FE simulations have confirmed that the

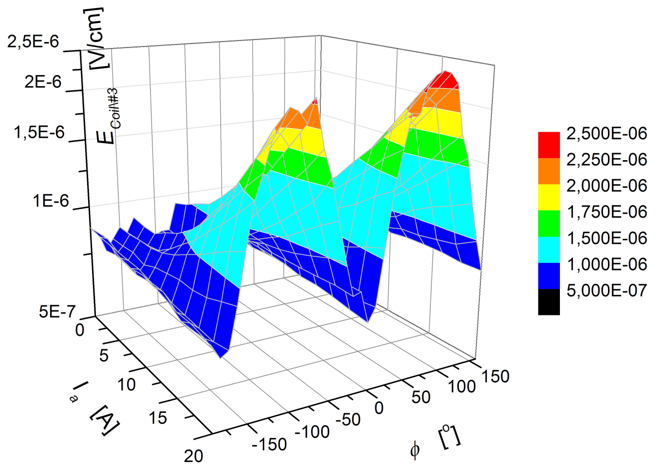

(a) Arr2-b

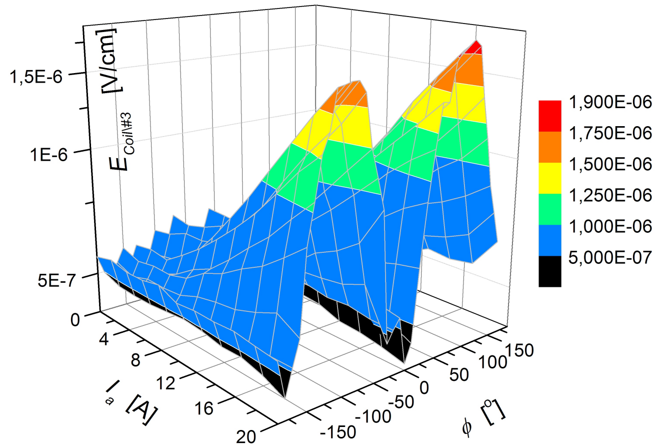

(b) Arr2-c

Figure 5.32: The electric field for $Coil\#3$ - (a)The electric field of $Coil\#3$ for I_{Coil}=50 A for the field winding in Arr2-b. The current of $Coil\#7$ and $Coil\#8$ is 5 A; (b)The electric field of $Coil$ for I_{Coil}=50 A for the field winding in Arr2-c.The current of $Coil\#7$ and $Coil\#8$ is 10 A.

effects of flux shielding are function of the currents of $Coil\#7$ and $Coil\#8$ and that for higher currents, more flux shielding is provided. For the current of 50 A, the magnetic conditions $Coil\#3$ is experiencing are similar to the individual IV experiments which implies that the I_c of $Coil\#3$ could be boosted up to 70 A – 80 A.

Thus, as the portion of total MMF generated by $Coil\#7$ and $Coil\#8$ of the field winding is increasing, so will the perpendicular flux these coils are exposed to. However,

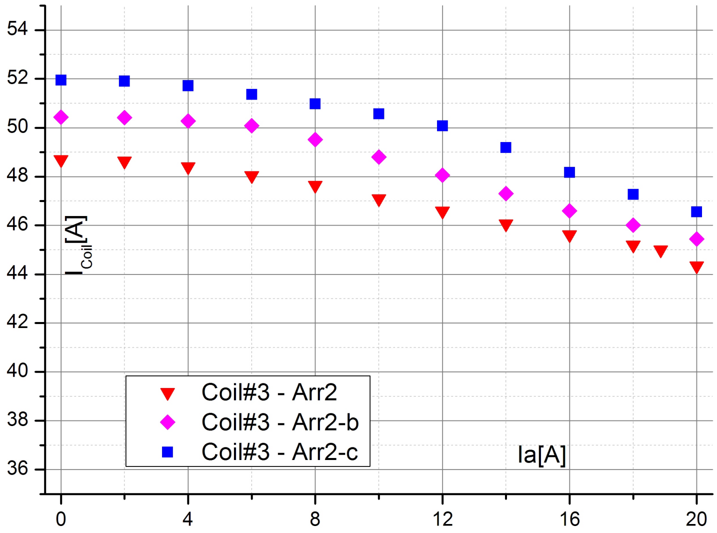

Figure 5.33: The critical current of $Coil\#3$ based on the E_0=1μV/cm criteria, as a function of I_{Coil} and I_a for the field winding in Arr, Arr-b and Arr-c. - This plot illustrates an increase in the critical current of $Coil\#3$ (while part of the series connected field winding) with increase of the current in coils $Coil\#7$ as $Coil\#8$ from 0A to 10A. The discussion was made for γ=90° where the armature reaction impact is the highest.

in two pole machine, if these coils are placed as $Coil\#7$ and $Coil\#8$ are, the perpendicular flux inner coils are exposed to is decreasing correspondingly, ie. flux shielding. The strategic placement of the HTS coils (both 1G and 2G) is of the essence. It is not only that the 2G coils are more suitable to be placed in the field winding where the flux is mostly perpendicular to the turns, but having compact high MMF coils (high engineering current density) placed at outer position will also substantially improve the conditions for the neighboring coils further in the coil stack.

5.6.3 Summary for improving the HTS field winding performance

- By incorporating the multiple current supplies in the design approach of an HTS machine, substantial savings could be achieved where 12% increase in total MMF was observed in the Superwind machine while in the same time the increase in performance of $Coil\#2$ was ~40%.
- A 12% increase in performance of the HTS field winding was observed too for the case of two power supplies in total. Hence, number of additional power supplies

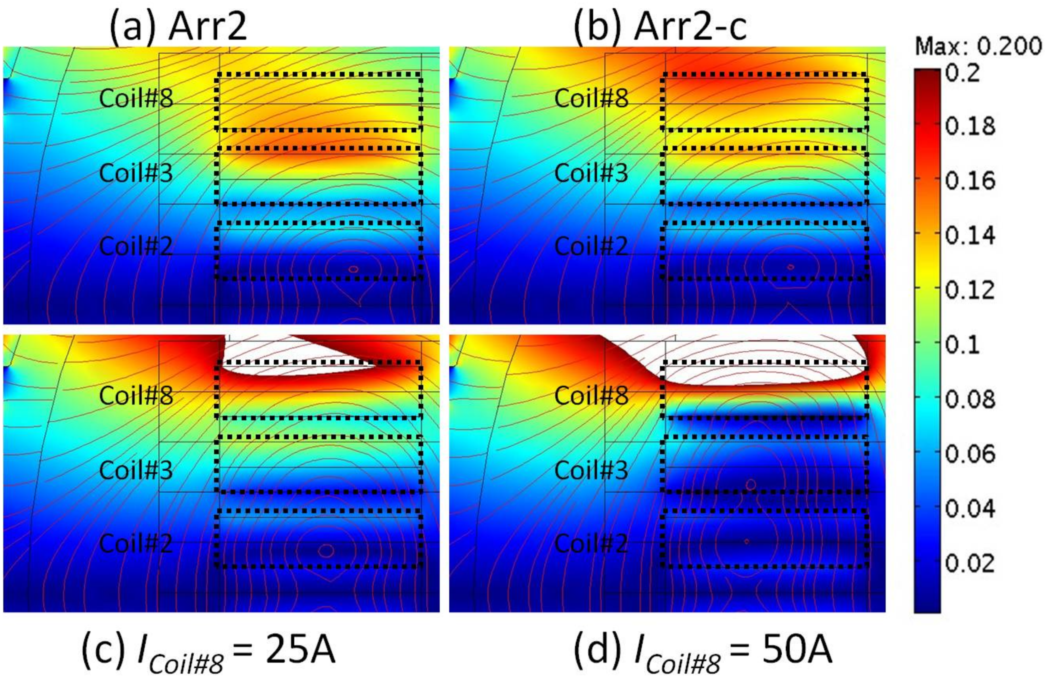

Figure 5.34: The perpendicular flux density plots for various currents of $Coil\#7$ and $Coil\#8$ and for I_a=0A and I_{Coil}=45A. - The color legend is common for all flux plots. Areas with no color (in (c) and (d)) are where the perpendicular flux density is higher than 200 mT. **(a)** Flux plot of the HTS field winding in Arr2, with indicated flux lines. **(b)** Flux plot of the HTS field winding in Arr2-c. With 10A running in $Coil\#7$ and $Coil\#8$, the slight change in the perpendicular flux of the $Coil\#3$ is observed. **(c)** With $25A$ running in $Coil\#7$ and $Coil\#8$, the substantial change in the perpendicular flux of the $Coil\#3$ is observed (50% reduction from Arr2) . **(d)** With $50A$ running in $Coil\#7$ and $Coil\#8$, the perpendicular flux of the $Coil\#3$ is ~50 mT, similar to the magnetic condition for the IV curve of $Coil\#3$.

can be optimized in order to reduce the cost and complexity of proposed approach.

- The placement of 1G and 2G coil proved to be crucial where recommendation to place 2G coils in regions with high perpendicular flux density would result in the HTS field winding with better higher MMF. If instead of $Coil\#3$ in Arr2, the clone of $Coil\#6$ was used, the critical current of the HTS field winding connected into a series would be $ge65$A which is $\sim$ 30% higher than observed in experiments where $Coil\#3$ is the bottleneck.

- An additional benefit of compact MMF (high J_e) of 2G coils is seen in improved magnetic conditions for inner coils.

5.7 The HTS machine parameters and performance

The parameters of the HTS machine will be determined on the basis of experimental data and FE simulation. No load and short circuit experiments were performed for several speeds and operating MMF of the field winding. As the Superwind HTS machine utilizes an armature winding designed for a high speed machine and since the speed of the setup is limited to 400 rpm, the output frequency and induced voltage are expected to be low. Consequently, only loads with low impedance could be used.

5.7.1 Armature No load test

The No-Load voltage was measured in a No-Load test conducted at several speeds (with maximum speed of 312 rpm) and validated via 2D FE simulation. Both measured and simulated results are presented in the Fig.5.35 for the speed of 115 rpm, where as it can be observed, the simulated results for the induced voltage are in good agreement with measurements.

As the magnitude of the induced voltage is a direct indicator of the flux linkage in the machine, the induced voltage in the machine can be correlated to the air gap magnetic flux density. The armature design value for an air gap magnetic flux density could be used as a good reference point for comparing achieved values of the air gap flux density. This is derived as rated armature phase voltage, 400 V, multiplied with the relative speed of the machine in the experiment where the base speed would be the rated synchronous speed of the armature winding, 3000 rpm. The lower value of induced voltage in the phase winding is a consequence of the poor magnetic permeability of the cold steel, Steel37 (for B-H curve see Sec.4.4.3) and large magnetic air gap (10 mm). If instead the high permeability steel is used (for example, M800), both the flux linkage and the HTS current capacity could be boosted on the account of the decrease of the leakage flux of the HTS field winding.

With four HTS coils operated at 77 K for the HTS field winding in Arr1 connected into a series, the highest induced phase voltage was 11.1 V for the speed of 115 rpm. The field current in this case was 50 A. This corresponds to the peak flux density of 0.58 T in the 10 mm air gap. When multiple supplies were used, the maximal value of the

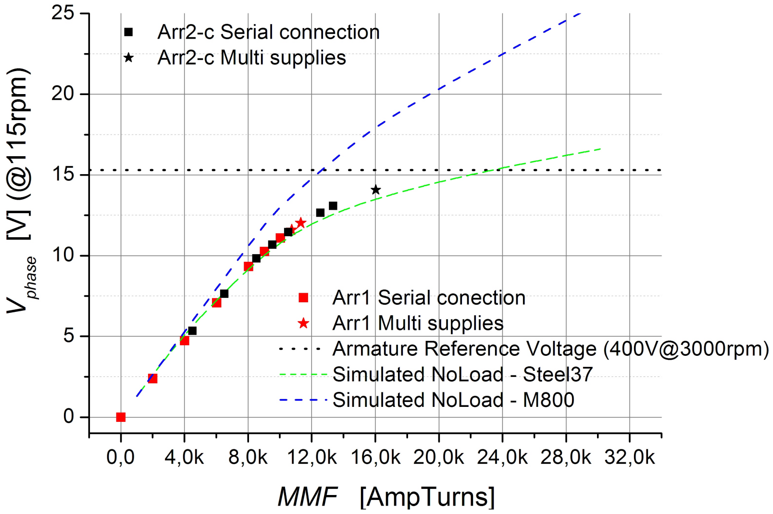

Figure 5.35: The trace of the No-Load voltage for the HTS field winding Arr1 and Arr2. - No Load phase voltage for the HTS field winding Arr1 and Arr2 at 115rpm. Star markers are used in the case when multi power supplies were used. A constant voltage dotted line is illustrating the 115×rpm 400 V / 3000 rpm voltage level. Dashed blue and green lines are representing simulation estimates for No-Load voltage induced if M800 and Steel37 steel are used as a cold steel, respectively.

phase voltage recorded was 12 V with the set of currents for *Coil*#2 with 70 A, *Coil*#3 with 45 A, *Coil*#5 with 50 A and *Coil*#6 with 60 A. This constitutes approximately 78% of the reference voltage (400 V @3000 rpm). In the Arr2-c with multiple power supplies, with the help of MMF from the 2G coils with a defect, the maximal induced No Load voltage was 14 V which constitutes 91% of the reference voltage. Thus, it can be concluded that if *Coil*#7 and *Coil*#8 were operational, the field winding in Arr2 would be able to create the air gap flux density higher than 0.75 T which would induce voltage higher than the rated voltage (15.33 V).

5.7.2 Armature short circuit

The short circuit experiment was performed for several speeds and several values of MMF. Results from the experiments are presented in Fig.5.37. The short circuit characteristics, as expected, are linearly scaled with I_{coil}. FE simulation was carried out for a few selected cases corresponding to the experiments which were compared with experimental data. The measured and the simulated short circuit current waveforms for one of these cases, presented in Fig.5.38, are found to be in good agreement.

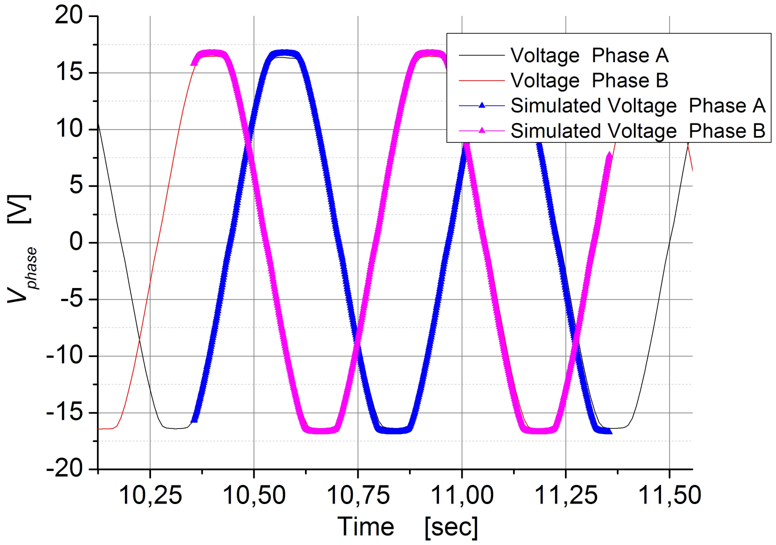

Figure 5.36: The voltage waveform trace for the No Load experiment at 115rpm - The figure illustrates measured phase voltage and the result from a FE simulation corresponding to the No load experiment. The measured (triangles) and simulated (lines) results are in very good agreement.

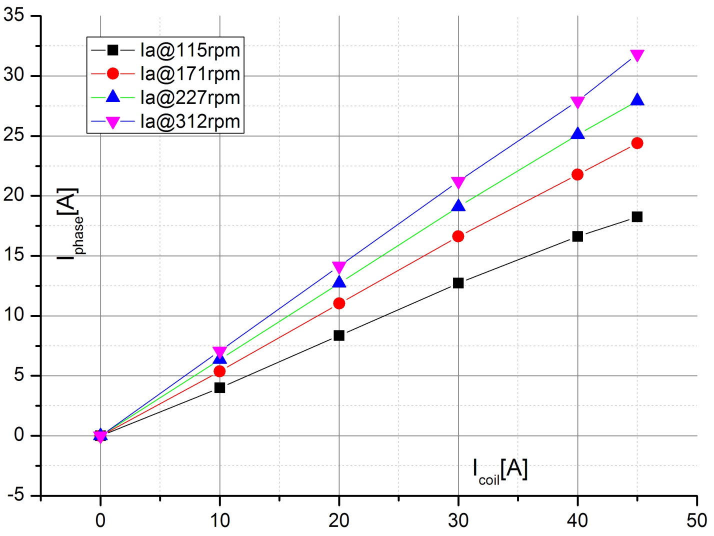

Figure 5.37: Short Circuit Test - The armature winding during the three phase short circuit at several speeds and MMF values. As expected, the short circuit characteristics are linear functions of excitation current.

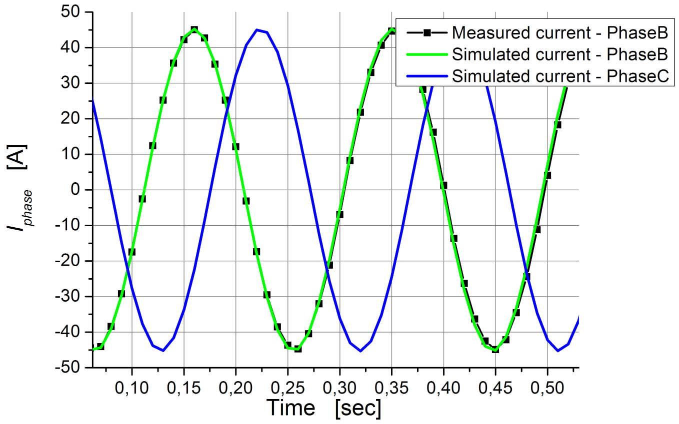

Figure 5.38: The FE simulation of the short circuit experiment. - The figure presents the recorded results and the results from simulation for the short circuit at 312 rpm and for the field current 45 A in Arr2

5.7.3 Estimation of machine parameters

The machine parameters were estimated from a 2D FE model where the self inductance of the phase winding A was found to be

$$L_{aa} = L_{aa0} + L_{aa2} * cos(2\theta) \tag{5.10}$$

$$L_{ab} = -L_{ab0} + L_{ab2} * cos(2\theta - \frac{2\pi}{3}) \tag{5.11}$$

where L_{aa0}= 8×10^{-3}H and $L_{aa2} = 3\times10^{-3}$H. The L_{ab0} was found to be 4×10^{-3}H and $L_{ab0} = L_{ab2}$ which leads to the values of $L_d = 16.5\times10^{-3}$H and L_q= 7.5×10^{-3}H (124) defined by 5.12 and 5.13.

$$L_d = L_{aa0} + L_{ab0} + 3L_{aa2}/2 \tag{5.12}$$

$$L_q = L_{aa0} + L_{ab0} - 3L_{aa2}/2 \tag{5.13}$$

The self and mutual inductances of the phase winding were estimated for a saturated magnetic circuit. Now, we can compare these values with experimental results from no load and short circuit experiments. It is possible to derive the values of L_d and L_q from performed short circuit and no load experiments where the voltage balance equations for d and q axis, written for short circuit (V_d=0V and V_q=0V) are expressed in 5.14 and 5.15

$$R_a I_d = \omega L_q I_q \tag{5.14}$$

$$E_{noload} = R_a I_q + \omega L_d I_d \tag{5.15}$$

where E_{noload} is the no load voltage for given speed and MMF while ω is the angular frequency at given speed. The impedance defined as no-load voltage divided with short circuit current for a salient pole machine can be expressed as 5.16

$$Z = \frac{E_{noload}}{I_{short}} = \frac{R_a^2 + \omega^2 L_d L_q}{\sqrt{R_a^2 + \omega^2 L_q^2}} \tag{5.16}$$

where R_a=0.48Ω is the resistance of the phase winding (@90°C). The values of impedance, Z, derived from the experiments by simple devision of no load voltage and corresponding armature current from short circuit experiment are presented in Fig.**??** for five values of I_{Coil} and four different speeds. Due to the saturation of the cold steel, the values for Z are slightly lower for higher field currents. The curve presented in the figure with the red line is the fit performed for Z($I_{Coil=45A}$) from where the values L_d=23.5×10^{-3}H and L_q =15×10^{-3}H were found. Compared to the FE estimate, the experimentally determined values are higher by ∼7.5×10^{-3}H which is most likely due to the leakage inductance of the end connections of the phase windings (not present in the 2D FE model cannot be used).

If these values for inductances are extrapolated to the rated values for armature winding, (400V, 23.5A, 3000rpm), the inductances expressed in per unit (p.u.) would be: L_d=0.43 p.u. and L_q=0.27 p.u.

5.7.4 Summary for the HTS machine parameters

- The no load voltage test confirmed that with 4 coils in Arr1 and 50 A, the induce voltage was 11,1V which constitutes 72% of reference armature voltage. The air gap flux density across 10 mm magnetic air gap was found to be 0.58 T

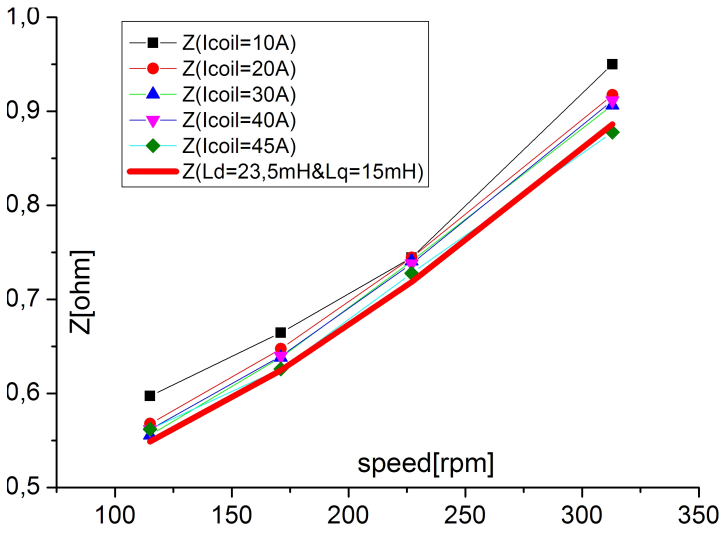

Figure 5.39: Impedance Z calculated for No Load and Short Circuit experiments - The impedance as defined in expression 5.16 for several speeds and values of the field current.

- By operating with multiple current supplies in Arr2-c, the induced voltage was increased up to 91%.
- Parameter analysis of the HTS machine have confirmed the air dominated design due to large magnetic air gap and low permeability of cold steel with low values of L_d and L_q.

——————————— : ——————— end of thesis sub-document ——————— ———————————————

Chapter 6

Conclusion and Future Work

6.1 Conclusion

In the design process of the machine setup, a number of challenges were addressed among which two stands out: the cryostat design and Torque Transfer Element (TTE). The cryostat design showed that with a rather simple design and low cost technology and material (such as stainless steel), remarkable thermal and mechanical performances can be achieved. The compact design of the vacuum insulated cryostat with 10 mm net thickness resulted in ∼10 W of heat transfer at 77 K (for properly evacuated vacuum chamber). Even though, the 10 mm thick thermal insulation presents 12.5% of the air gap radius in this particular design, the implication of this achievement is encouraging for larger machines, particularly for the machines with a high pole number where the pole surface relative to the magnetic air gap is not large.

The heat transfer of only 10 W at 77 K is achieved due to an optimized design of the Torque Transfer Element which is integrated into the cryostat and is identified as an element with the largest contribution to the net heat load. Realizing the significance of the optimization of the thermal and mechanical properties, general recommendation towards a TTE geometry are presented and their validity verified in the design (the TTE with 10 W compared to the alternative - a shaft with an estimate of ∼60 W).

The HTS coil design confirmed the robustness of the both 1G and 2G HTS tape from AMSC (1) while problems with the 2G Superpower HTS tape was observed in both constructed coils, indicating the sensitivity of the HTS tape and the importance of the coil design. The difference between these, beside the fabrication method, was in the electric insulation used. The solution where an epoxy coating is applied to the HTS tape as an insulating layer consequently should increase the engineering current density of the coil (*Coil*#7 and *Coil*#8 have 2.5 times more turns compared to the others coils). However, both *Coil*#7 and *Coil*#8 were damaged most likely due to the thermal stress/strain which delaminated the HTS and thus degraded the I_c. Interestingly, the I_c value of the coils did not degrade with repeating cool-down which would be expected. Therefore, further investigations are required to understand and ensure that the coil design can mitigate damaging mechanical stresses.

To the author knowledge, the Superwind HTS machine, next to being the first HTS SM developed in Denmark, is the first HTS SM to operate with the combination of HTS conductors, both 1G and 2G type. This design approach, employing several types of the HTS conductors, was proposed as a method to increase the performance of the HTS field winding, but also to achieve a better value of the investment in HTS (since the 2G is twice the cost of 1G at the moment). Thus, the two arrangements of the HTS field winding with different placement of the 1G and 2G coils were tested. The 2G coil, *Coil*#6, with ∼15% of I_c reduction has a lower degree of sensitivity to the magnetic field and thereby to the placement in the HTS field winding, compared to the 1G coils (see Fig.5.13). In both arrangements, *Coil*#3 (the 1G coil) placed closest to the pole shoe was the coil with the lowest I_c, which limited the current of the field winding to ∼50 A. However, the significant improvement in the current capacity was observed in the case of *Coil*#5 (1G coil),when placed in Arr1 (close to the pole shoe), where the coil had $I_c \sim 50$ A but when placed in Arr2 (the middle of the coil stack) an $I_c \geq$80A (see Fig.5.14). Thus, almost 40% (50/80) of the turns of the coil could be omitted if the coil is strategically placed which presents substantial amount of HTS savings. As a general recommendation for combining 1G and 2G tapes in a machine, BSCCO coils should comprise only the inner coils in the field winding stack, whereas YBCO should be used as outer coils.

The second approach towards higher MMF of the HTS field winding, not used in machine design so far, is a multi power supply approach, where the number of current sources is increased so that a coil with large difference between operating and critical current could be utilized better. In the experimental setup each coil had its own power supply which made this configuration highly flexible. Several combinations of currents were supplied to the field winding (each coil separately) and a ∼12% increase in the MMF of the field winding was achieved. The same increase in the MMF was observed using only two power supplies implying that expected increase in the MMF will not scale linearly with the number of power supplies. Due to the fact that both the 1G and 2G HTS have significant sensitivity to magnetic field (including magnetic anisotropy), an HTS coil segments in different field orientation would have different current capabilities. Thus, it is expected that by employing multiple supplies even larger saving would be possible in a large machine. The HTS is (and will for a long time be) the largest contributor to the cost of a HTS machine whereby the reduction of the required amount would easily justify an additional power supply.

Finally, the HTS field winding showed substantial difference between d and q orientations of the armature reaction. While in the d axis, the armature had actually beneficial effect by slightly enhancing the current capacity of the field winding. In contrast, the armature reaction in the q axis the reduction of the critical current was the greatest. The difference between I_c of the field winding for no load and rated armature reaction in the q axis was found to be $\sim$20%. From the observed tendency of I_s, the control strategy of the excitation current was proposed with the aim to increase the performance of a HTS machine.

Depending on the degree of difference between the I_c at no load and at full load, substantial reduction of the armature loss can be achieved if the current of the field winding would adjust to the armature reaction in q axis. For 50% of partial load, a $\sim$20% lower loss could be achieved by introducing this control approach assuming the I_c will have the same reduction (20%) as in the case of the Superwind machine. A balance between the ac loss of the HTS generated by the variations of the field current and the armature losses saved by the proposed control will be a limiting factor to how fast load changes which could be followed.

6.2 Afterlife of the Superwind test machine

The work presented in this thesis is the initial step in a larger research effort targeted to develop HTS machines. The learning potential of the constructed experimental setup is very high. Hence, I would like to identify a few research directions and opportunities the setup can be used for.

6.2.1 Lowering the operating temperature

The operating temperature of a HTS device has a prevailing impact on its performance. We have so far only conducted experiments at 77 K. However it would be fairly easy, with modest additional funds, to incorporate a closed system conduction cooling where the cooling would be performed by a commercial cryocooler. This could be done by construction of an appropriate lid for the cryostat top. The expected net heat load of the machine (based on the thermal calculation performed in Ch.4) would not exceed 50 W even at 20 K, hence one cryocooler would suffice.

The motivation for lowering the temperature stems from the fact that the HTS tapes have an order of magnitude higher I_c at 20 K than at 77 K. Hence, with just four coils (from Arr1) cooled down at 20 K, the MMF coils would be able to generate would correspond to the $\geq$ 80k Amp –turns. Consecutively, resulting air gap flux would exceed ~1.5 T in the machine has cold steel or would be ~0.5 T in the case of air core machine. Other characteristics of the HTS are changing with temperature as well such as the degree of magnetic anisotropy (1G tape), thermal conductivity of materials impacting the thermal equilibrium of conductors when quench occurs, etc. Therefore, it is important to investigate these as well at the lower temperature.

6.2.2 HTS ac loss investigation

All experiments with revolving armature will generate an ac component of the flux in the machine, hence it is possible to measure and study ac losses in the machine. The HTS field winding had a number of hall probes integrated into the coils, which allow for flux perturbations to be correlated to the voltage and current of the coil.

Additionally, this study may identify the nature of the ac losses in the machine since this loss is not of the same nature as the one found in an ac application of HTS. In the general case, a dc current with a smaller ac component is flowing through the HTS, whereas the HTS tapes in the machine will be exposed to a dc flux on top of which an ac fluctuation is superposed. None of the analytical studies addressing the HTS ac losses have covered this particular case. Thereby, the only way to assess these would be measurements experiments or FE methods (which must be verified by the measurement). It is noteworthy to mention that an extensive work has been done by a colleague of mine, Victor M. Rodriguez Zermeno, on FE modeling based on the HTS physics (2G) that could be used to derive the ac losses of the HTS coils and machines.

6.2.3 HST tape types and different coil designs

We have tested three types of HTS tape. Two produced by AMSC performed as expected during the coil manufacturing and testing, whereas 2G tape produced by SuperPower, even though promising a doubling of the engineering current, proved to be challenging in practice (damaged by a thermal stress). Therefore, the importance of both coil design (insulation, winding procedure, condition monitoring, cooling, etc.) and HTS choice is emphasized throughout this thesis.

A number of HTS conductors are expected to become available in the future. The tapes from different manufacturers, employing different production techniques, may have different characteristics (mechanical, thermal, electrical, etc.). As the implications of these could challenge the coil fabrication, as we found to be the case with SuperPower 2G tape, it is crucial to examine and test various concepts and types of HTS tapes.

References

[1] American Superconductor Inc. Technical report, http://www.amsc.com/. xvii, 10, 13, 14, 15, 34, 73, 137

[2] SuperPower Inc. Technical report, http://www.superpower-inc.com/. xvii, 13, 15, 34, 73

[3] G. Klaus, M. Wilke, J. Frauenhofer, W. Nick, and H.-W. Neumuller. **Design Challenges and Benefits of HTS Synchronous Machines**. In *Proc. IEEE Power Engineering Society General Meeting*, pages 1–8, 2007. 1

[4] N. Mijatovic, A.B. Abrahamsen, C. Træholt, E. Seiler, M. Henriksen, V.M. Rodriguez-Zermeno, and N.F. Pedersen. **Superconducting generators for wind turbines: Design considerations**. In *Journal of Physics: Conference Series*, **234**, page 032038. IOP Publishing, 2010. 1, 37

[5] A.B. Abrahamsen, B.B. Jensen, E. Seiler, N. Mijatovic, V.M. Rodriguez-Zermeno, N.H. Andersen, and J. Østergård. **Feasibility study of 5 MW superconducting wind turbine generator**. *Physica C: Superconductivity*, 2011. 1, 71

[6] H.K. Onnes. **Investigations into the properties of substances at low temperatures, which have led, amongst other things, to the preparation of liquid helium**. *Nobel Lecture*, pages 333–335, 1913. 6, 7

[7] Department of Energy Basic Energy Sciences. http://science.energy.gov/. 6

[8] J.G. Bednorz and K.A. Müller. **Possible highT c superconductivity in the Ba- La-Cu- O system**. *Zeitschrift für Physik B Condensed Matter*, **64**(2):189–193, 1986. 6

[9] A. Khurana. **Bednorz and Müller Win Nobel Prize for New Superconducting Materials**. *Physics Today*, **40**:17, 1987. 6

[10] T.P. Sheahen. *Introduction to high-temperature superconductivity.* Plenum, New York, NY (United States), 1994. 6, 7, 8

[11] MK Wu, JR Ashburn, CJ Torng, P.H. Hor, RL Meng, L. Gao, Z.J. Huang, YQ Wang, and CW Chu. **Superconductivity at 93 K in a new mixed-phase Y-Ba-Cu-O compound system at ambient pressure**. *Physical Review Letters*, **58**(9):908–910, 1987. 6

[12] A. Mourachkine. *Room-temperature superconductivity.* Cambridge International Science Publishi, 2004. 6

[13] DG Hinks, H. Claus, and JD Jorgensen. **The complex nature of superconductivity in MgB2 as revealed by the reduced total isotope effect**. *Nature*, **411**(6836):457–460, 2001. 6

[14] GF Chen, Z. Li, D. Wu, G. Li, WZ Hu, J. Dong, P. Zheng, JL Luo, and NL Wang. **Superconductivity at 41 K and Its Competition with Spin-Density-Wave Instability in Layered CeO_ {1-x} F_ {x} FeAs**. *Physical review letters*, **100**(24):247002, 2008. 6

[15] D.G. Fink, H.W. Beaty, and H.W. Beaty. *Standard handbook for electrical engineers.* McGraw-Hill, 1993. 7

[16] D. Fishlock. *GUIDE TO SUPERCONDUCTIVITY.* 1970, 1969. 7

[17] RD Parks and M. Tinkham. *Superconductivity Vols. 1, 2*, **23**. 1970. 7

[18] H. Suhl, BT Matthias, and LR Walker. **Bardeen-Cooper-Schrieffer theory of superconductivity in the case of overlapping bands**. *Physical Review Letters*, **3**(12):552–554, 1959. 7

[19] J. Bardeen, L.N. Cooper, and J.R. Schrieffer. **Theory of superconductivity**. *Physical Review*, **108**(5):1175, 1957. 7

[20] J.R. Schrieffer and J.S. Brooks. *Handbook of high-temperature superconductivity: theory and experiment.* Springer Verlag, 2007. 8, 10

[21] MD Sumption, M. Bhatia, M. Rindfleisch, M. Tomsic, and EW Collings. **Transport properties of multifilamentary, in situ route, Cu-stabilized MgB2 strands: one metre segments and the Jc (B, T) dependence of short samples**. *Superconductor Science and Technology*, **19**:155, 2006. 9, 90

[22] B. Seeber. *Handbook of Applied Superconductivity: Applications*, **2**. Taylor & Francis, 1998. 10, 95

[23] A.V. Narlikar. *Frontiers in superconducting materials.* Springer Verlag, 2005. 10

[24] M. Kikuchi, T. Kato, K. Ohkura, N. Ayai, J. Fujikami, K. Fujino, S. Kobayashi, E. Ueno, K. Yamazaki, S. Yamade, et al. **Recent development of drastically innovative BSCCO wire** $(DI-BISCCO)$. *Physica C: Superconductivity*, **445**:717–721, 2006. 10

[25] Sumitomo Electric Industries. Technical report, http://global-sei.com. 10, 11

[26] Bruker Energy & Supercon Technologies. Technical report, http://www.bruker-est.com/. 10

[27] Zenergy Power. Technical report, http://www.zenergypower.com/. 10

[28] Asger Bech Abrahamsen. **Superconductor based energy production**. In *Materialer og energi*, pages 131–150, Lyngby, 2008. DMS. 12, 13, 14

[29] P. Paturi, T. Kulmala, J. Raittila, J.C. Grivel, R. Laiho, and NH Andersen. **Texture of YBCO/Ag PIT-tapes**. *Physica C: Superconductivity*, **408**:935–936, 2004. 12

[30] DA Korzekwa, JF Bingert, EJ Podtburg, and P. Miles. **Deformation processing of wires and tapes using the oxide powder in tube method**. *Applied superconductivity*, **2**(3-4):261–270, 1994. 12

[31] DK Finnemore, KE Gray, MP Maley, DO Welch, DK Christen, and DM Kroeger. **Coated conductor development: an assessment**. *Physica C: Superconductivity*, **320**(1-2):1–8, 1999. 12

[32] A. GOYAL, M. Parans Paranthaman, and U. Schoop. **The RABiTS approach: Using rolling-assisted biaxially textured substrates for high-performance YBCO superconductors**. *MRS bulletin*, **29**(8):552–561, 2004. 12

[33] MW Rupich, U. Schoop, DT Verebelyi, C. Thieme, W. Zhang, X. Li, T. Kodenkandath, N. Nguyen, E. Siegal, D. Buczek, et al. **YBCO coated conductors by an MOD / RABiTS process**. *Applied Superconductivity, IEEE Transactions on*, **13**(2):2458–2461, 2003. 12, 13

[34] P.J. Martin, H.A. MacLeod, R.P. Netterfield, CG Pacey, and W.G. Sainty. **Ion beam assisted deposition of thin films**. *Applied Optics*, **22**(1):178–184, 1983. 13

[35] Y. Jung, C.J. Sheehan, J.Y. Coulter, V. Matias, and D. Youm. **Pushing Coated Conductor Critical Currents Beyond 1 kA per cm Width: Stacks of YBCO Layers**. *Applied Superconductivity, IEEE Transactions on*, (99):1–1. 13

[36] SR Foltyn, QX Jia, PN Arendt, L. Kinder, Y. Fan, and JF Smith. **Relationship between film thickness and the critical current of YBaCuO-coated conductors**. *Applied Physics Letters*, **75**:3692, 1999. 13

[37] MP Siegal, PG Clem, JT Dawley, RJ Ong, MA Rodriguez, and DL Overmyer. **All solution chemistry approach for YBaCuO coated conductors**. *Applied physics letters*, **80**:2710, 2002. 13

[38] V. Boffa, G. Celentano, L. Ciontea, F. Fabbri, V. Galluzzi, U. Gambardella, G. Grimaldi, A. Mancini, and T. Petrisor. **Influence of film thickness on the critical current of $YBa2Cu3O7-x$ thick films on Ni-V biaxially textured substrates**. *Applied Superconductivity, IEEE Transactions on*, **11**(1):3158–3161, 2001. 13

[39] THEVA. http://www.theva.com/infobase/publikationen. 14, 16

[40] MW Rupich, U. Schoop, DT Verebelyi, CLH Thieme, D. Buczek, X. Li, W. Zhang, T. Kodenkandath, Y. Huang, E. Siegal, et al. **The development of second generation HTS wire at American Superconductor**. *Applied Superconductivity, IEEE Transactions on*, **17**(2):3379–3382, 2007. 14

[41] A.B. Abrahamsen, N. Mijatovic, E. Seiler, T. Zirngibl, C. Træholt, P.B. Nørgård, N.F. Pedersen, N.H. Andersen, and J. Østergaard. **Superconducting wind turbine generators**. *Superconductor Science and Technology*, **23**:034019, 2010. 14

[42] T. Kagiyama, K. Yamazaki, M. Kikuchi, S. Yamade, T. Nakashima, S. Kobayashi, K. Hayashi, K. Sato, J. Shimoyama, M. Inoue, et al. **Recent Progress in High Performance Ag-Sheathed Bi2223 Wire (DI-BSCCO)**. In *IOP Conference Series: Materials Science and Engineering*, **18**, page 152001. IOP Publishing, 2011. 14

[43] C. Lewis and J. Muller. **A direct drive wind turbine HTS generator**. In *Power Engineering Society General Meeting, 2007. IEEE*, pages 1–8. IEEE, 2007. 14

[44] V. Selvamanickam, Y. Chen, X. Xiong, Y.Y. Xie, M. Martchevski, A. Rar, Y. Qiao, R.M. Schmidt, A. Knoll, K.P. Lenseth, et al. **High performance 2G wires: From R&D to pilot-scale manufacturing**. *Applied Superconductivity, IEEE Transactions on*, **19**(3):3225–3230, 2009. 14, 15

[45] M.W. Rupich, X. Li, C. Thieme, S. Sathyamurthy, S. Fleshler, D. Tucker, E. Thompson, J. Schreiber, J. Lynch, D. Buczek, et al. **Advances in second generation high temperature superconducting wire manufacturing and R&D at American Superconductor Corporation**. *Superconductor Science and Technology*, **23**:014015, 2010. 14

[46] A. B. Abrahamsen, N. Mijatovic, E. Seiler, M. P. Sorensen, M. Koch, P. B. Norgard, N. F. Pedersen, C. Traeholt, N. H. Andersen, and J. Ostergard. **Design Study of 10 kW Superconducting Generator for Wind Turbine Applications**. *IEEE-J-ASC*, **19**(3):1678–1682, 2009. 15

[47] The Silver Institute. http://www.silverinstitute.org/2000pres.php. 15

[48] M. Humphries. *Rare Earth Elements: The Global Supply Chain.* DIANE Publishing, 2010. 15

[49] SR Foltyn, L. Civale, JL MacManus-Driscoll, QX Jia, B. Maiorov, H. Wang, and M. Maley. **Materials science challenges for high temperature superconducting wire**. *Nature materials*, **6**(9):631–642, 2007. 16

[50] P.N. Barnes, M.D. Sumption, and G.L. Rhoads. **Review of high power density superconducting generators: Present state and prospects for incorporating YBCO windings**. *Cryogenics*, **45**(10-11):670–686, 2005. 17, 28

[51] CJ Oberhauser and HR Kinner. **SOME CONSIDERATIONS IN THE DESIGN OF A SUPERCONDUCTING ALTERNATOR.** Technical report, Dynatech Corp., Cambridge, Mass., 1967. 17

[52] A. Hughes and TJE Miller. **Analysis of fields and inductances in air-cored and iron-cored synchronous machines**. *Proc. IEE*, **124**(2):121–126, 1977. 19, 37, 38, 39, 41

[53] TJE Miller and A. Hughes. **Comparative design and performance analysis of air-cored and iron-cored synchronous machines**. *Proc. IEE*, **124**(2):127–132, 1977. 19, 37, 39

[54] S.S. Kalsi. *Applications of High Temperature Superconductors to Electric Power Equipment*. Wiley-IEEE Press, 2011. 19, 23, 24, 25, 27

[55] J.M. Fogarty. **Development of a 100 MVA high temperature superconducting generator**. In *Power Engineering Society General Meeting, 2004. IEEE*, pages 2065–2067. IEEE, 2004. 21

[56] L. Li, T. Zhang, W. Wang, J. Alexander, X. Huang, K. Sivasubramaniam, ET Laskaris, JW Bray, and JM Fogarty. **Quench test of HTS coils for generator application at GE**. *Applied Superconductivity, IEEE Transactions on*, **17**(2):1575–1578, 2007. 21, 41

[57] JA Urbahn, RA Ackermann, X. Huang, ET Laskaris, K. Sivasubramaniam, and A. Steinbach. **The thermal performance of a 1.5 MVA HTS generator**. In *AIP Conference Proceedings*, **710**, page 849, 2004. 21

[58] S.S. Kalsi, K. Weeber, H. Takesue, C. Lewis, H.W. Neumueller, and R.D. Blaugher. **Development status of rotating machines employing superconducting field windings**. *Proceedings of the IEEE*, **92**(10):1688–704, 2004. 21, 23, 28

[59] P. Tixador. **Development of superconducting power devices in Europe**. *Physica C: Superconductivity*, **470**(20):971–979, 2010. 21

[60] L. SANFORD. **German hydro plant is the first to install an HTS generator**. *Modern power systems*, (GERMANY):22–23, 2007. 21

[61] R. Fair, C. Lewis, J. Eugene, and M. Ingles. **Development of an HTS hydroelectric power generator for the hirschaid power station**. In *Journal of Physics: Conference Series*, **234**, page 032008. IOP Publishing, 2010. 21

[62] B. Grzesik, M. Stepien, K. Bodzek, R. Fair, and M. Ingles. **Tests of a vacuum gauge for an HTS hydrogenerator**. In *Power Electronics and Motion Control Conference (EPE/PEMC), 2010 14th International*, pages T15–13. IEEE. 21

[63] B.B. Gamble, S. Kalsi, G. Snitchler, D. Madura, and R. Howard. **The status of HTS motors**. In *Power Engineering Society Summer Meeting, 2002 IEEE*, **1**, pages 270–274. IEEE. 23, 24, 28

[64] M. Frank, J. Frauenhofer, P. Van Hasselt, W. Nick, H.W. Neumueller, and G. Nerowski. **Long-term operational experience with first siemens 400 kW HTS machine in diverse configurations**. *Applied Superconductivity, IEEE Transactions on*, **13**(2):2120–2123, 2003. 23, 41

[65] J. Frauenhofer, J. Grundmann, G. Klaus, and W. Nick. **Basic concepts, status, opportunities, and challenges of electrical machines utilizing high-temperature superconducting (HTS) windings**. In *Journal of Physics: Conference Series*, **97**, page 012189. IOP Publishing, 2008. 23, 24, 28, 29

[66] JP Voccio, BB Gamble, CB Prum, and HJ Picard. **125 HP HTS motor field winding development**. *Applied Superconductivity, IEEE Transactions on*, **7**(2):519–522, 1997. 23

[67] D. Aized, BB Gamble, A. Sidi-Yekhlef, JP Voccio, DI Driscoll, BA Shoykhet, and BX Zhang. **Status of the 1000 HP HTS motor development**. *Applied Superconductivity, IEEE Transactions on*, **9**(2):1197–1200, 1999. 23

[68] G. Papst, BB Gamble, AJ Rodenbush, and R. Schöttler. **Development of synchronous motors and generators with HTS field windings**. *Superconductor Science and Technology*, **10**:924, 1997. 23

[69] HW Neumüller, W. Nick, B. Wacker, M. Frank, G. Nerowski, J. Frauenhofer, W. Rzadki, and R. Hartig. **Advances in and prospects for development of high-temperature superconductor rotating machines at Siemens**. *Superconductor Science and Technology*, **19**:S114, 2006. 23

[70] W. Nick, M. Frank, G. Klaus, J. Frauenhofer, and H.W. Neumuller. **Operational Experience With the World's First 3600 rpm 4 MVA Generator at Siemens**. *Applied Superconductivity, IEEE Transactions on*, **17**(2):2030–2033, 2007. 24, 40, 41

[71] M. Wilke, K. Schleicher, G. Klaus, W. Nick, H.W. Neumuller, J. Frauenhofer, K. Kahlen, and R. Hartig. **Numerical calculations for high-temperature superconducting electrical machines**. In *Electrical Machines, 2008. ICEM 2008. 18th International Conference on*, pages 1–6. IEEE. 24

[72] A.P. Malozemoff. **The new generation of superconductor equipment for the electric power grid**. *Applied Superconductivity, IEEE Transactions on*, **16**(1):54–58, 2006. 24

[73] S.S. Kalsi, D. Madura, and M. Ingram. **Superconductor synchronous condenser for reactive power support in an electric grid**. *Applied Superconductivity, IEEE Transactions on*, **15**(2):2146–2149, 2005. 24

[74] SS Kalsi, BB Gamble, G. Snitchler, and SO Ige. **The status of HTS ship propulsion motor developments**. In *Power Engineering Society General Meeting, 2006. IEEE*, pages 5–pp. IEEE, 2006. 24, 40

[75] J. Buck, B. Hartman, R. Ricket, B. Gamble, T. MacDonald, and G. Snitchler. **Factory testing of a 36.5 MW high temperature superconducting propulsion motor**. *Fuel Tank to Target: Building the Electric Fighting Ship at American Society of Naval Engineers Day 2007*. 24, 40

[76] H. Wen, W. Bailey, M.K. Al-Mosawi, K. Goddard, C. Beduz, and Y. Yang. **Further Testing of an Iron-Cored HTS Synchronous Generator Cooled by Liquid Air**. *Applied Superconductivity, IEEE Transactions on*, (99):1–1. 24

[77] H. Wen, W. Bailey, K. Goddard, M. Al-Mosawi, C. Beduz, and Y. Yang. **Performance test of a 100 kW HTS generator operating at 67 K–77 K**. *Applied Superconductivity, IEEE Transactions on*, **19**(3):1652–1655, 2009. 24, 40, 41

[78] K.F. Goddard, B. Lukasik, and J.K. Sykulski. **Alternative designs of a superconducting synchronous generator: the Southampton approach**. In *Electrical Machines, 2008. ICEM 2008. 18th International Conference on*, pages 1–6. IEEE. 24

[79] MK Al-Mosawi, W. Bailey, C. Beduz, K. Goddard, and Y. Yang. **Development of a coreless HTS synchronous generator operating at sub-cooled liquid nitrogen temperatures**. In *Journal of Physics: Conference Series*, **97**, page 012205. IOP Publishing, 2008. 25

[80] MK Al-Mosawi, K. Goddard, C. Beduz, and Y. Yang. **Coreless HTS synchronous generator operating at liquid nitrogen temperatures**. *Applied Superconductivity, IEEE Transactions on*, **17**(2):1599–1602, 2007. 25

[81] YK Kwon, SK Baik, EY Lee, JD Lee, YC Kim, TS Moon, HJ Park, WS Kwon, SH Lee, JP Hong, et al. **Status of HTS Motor Development in Korea**. In *Power Engineering Society General Meeting, 2007. IEEE*, pages 1–5. IEEE. 25

[82] YK Kwon, HM Kim, SK Baik, EY Lee, JD Lee, YC Kim, SH Lee, JP Hong, YS Jo, and KS Ryu. **Performance test of a 1 MW class HTS synchronous motor for industrial application**. *Physica C: Superconductivity*, **468**(15-20):2081–2086, 2008. 25, 28

[83] YK Kwon, SK Baik, EY Lee, JD Lee, JM Kim, YC Kim, TS Moon, HJ Park, WS Kwon, JP Hong, et al. **Status of HTS motor development for industrial applications at KERI & DOOSAN**. *Applied Superconductivity, IEEE Transactions on*, **17**(2):1587–1590, 2007. 25

[84] C. Lewis. **Direct drive superconducting wind generators**. *Wind Power Generation and Wind Turbine Design*, page 303, 2010. 25

[85] AMSC. http://www.amsc.com/documents/displaypdf.php?id=7516. 25

[86] P. Tixador, Y. Brunet, P. Vedrine, Y. Laumond, and JL Sabrie. **Electrical tests on a fully superconducting synchronous machine**. *Magnetics, IEEE Transactions on*, **27**(2):2256–2259, 1991. 25

[87] I. Muta, H. Tsukiji, T. Hoshino, and E. Mukai. **Electrical characteristics of fully superconducting synchronous generator in persistent excitation mode**. *Magnetics, IEEE Transactions on*, **28**(1):434–437, 1992. 25

[88] Y. Jiang, R. Pei, Q. Jiang, Z. Hong, and TA Coombs. **Control of a superconducting synchronous motor**. *Superconductor Science and Technology*, **20**:392, 2007. 25

[89] P. Tixador and H. Daffix. **Conceptual design of an electrical machine with both low and high T c superconductors**. *Applied Superconductivity, IEEE Transactions on*, **7**(4):3858–3865, 1997. 25

[90] MP Oomen, R. Nanke, and M. Leghissa. **Modelling and measurement of ac loss in BSCCO/Ag-tape windings**. *Superconductor Science and Technology*, **16**:339, 2003. 25

[91] S. Fukui, T. Noguchi, J. Ogawa, M. Yamaguchi, T. Sato, O. Tsukamoto, and T. Takao. **Numerical study on AC loss minimization of multi-layer tri-axial HTS cable for 3-phase AC power transmission**. *Applied Superconductivity, IEEE Transactions on*, **17**(2):1700–1703, 2007. 25

[92] Advance Magnetic Lab. http://www.magnetlab.com/energy/electrical-machinery/. 25

[93] J. Sim, K. Lee, G. Cha, and J.K. Lee. **Development of a HTS squirrel cage induction motor with HTS rotor bars**. *Applied Superconductivity, IEEE Transactions on*, **14**(2):916–919, 2004. 26

[94] CL Goodzeit, RB Meinke, and MJ Ball. **A superconducting induction motor using double-helix dipole coils**. *Applied Superconductivity, IEEE Transactions on*, **13**(2):2235–2238, 2003. 26

[95] G. Morita, T. Nakamura, and I. Muta. **Theoretical analysis of a YBCO squirrel-cage type induction motor based on an equivalent circuit**. *Superconductor Science and Technology*, **19**:473, 2006. 26

[96] T. Konishi, T. Nakamura, T. Nishimura, and N. Amemiya. **Analytic Evaluation of HTS Induction Motor for Electric Rolling Stock**. *Applied Superconductivity, IEEE Transactions on*, (99):1–1. 26

[97] J. Sim, M. Park, H. Lim, G. Cha, J. Ji, and J. Lee. **Test of an induction motor with HTS wire at end ring and bars**. *Applied Superconductivity, IEEE Transactions on*, **13**(2):2231–2234, 2003. 26

[98] B. Oswald, KJ Best, M. Setzer, M. Söll, W. Gawalek, A. Gutt, L. Kovalev, G. Krabbes, L. Fisher, and HC Freyhardt. **Reluctance motors with bulk HTS material**. *Superconductor Science and Technology*, **18**:S24, 2005. 26

[99] B. Oswald, K.J. Best, M. Setzer, M. Söll, W. Gawalek, A. Gutt, L. Kovalev, L. Fisher, G. Krabbes, and HC Freyhardt. **Optimization of Our SC HTS Reluctance Motor**. In *AIP Conference Proceedings*, **711**, page 879, 2004. 26

[100] P. Campbell. **Principles of a permanent-magnet axial-field DC machine**. *Proc. IEE*, **121**(12):1489–1494, 1974. 27

[101] B.W. Strohm. **Voltage homopolar machine**, September 19 1995. US Patent 5,451,825. 27

[102] AD Appleton. **Superconducting dc machines**. *Superconducting Machines and Devices: Large Systems Applications*, **1**:219–277, 1974. 27

[103] T. Curcic and S.A. Wolf. **Superconducting hybrid power electronics for military systems**. *Applied Superconductivity, IEEE Transactions on*, **15**(2):2364–2369, 2005. 27

[104] J.G. Weisend et al. *Handbook of cryogenic engineering*. Taylor & Francis Philadelphia, PA, 1998. 28

[105] M.K. Al-Mosawi, C. Beduz, and Y. Yang. **Construction of a 100 kVA high temperature superconducting synchronous generator**. *Applied Superconductivity, IEEE Transactions on*, **15**(2):2182–2185, 2005. 28, 30, 67

[106] S.W. Van Sciver. **Cryogenic systems for superconducting devices**. *Physica C: Superconductivity*, **354**(1-4):129–135, 2001. 28

[107] T.M. Flynn and Inc NetLibrary. *Cryogenic engineering*. Marcel Dekker New York, 1997. 28, 55, 57, 65, 67, 68

[108] R.A. Ackermann, K.G. Herd, and W.E. Chen. **Advanced Cryocooler Cooling for MRI Systems**. *Cryocoolers 10*, pages 857–867, 2002. 28

[109] CryoMech. http://www.cryomech.com/AL325.php. 29

[110] CryoMech. http://www.cryomech.com/PT63.php. 29

[111] R. Radebaugh. **Development of the pulse tube refrigerator as an efficient and reliable cryocooler**. *Proc. Institute of Refrigeration (London)*, **2000**, 1999. 29

[112] J. Ko, S. Jeong, H. Kim, J. Jung, J. Choi, S. In, M. Sohn, and Y.K. Kwon. **Rotating Cryocooler for Superconducting Motor**. In *AIP Conference Proceedings*, **823**, page 653, 2006. 29

[113] JM Poncet, A. Ravex, and I. Charles. **Developments on single and double stage GM type pulse tube cryorefrigerators**. *Cryocoolers 11*, pages 229–233, 2002. 29

[114] J.L. Kirtley Jr, J.L. Smith Jr, and S.D. Umans. **Cryogenic isolating torque tubes for a superconducting generator-detailed model and performance analysis**. *Energy Conversion, IEEE Transactions on*, **6**(2):267–273, 1991. 30

[115] TE Laskaris and KF Schoch. **Superconducting rotor development for a 20 MVA generator**. *Power Apparatus and Systems, IEEE Transactions on*, (6):2031–2039, 1980. 30

[116] A. Ueda. **Rotor for a superconducting rotating electric machine**, April 14 1987. US Patent 4,658,170. 30

[117] K.J. Baumann. **Flexible coupling for rotor elements of a superconducting generator**, September 26 1978. US Patent 4,117,357. 30

[118] W.O.S. Bailey, M. Al-Mosawi, Y. Yang, K. Goddard, and C. Beduz. **The design of a lightweight HTS synchronous generator cooled by subcooled liquid nitrogen**. *Applied Superconductivity, IEEE Transactions on*, **19**(3):1674–1677, 2009. 30, 67

[119] P. Kummeth, M. Frank, W. Nick, G. Nerowski, and H.W. Neumueller. **Development of synchronous machines with HTS rotor**. *Physica C: Superconductivity*, **426**:1358–1364, 2005. 31, 40

[120] B.B. Gamble and G.L. Snitchler. **Superconducting synchronous motor construction**, July 7 1998. US Patent 5,777,420. 31

[121] B.A. Shoykhet. **Composite torque tube for superconducting motor**, October 10 2000. US Patent 6,129,477. 31

[122] J. Dewolf. *Mechanics Of Materials (In Si Units)*. McGraw-Hill Education (India) Pvt Ltd, 2004. 32

[123] M.Yazdanian, P.Erhaminia, M.RZolghadri, and M.Fardmanesh. **Investigation of iron-cored Structure in HTS Synchronous Machine for Industrial Application**, 2011. Presented at conference. 38

[124] P. Kundur, N.J. Balu, and M.G. Lauby. *Power system stability and control*, **141**. McGraw-Hill New York, 1994. 39, 134

[125] M. Beckenbach, F. Hornung, M. Klaser, P. Leys, B. Lott, and T. Schneider. **Manufacture and test of a 5 T Bi-2223 insert coil**. *Applied Superconductivity, IEEE Transactions on*, **15**(2):1484–1487, 2005. 43

[126] J.R. Miller. **The NHMFL 45-T hybrid magnet system: Past, present, and future**. *Applied Superconductivity, IEEE Transactions on*, **13**(2):1385–1390, 2003. 43, 44

[127] D.W. Hazelton, V. Selvamanickam, J.M. Duval, D.C. Larbalestier, W.D. Markiewicz, H.W. Weijers, and R.L. Holtz. **Recent developments in 2G HTS coil technology**. *Applied Superconductivity, IEEE Transactions on*, **19**(3):2218–2222, 2009. 44

[128] A. Ghattas, M. Annabi, M. Zouaoui, F.B. Azzouz, and M.B. Salem. **Flux pinning by Al-based nano particles embedded in polycrystalline (Bi, Pb)-2223 superconductors**. *Physica C: Superconductivity*, **468**(1):31–38, 2008. 44

[129] A. Korpela, J. Lehtonen, R. Mikkonen, and R. Perälä. **Temperature dependent current-voltage characteristics of an HTS coil having a poor resistive joint**. *Physica C: Superconductivity*, **386**:457–461, 2003. 44

[130] M. Kang, K. Lee, G. Cha, and H. Lee. **Design Method of a High Field HTS Magnet Consisting of Pancake Windings Having Different Current in Each Pancake Winding**. *Applied Superconductivity, IEEE Transactions on*, **18**(2):1537–1540, 2008. 44

[131] K. Lee, M. Kang, G. Cha, H. Lim, and T. Ahn. **Properties of an HTS magnet with pancake windings excited by multiple power sources**. *Applied Superconductivity, IEEE Transactions on*, **18**(2):1533–1536, 2008. 45

[132] V. Cavaliere, M. Cioffi, A. Formisanao, and R. Martone. **Shape optimization of high Tc superconducting magnets**. *Magnetics, IEEE Transactions on*, **38**(2):1129–1132, 2002. 46

[133] N. Mijatovic, B. B. Jensen, A. B. Abrahamsen, V. M. R. Zermeno, C. Traeholt, and N. F. Pedersen. **Coil Optimization for High Temperature Superconductor Machines**. *IEEE-J-ASC*, **21**(3):1136–1140, 2011. 46, 47, 123

[134] Comsol. **http://www.comsol.com/products/multiphysics/**, 2011. 46

[135] 24-Bit Universal AI NI 9239. http://sine.ni.com/nips/cds/view/p/lang/en/nid/208797. 51

[136] 24-Bit Universal AI NI 9219. http://sine.ni.com/nips/cds/view/p/lang/en/nid/208789. 51

[137] Koyo Bearing. http://www.danskkuglelejecenter.dk/koyolejer3.html. 52

[138] Danffoss Serial No.131b1673. http://www.danfoss.com/Denmark. 52

[139] P. Beckley. *Electrical steels for rotating machines*. Number 37. Inst of Engineering & Technology, 2002. 52

[140] Rogowski current transducer CWT015. http://www.powertekuk.com/cwtmini.htm. 53

[141] Juha Pyrhnen, Tapani Jokinen, and Valria Hrabovcov. *Design of rotating electrical machines*, pages i–xxv. John Wiley & Sons, Ltd, 2008. 53

[142] F.P. Incropera and D.P. De Witt. *Fundamentals of heat and mass transfer*. John Wiley and Sons Inc., New York, NY, 1985. 55

[143] F. Incropera and D. DeWitt. *Introduction to heat transfer*. John Wiley and Sons Inc., New York, NY, 1985. 55

[144] JE Fesmire. **Aerogel insulation systems for space launch applications**. *Cryogenics*, **46**(2-3):111–117, 2006. 55, 62

[145] D. Hull and TW Clyne. *An introduction to composite materials*. Cambridge Univ Pr, 1996. 57

[146] Aage Lystrup. **Typical properties of fibre composites:For preliminary design of fibre composite components for super conductor wind turbine generator**. Technical report, Ris National Laboratory for Sustainable Energy, Technical University of Denmark, Roskilde, Denmark,December 2008, Ris-I-2789(EN), 2008. 57

[147] DK Hale. **The physical properties of composite materials**. *Journal of Materials Science*, **11**(11):2105–2141, 1976. 57

[148] R.L. Tobler and D.T. Read. **Fatigue resistance of a uniaxial S-glass/epoxy composite at room and liquid helium temperatures**. *Journal of Composite Materials*, **10**(1):32, 1976. 57

[149] M. Surendra Kumar, N. Chawla, A. Priyadarsini, I. Mishra, and BC Ray. **Assessment of microstructural integrity of glass/epoxy composites at liquid nitrogen temperature**. *Journal of reinforced plastics and composites*, **26**(11):1083, 2007. 57

[150] W. Meeks and Y. Zlobinsky. **Vacuum drying system with cryopumping of solvent recovery feature**, November 23 1993. US Patent 5,263,268. 62

[151] HK Yeom, YJ Hong, SJ Park, TB Seo, KC Seong, and HJ Kim. **Study of cryogenic conduction cooling systems for an HTS SMES**. *Applied Superconductivity, IEEE Transactions on*, **17**(2):1955–1958, 2007. 62

[152] K.D. Timmerhaus. *Advances in cryogenic engineering*, **39**. Plenum Publishing Corporation, 1994. 62, 68

[153] **http://www.ruag.com/en/Space/Products/**. 68

[154] HBM UB9 500N. http://www.hbm.com/en/geoipcn=2. 80

[155] HOA 0901 012. http://sensing.honeywell.com/index.cfm/ciid/154366/laid/1.htm. 82

[156] C.P. Poole. *Handbook of superconductivity*. Academic Press, 2000. 90

[157] Y. Iwasa. *Case studies in superconducting magnets: design and operational issues*. Springer Verlag, 2009. 90

[158] L. Dresner. **Quench energies of potted magnets**. *Magnetics, IEEE Transactions on*, **21**(2):392–395, 1985. 90

[159] F. Trillaud, M.C. Ahn, J. Bascunan, W.S. Kim, J.P. Voccio, and Y. Iwasa. **Quench behavior, quench protection of a YBCO test coil assembly**. *Applied Superconductivity, IEEE Transactions on*, **18**(2):1329–1332, 2008. 90, 94

[160] SX Dou, HK Liu, MH Apperley, KH Song, and CC Sorrell. **Critical current density in superconducting Bi-Pb-Sr-Ca-Cu-O wires and coils**. *Superconductor Science and Technology*, **3**:138, 1990. 90

[161] T.P. Sheahen. **Introduction to high-temperature superconductivity**. *????????*, 1994. 95

[162] V. M. Rodriguez-Zermeno, N. Mijatovic, C. Traeholt, T. Zirngibl, E. Seiler, A. B. Abrahamsen, N. F. Pedersen, and M. P. Sorensen. **Towards Faster FEM Simulation of Thin Film Superconductors: A Multiscale Approach**. *IEEE-J-ASC*, **21**(3):3273–3276, 2011. 96